FEDERAL UNIVERSITY OF SÃO CARLOS
CENTER OF EXACT SCIENCE AND TECHNOLOGY
GRADUATE PROGRAM IN MATERIALS SCIENCE AND ENGINEERING

INFLUENCE OF BOBBIN TOOL FRICTION STIR WELDING (BT-FSW) VARIANTS ON THE MICROSTRUCTURE AND PROPERTIES OF AA2060 AND AA2196 ALUMINUM ALLOYS

Joana Amaral de Carvalho

São Carlos - SP
2020

FEDERAL UNIVERSITY OF SÃO CARLOS
CENTER OF EXACT SCIENCE AND TECHNOLOGY
GRADUATE PROGRAM IN MATERIALS SCIENCE AND ENGINEERING

INFLUENCE OF BOBBIN TOOL FRICTION STIR WELDING (BT-FSW) VARIANTS ON THE MICROSTRUCTURE AND PROPERTIES OF AA2060 AND AA2196 ALUMINUM ALLOYS

Joana Amaral de Carvalho

Dissertation presented to Graduate Program in Materials Science and Engineering (PPG-CEM) in fulfillment of the requirements to obtain the MASTER OF SCIENCE DEGREE IN MATERIALS SCIENCE AND ENGINEERING.

Supervisor: Prof. Dr. Nelson Guedes de Alcântara

Co-supervisor: Prof. Dr. Guilherme Zepon

São Carlos - SP
2020

DEDICATION

To God for giving me health and strength to overcome obstacles.

To my parents, Simone and João Bosco, and my siblings, Marcia, Lilian and Júnior, for their love, encouragement and unconditional support.

To all who were directly or indirectly part of my background, thank you very much.

Finally, a special thanks to my best friend Milli Aline Sant'Anna for being present at all times of my graduation. I love you.

CANDIDATE VITAE

Materials engineering degree at Federal University of São Carlos (2017).

Folha de Aprovação

Defesa de Dissertação de Mestrado da candidata Joana Amaral de Carvalho, realizada 18/06/2020.

Comissão Julgadora:

Prof. Dr. Nelson Guedes de Alcântara (UFSCar)

Prof. Dr. Claudemiro Bolfarini (UFSCar)

Prof. Dr. Jorge Fernandez dos Santos (WMP/HZG)

O presente trabalho foi realizado com apoio da Coordenação de Aperfeiçoamento de Pessoal de Nível Superior - Brasil (CAPES) - Código de Financiamento 001.

O Relatório de Defesa assinado pelos membros da Comissão Julgadora encontra-se arquivado junto ao Programa de Pós-Graduação em Ciência e Engenharia de Materiais.

ACKNOWLEDGMENTS

This work is the result of one year of research on Bobbin Tool Friction Stir Welding at Helmholtz-Zentrum Geesthacht (former GKSS) and at Department of Materials Engineering (DEMa) in association with Center for Characterization and Development of Materials (CCDM/DEMa/UFSCar). The results presented here could not have been achieved without the help and support of many dear colleagues and friends. I would like to thank:

- My best friend, Milli Aline Sant'Anna for the hours of fun, dedication, correction of texts, help writing this thesis, help in scientific questions and for all support when I was about to fail;
- My sister Professor Doctor Lilian Amaral de Carvalho, for reading and improving this dissertation;
- Qaiser Ali Khan and Usama Ahmed, for all the friendship, talks about life, religion, culture and amazing food that inspired me during my abroad time;
- Dagmar Koschek for taking care of us as her own children, for the wine nights and for all the kindness;
- Dr. Jannik Goebel for the supervision of the work and for the donation of drawings elaborated by him to illustrate the tool in this work;
- Dr. Jorge F. dos Santos for his help in scientific and all other questions;
- Professor Dr. Guilherme Zepon and Dr. Nelson Guedes for improving this dissertation;
- This study was financed in part by the Coordenação de Aperfeiçoamento de Pessoal de Nível Superior - Brasil (CAPES) - Finance Code 001.

ABSTRACT

In order to reduce total costs in aircrafts production, operation and maintenance, materials and processing techniques have been continuously further optimized. In this scenario, aluminum-lithium alloys have been studied due to its mechanical properties, low density and higher fatigue crack growth resistance compared to others aluminum alloys and steels. However, joining technologies usually applied in these alloys present limitations regarding uniformity, energy input and production costs. Since welding processes may not require any material additions such as rivets used in the mechanical fastening techniques conventionally used in joining aircrafts parts, it can contribute in saving structural weight. The aim of this research is to compare and understand the effect of two different methods of bobbin tool friction stir welding (BT-FSW), Self-Reacting BT-FSW (SRBT-FSW) and Stationary (upper) Shoulder BT-FSW (SSuBT-FSW) on the microstructure and mechanical properties of 3 mm thick aluminum-lithium alloys (AA2060 and AA2196) plates in butt joint. In addition, the study of the influence of energy input on bobbin tool friction stir welding (BT-FSW) was evaluated to understand the effect of the parameters on the alloys. Defect free welds have been produced featuring a high-quality surface finish on the stationary side. In general, the self-reacting variant enabled welding with faster welding speeds than the SSuBT-FSW technique, which was the reason for lower energy input on SRBT-FSW. The influence of the processes on the microstructure and mechanical properties of different regions of the produced joint was evaluated by means of optical microscopy (OM), hardness testing and tensile testing. Differential scanning calorimetry (DSC) was performed to evaluate the influence of variants on precipitate evolution. Superior results were achieved welding AA2060 and AA2196 using SRBT-FSW- low energy input, reaching up to 78% of ultimate tensile strength of base metal.

Key-words- Aluminum-lithium alloys; Bobbin Tool Friction Stir Welding (BT-FSW); AA2060; AA2196; Microstructure; Mechanical properties; Energy input; Friction Stir Welding (FSW); Solid state welding.

RESUMO

Influência de duas variantes da soldagem por fricção e mistura usando-se a ferramenta *bobbin tool* na evolução das propriedades mecânicas e metalúrgicas das ligas AA2060 e AA2196

A fim de reduzir os custos totais na produção, operação e manutenção de aeronaves, os materiais e as técnicas de processamento foram continuamente otimizadas. Neste cenário, ligas de Al-Li são estudadas devido às suas propriedades mecânicas quando comparada a outras ligas de alumínio e aço. Entretanto, as técnicas de união usualmente aplicadas a estas ligas apresentação limitações quanto à uniformidade da junção, eficiência energética e custos. Como os processos de soldagem podem não exigir adições de material, como rebites usados nas técnicas de fixação mecânica, isso pode contribuir para a economia de peso estrutural. O objetivo desta pesquisa é comparar e entender o efeito de dois métodos diferentes do BT-FSW, o BT-FSW de auto-reação (SRBT-FSW) e o BT-FSW de ombro (superior) estacionário (SSuBT-FSW), no processo metalúrgico e evolução das propriedades mecânicas de chapas de liga de Al-Li, em junta de topo. Além disso, foi avaliado o estudo da influência do aporte de energia na soldagem por fricção. Soldas sem defeitos foram produzidas com um acabamento superficial de alta qualidade no lado estacionário. Em geral, SRBT-FSW permitiu a soldagem com velocidades de soldagem mais rápidas que a técnica SSuBT-FSW, o que permitiu soldas com menor aporte de energia na variante SRBT-FSW. A influência dos processos nas propriedades mecânicas e metalúrgicas de diferentes regiões da junta produzida foi avaliada por microscopia óptica (OM), teste de dureza e teste de tração. Calorimetria exploratória diferencial (DSC) foi realizada para avaliar a influência de variantes na evolução dos precipitados. Os melhores resultados foram obtidos na soldagem de AA2060 e AA2196 usando SRBT- baixa energia, atingindo 78% da resistência a tração do material de base.

Palavras-chave- Ligas de alumínio-lítio; Bobbin Tool Friction Stir Welding (BT-FSW); AA2060; AA2196; Microestrutura; Propriedades mecânicas; entrada de energia; Soldagem por Fricção e Mistura (FSW); Soldagem no estado sólido.

TABLE OF CONTENTS

Page

LIST OF TABLES

Page

LIST OF FIGURES

Page

SYMBOLS AND ABBREVIATIONS

AA	Aluminum Alloy
AS	Advancing Side
AW	As Welded
AWS	American Welding Society
BM	Base Material
BoP	Bead-on-Plate
BT-FSW	Bobbin Tool Friction Stir Welding
CCDM	Center for Characterization and Development of Materials
d	Average diameter of the grains
DEMa	Department of Materials Engineering of Federal University of São Carlos
DoE	Design of Experiments
DRX	Dynamic Recrystallization
DSC	Differential Scanning Calorimetry
Es	Energy input per length
FSW	Friction Stir Welding
GBP	Grain Boundary Particles
GP	Guinier-Preston zones
HAZ	Heat Affected Zone
HEW	High Energy input Weldment
HV	Vickers Hardness – [HV]
HZG	Helmholtz-Zentrum Geesthacht
JLR	Joint Line Remnant
k	Material constant
LEW	Low Energy input Weldment
M	Torque – [N·m]
OM	Optical Microscopy
PFZ	Precipitate Free Zone
RS	Retreating Side
RT	Room Temperature

s	Second – [s]
S	Al_2CuMg precipitate
SLC	Severe Localized Corrosion
SRBT-FSW	Self-Reacting Bobbin Tool Friction Stir Welding
SS	Stainless Steel
SSuBT-FSW	Stationary (upper) Shoulder Bobbin Tool Friction Stir Welding
SSS	Super-Saturate Solution
SZ	Stir Zone
Tb	$Al_{7.5}LiCu_4$ precipitate
TMAZ	Thermo-Mechanically Affected Zone
TWI	The Welding Institute
T_1	Al_2CuLi precipitate
T_2	Al_6Li_3Cu precipitate
V	Volt
WC	Weld Center/SZ Center
vol.%	Volume Percentage
wt. %	Weight Percentage
δ'	Al_3Li precipitate
θ	Incoherent precipitate
θ'	Al_2Cu precipitate (semi-coherent precipitate)
θ''	Coherent precipitate
v	Traverse (welding) speed – [$mm \cdot min^{-1}$]
σ_y	Yield Strength- [MPa]
σ_0	Friction Stress – [MPa]
ω	Rotation rate – [RPM]

1 INTRODUCTION

Adding alloying elements and thermal treatment have been an important strategy when using metals, as aluminum and iron, as structural components. The reason is that these methodologies can significantly modify the properties of the metals, e.g. altering its density, strength, toughness and corrosion resistance leading to the improvement of the performance that is essential for the technological development of humanity [1].

The addition of 1% weight of lithium in aluminum generates approximately 3% decrease in density and 6% increase in Young`s elastic modulus. Besides, it enables the formation of strong hardening precipitates that promote higher fatigue crack growth resistance, what makes this alloy an interesting material for aerospace and aeronautical industries. The opportunity to make these improvements in the metal property led to the study of aluminum-lithium alloys since middle 1920's [2]. However, the presence of Li can also decrease the ductility and fracture toughness besides providing significant anisotropy in mechanical properties. The third generation of Al-Li alloys could achieve balanced properties and showed great advantage when used in modern air and spacecraft vehicles. Therefore, these alloys have been investigated over the last decades regarding their mechanical properties correlated with microstructure evolution [3,4].

In order to reduce total costs in aircrafts production, operation and maintenance, materials and processing techniques have been continuously further optimized. Low-density metals like aluminum and its alloys have been applied predominantly to aircrafts and aerospace structures during the past century. A major benefit of reducing the structural weight of the transportation components is to improve fuel efficiency. Moreover, increasing corrosion and fatigue properties can generate cost savings regarding maintenance in service [5].

According to a leading aircraft manufacturer [6], more than 30% of airlines operating costs refer to fuel expenses. Modern aircrafts like Airbus' A350 XWB have achieved a 25% reduction of fuel consumption by improving materials

selection, aerodynamics and propulsion technology. The aircraft is composed by 19 wt.% aluminum alloys including aluminum-lithium alloys applied in floor beams, frames, ribs and landing gear bays [7].

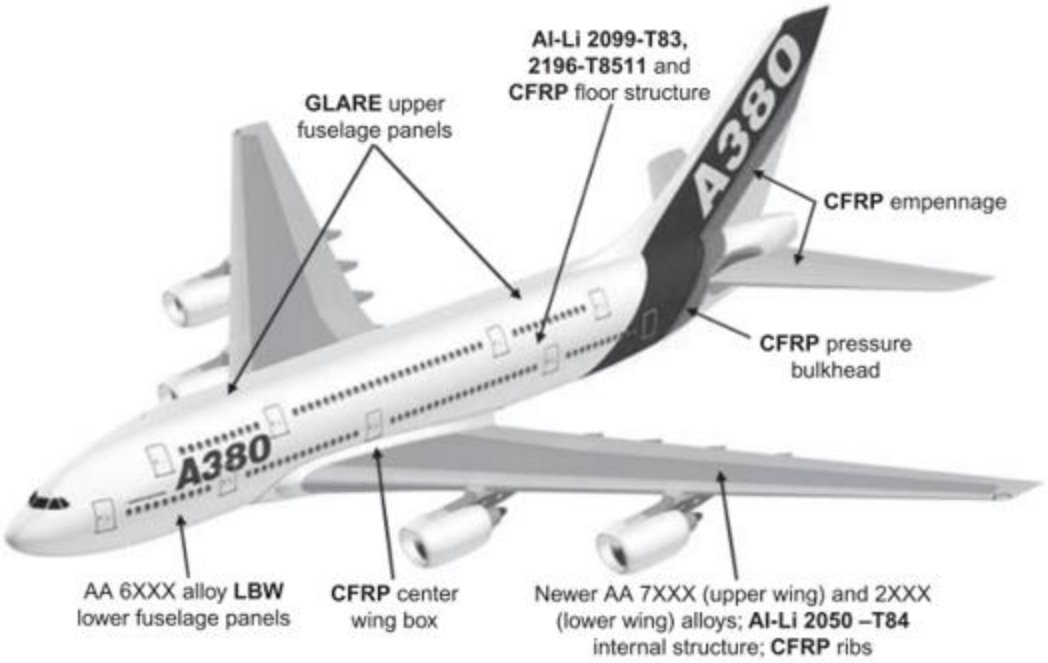

Figure 1.1 - Illustration of materials and processes applied in major structural areas of Airbus A380 [8]. GLARE (Glass laminate aluminum reinforced epoxy); CFRP (Carbon Fiber Reinforced Polymers); LBW (Laser Beam Welding).

The joining procedure of the materials can also influence the weight of the structure. Since welding processes may not require any material additions such as rivets used in the mechanical fastening techniques conventionally used in joining aircrafts parts, it can contribute in saving structural weight [9]. However, conventional welding has negative impacts on environment and introduces significant problems to some aluminum alloys due to the consequences of the high-energy process [9,10]. Moreover, melting of aluminum alloys can led to the evaporation of some solute atoms, as Li, heading to a loss of properties. A solution to avoid those problems is to use solid state joining technology [11–15].

Solid-state welding processes are conducted below the melting temperature of the substrate and therefore are especially suitable for aluminum

alloys where solidification problems can be avoided. Besides, the lower energy consumption as well as being environmental friendly has led Friction Stir Welding (FSW) to be classified as green technology [9]. A variation of FSW, where the difference is a second shoulder added on the process, is named Bobbin Tool Friction Stir Welding (BT-FSW). In both techniques, the contact between the tool and the material generates a complex heating and flow of the material that promotes the weld of the substrates. Therefore, the aim of this project is to understand how BT-FSW variants can affect the welded joint.

Thus, knowledge of how the variants of BT-FSW influence the microstructural and mechanical behavior of the weldments is essential to further improve the process and consolidate it as a reliable method for welding Al-Li alloys from series 2XXX.

This research was a result of a scientific and technological partnership between the Federal University of São Carlos (UFSCar) and the German research center Helmholtz-Zentrum Geesthacht (HZG), which is a reference in solid-state welding research.

2 OBJECTIVES

In the present work, the main objectives are:

1) Evaluating the microstructure and mechanical properties of two Al-Li alloys (AA2060-T8 and AA2196-T8) welded by Self-Reacting BT-FSW and by Stationary upper shoulder BT-FSW;
2) Investigating the correlation between energy input of SSuBT-FSW and SRBT-FSW on the mechanical properties of AA2060-T8 and AA2196-T8.

3 LITERATURE REVIEW

3.1 Aluminum Alloys

Aluminum has always been a metal of interest due to its low density and good corrosion resistance. However, pure aluminum has low mechanical properties and is only used in specific areas [1,16]. According to J. E. Hatch [17], over 100 of the existing elements can be used as alloying elements, but only 9 of them have a solubility higher than 1 wt.% in aluminum. Removing the most expensive and hard to process ones, the five remaining elements are the basis for all aluminum alloys, being them copper (Cu), magnesium (Mg), manganese (Mn), silicon (Si) and zinc (Zn) [18].

Balanced by the solid solubility of Al, its alloys can be classified in two groups: wrought and cast alloys. The main difference between these groups is the mix and fraction of alloying elements. Cast alloys often contain large amounts of silicon that assure the castability of the alloy. Cast alloys usually undergo a catastrophic loss of mechanical properties in high temperatures, above 300°C, while most of wrought aluminum alloys retain their mechanical properties and remain ductile within this temperature range. Wrought alloys contain lower percentages per additional element and is sufficiently ductile to be shaped by cold/hot work [18].

Wrought alloys can be divided in non-heat-treatable (solid solution strengthened) and heat-treatable alloys (precipitation strengthened). The first wrought group, also called work-hardened aluminum alloys, is characterized by the presence of dissolved elements in the matrix that leads to distortions in the crystal lattice. As the dislocation motion interacts with the solute atoms, their movement is inhibited, and a critical stress is necessary for the dislocation to overcome the solute element. A higher fraction of dislocations and solute atoms will lead to higher critical stresses and, therefore, higher forces necessary to deform the material. Then, mechanical properties of these alloys are controlled by a cold working step after alloying since work hardening promotes movement, multiplication and interaction of dislocations. A heat treatment of these alloys will

eliminate the effects of the work hardening process. Magnesium (5XXX) and manganese (3XXX) are the most extensively applied on this group [16,17]. Cold rolling, stretching, drawing or a combination of these processes are the main way of strengthening these alloys [18].

The second wrought group is strengthened by the presence of precipitates. The influence of the precipitate on the strength of the alloy depends on its type, size and distribution in the Al matrix. The type is determined by the chemical and crystal structure and sets the characteristics of the particle [13]. Some elements in cooperation with a controlled heat treatment can drive to the formation of specifics precipitates [19,20]. The size and volume fraction of these particles depends on the type, concentration and distribution of the chemical elements besides the heat treatment applied [13,19].

The development of precipitates depends on the presence of a solute and its solubility in the matrix, and on the individual mobility of these solute atoms. As solubility increases with temperature, higher amount of the solute can be found within the matrix at higher temperature. A fast drop of temperature (quenching) leads to a non-stable system where the solute concentration is higher than the one allowed on the matrix at room temperature (RT). This metastable condition is called a super-saturate solution (SSS). As most of science resumes to thermodynamic stability (minimum energy of the system), the extra amount of solute present in the matrix tends to move out of the aluminum matrix developing stable phases (precipitates). As atomic mobility depends on energy, some alloys will be able to form precipitates at room temperature (RT) called natural aging process and some will only form them at higher temperature (artificial aging) [21].

Initially, the solute diffuses through the matrix generating solute-rich cluster identified as Guinier-Preston zones. The increase of the concentration of alloying elements clustered within a small region creates a local change of composition that originates another phase (precipitate). At the beginning there is no distinct interface between the particles and matrix (coherent precipitate). The evolution of the precipitates through time generates a crystal structure change from the metal lattice (incoherent precipitates). The stages of precipitation are summarized by (Equation 3.1) [22].

Super-saturate solution (SSS) → Guinier-Preston zones (GP) → coherent precipitate (θ") → semi-coherent precipitate (θ')→ incoherent precipitate (θ) (Equation 3.1)

Precipitates increase the strength of materials by hampering dislocation movement. Thereafter, the dislocation has two options to keep moving- 1) cut through the particles; 2) bow around them (Orowan strengthening mechanism). The first mechanism tends to occur when the precipitate radius is small. The second one happens when the radius is large, and the particle is hard. The change between the mechanisms relies on the minimum energy consumption to realize the movement. Equations to quantify gain originated by precipitation hardening and a deeper explanation about the parameters that influences the process are described by Starink et al. [23], Seidman et al [24], and Gao et al [13]. Copper (2XXX), magnesium in combination with silicon (6XXX) and zinc (7XXX) are the most common alloying elements for heat-treatable aluminum alloys [16,17]. Figure 3.1 shows the conventional correlation between precipitation stages and hardening mechanisms.

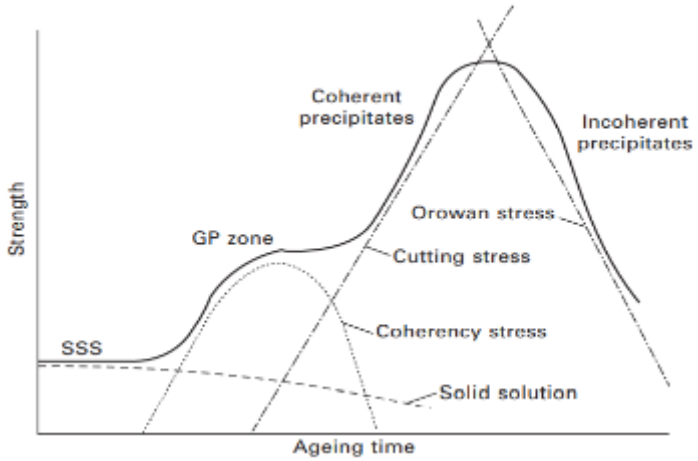

Figure 3.1 - Relationship between precipitation stages and strengthening mechanisms [22].

Besides the strengthening mechanisms described above as solid solution, precipitation and work hardening, there is another strength mechanism that is widely applied in metals, the grain boundary strengthening, also known as Hall-

Petch effect [25–27]. This mechanism is the unique that promotes the strengthening of the material without decreasing its ductility. The correlation between the grain size and the mechanical properties is described by Hall-Petch [28,29]:

$$\sigma_y = \sigma_0 + \frac{k}{\sqrt{d}}$$ *(Equation 3.2)*

where σ_y is the yield strength, d is the average diameter of the grains, k is a material constant and σ_0 is called the friction stress and it defines the stress required to move dislocations in a single crystal without a grain boundary. The Hall–Petch relationship is accurate for metals with a grain size between about 1 μm and 1 mm, but is not valid for materials with larger (>1 mm) or finer (<1 μm) grains [22].

While work-hardened alloys are classified by the deformation grade, heat-treatable alloys are classified in tempers. The basic designation includes O (annealed) and H (strain hardened) in addition to W and T (solution heat-treated alloys). At least a number, to specify the treatment received, follows this letter. Common tempers applied in aluminum alloys for aeronautics applications are T3 (solution heat-treated, cold worked, and naturally aged to a substantially stable condition), T6 (solution heat-treated then artificially aged) and T8 (solution heat-treated, cold worked, and then artificially aged) [17].

Mechanical properties of 2XXX, 6XXX and 7XXX aluminum alloy series largely varies according to applied temper and aging-time. Figure 3.2 shows the ultimate tensile strain of AA2198 varying from around 200MP to over 500MP according to the aging-time [30].

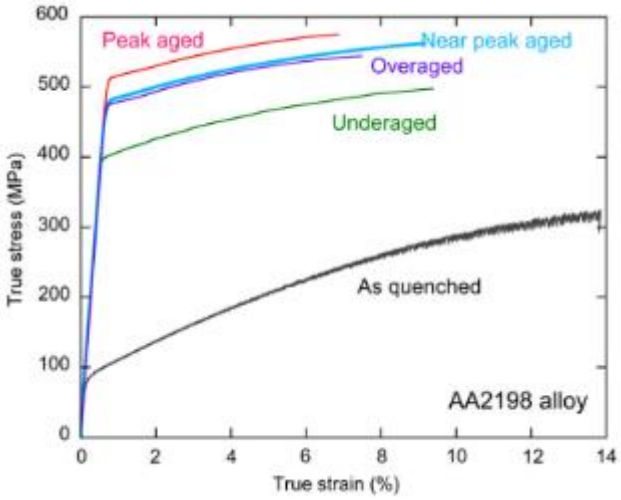

Figure 3.2 - Stress–strain curves of an Al–Cu–Li alloy for different aging condition in AA2198.

3.1.1 Aluminum – lithium alloys

The addition of lithium (Li) to aluminum (Al) has been studied since 1920 and three generations of Al-Li alloys have been developed. The last generation achieved a good balance between low density, increased corrosion resistance and high mechanical performance with low anisotropy that enables this group to be applied in aircraft and aerospace structures. The main components on this generation for aircraft applications are lithium (0.7 – 2.7 wt.%), copper (1.0 – 3.9 wt.%), zinc (0.2 – 1.0 wt.%), magnesium (0.2 – 1.3 wt.%), and manganese (0.1 – 0.5wt.%). The first one has significant influence in weight reduction and increase of elastic modulus. Cu combined with Li and Mg form the main strengthening precipitates. Zinc has impact in the fracture toughness and quench sensitivity of the alloy besides contributing to the corrosion resistance. Finally, Mn is responsible for controlling grain structure and crystallographic texture during thermo-mechanical processing [5].

Aluminum-lithium alloys from 2XXX series present complex precipitation sequence featuring aspects from Al-Cu and Al-Li systems [20]. The main strengthening precipitate is T_1 (Al_2CuLi), obtained only through artificial aging process. Common strengthening precipitates found in artificial and natural aged

Al-Li alloys are θ' (Al_2Cu) and δ' (Al_3Li) precipitates. Depending on the alloy composition and processing conditions, S (Al_2CuMg), T_2 (Al_6Li_3Cu), β' (Al_3Zr) or Tb ($Al_{7.5}LiCu_4$) precipitates can be also found [4,31]. Figure 3.3 presents an isothermal section of the ternary diagram of Al-Cu-Li system.

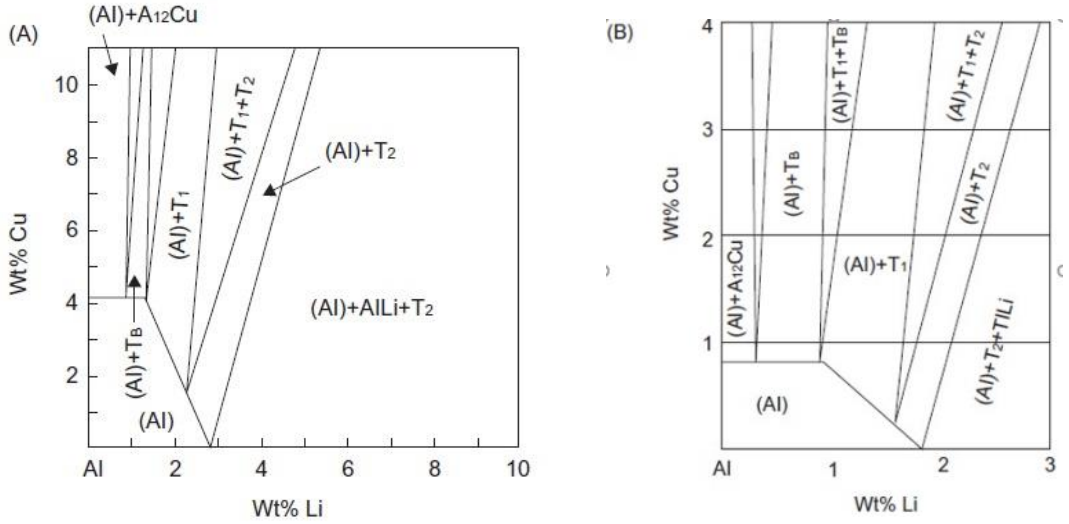

Figure 3.3 - Isothermal section of the ternary diagram of Al-Cu-Li system at (A) 500ºC and (B) 350ºC [32].

Figure 3.4 presents the microstructure of AA2060-T8 [33]. The image presented by Liu et al. shows that AA2060 at T8 condition has an elongated pancake-like non-recrystallized structure along the rolling direction, same as related by Cai et al. [34]. His work also identified significant amount of precipitates (δ', θ', T_1, S' and β'), dislocation loops and spirals as showed in Figure 3.4 b) to d).

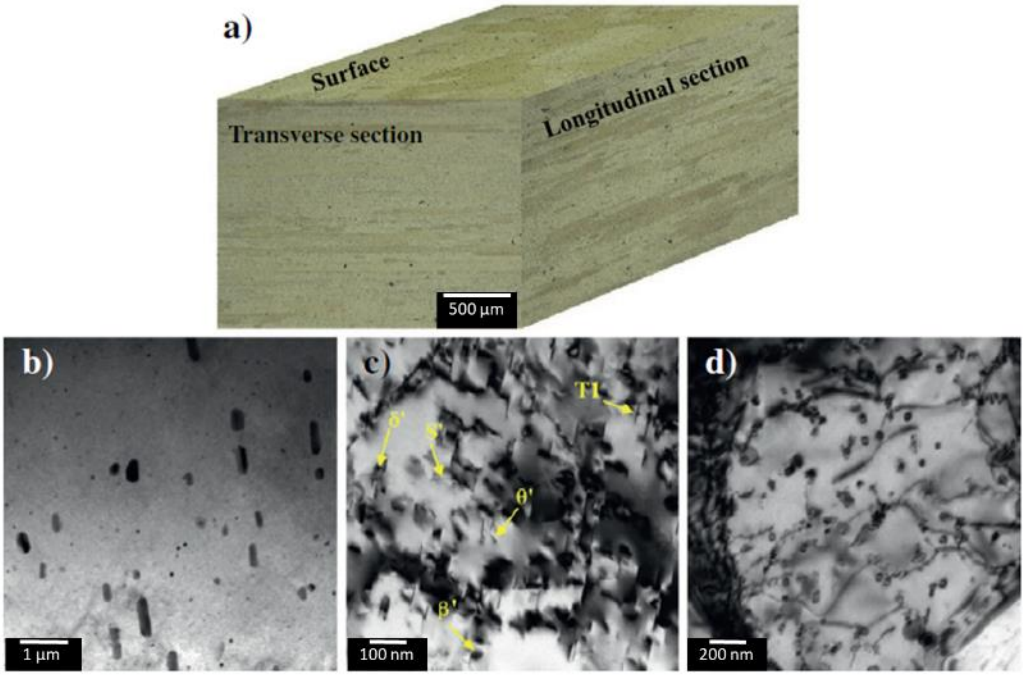

Figure 3.4 - Microstructure of the AA2060-T8 presented by: a) three dimensional optical micrograph; transmission electron microscopy images of b)–c) bright field and d) dislocation structures [33].

Decreus et al. [20] studied the precipitation sequence of AA2196 (low Cu/Li ratio) and AA2198 (high Cu/Li ratio) in T351 state (solution heat-treated, cold worked, and naturally aged to a substantially stable condition; residual stress relieved by stretching) varying the aging time at 155°C. Figure 3.5 presents the differential scanning calorimetry (DSC) graph constructed at their work. It was found that the first endothermic peak is associated with the dissolution of Cu-rich clusters for high Cu alloy (AA2198) and partial dissolution of δ' (Al_3Li) precipitates in Li-rich alloy (AA2196) in T351 state. This peak begins at about 200°C. The exothermic peak, which reach its maximum at around 300°C in AA2198 and nearly 400°C on AA2196, was related with precipitation of phases such as T_1 (Al_2CuLi).

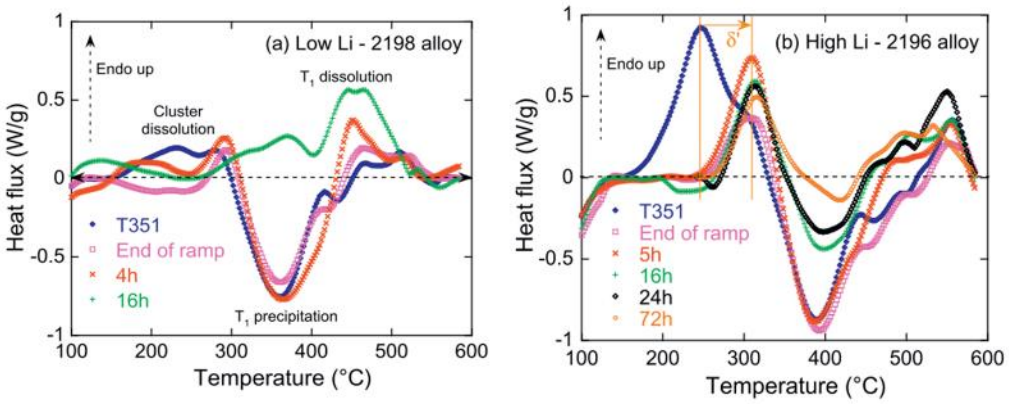

Figure 3.5 - Precipitation sequence of (a) AA2198 and (b) AA2196 in T351 temper varying the aging time at 155°C [20].

Decreus et al. [20] furthermore demonstrated that Cu/Li ratio influences the precipitation sequence and kinetics of Al-Cu-Li-x alloys. Their microstructure analysis during natural aging showed that high Cu/Li ratio alloy (AA2198) presented Cu-rich clusters, while in the Li-rich alloy (AA2196) δ`(Al_3Li) phase was dominant. During artificial aging experiments, samples of both alloys deformed prior heat treatment (T8 temper) mostly promoted T_1 precipitates. However, the low Cu/Li ratio alloy (AA2196) showed a longer incubation time and a larger saturation diameter of T_1 plates, what could mean a more difficult nucleation process [20].

Schneider et al. [35] studied the stir zone (SZ) in AA2195-T81 (solution heat-treated, cold worked, and then artificially aged; straightening or flattened after heat treatment). It was reported that in the material heat treated at temperatures in the range of 138 - 260°C (T81), T_1 precipitates prevailed. The increase of temperature to a range of 316 to 371°C resulted in a fast precipitation of θ and θ' (Al_2Cu). Finally, at temperatures above 482°C was stated that T_1 precipitates in the AA2195 alloy were dissolved instantaneously.

AA 2060 is a third generation Al-Li alloy containing 0.75 wt.% Li and 3.95wt% Cu, which makes a high Cu/Li ratio. This material present high strength/toughness relationship, good thermal stability, improved corrosion resistance and fatigue behavior. According to Rioja and Liu [2], AA2060 was developed for the application in fuselage sheet products and wings sections. AA 2196 has a low Cu/Li ratio, containing 1.75 wt.% Li and 2.9 wt. %Cu. In a T8511

condition, it has properties suitable for being applied on stringers of the fuselage/pressure cabin and on floor beams and seat rails [8].

3.2 Friction Stir Welding (FSW)

Structural materials often need to be joined with similar or dissimilar materials. As melting is the basis of all fusion welding methods, fumes of sublimated metals are produced during the process. This fumes are composed by metal nanoparticles that can be toxic and impact nature besides generating health issues [36]. In addition to conventional welding negative impacts on environment, some aluminum alloys are considered non-weldable due to the consequences of the high-energy process. These consequences can be porosity on the welded region (fusion zone), cracking, high level of residual stresses or poor microstructure generated until the heated affected zone heading to significant reduction of mechanical properties [9,10]. Moreover, melting of aluminum alloys can drive to the evaporation of some solute atoms, as Li, leading to a loss of properties [11–15].

A solution for avoiding the problems created by fusion welding aluminum alloys was presented by The Welding Institute (TWI) in 1991. The alternative invented by TWI was joining these alloys using a solid-state process. The basic idea was to rotate a non-consumable tool into the workpieces, and then the frictional heat generated by the contact plasticize the metal. When the probe is inside the work pieces, the rotational and translational movement of the tool extrude material around the pin, removing plasticized material from the front of the probe and consolidating the weld behind it [9,11,12]. Friction Stir Welding uses a shoulder and a probe as original tool. The shoulder main function is to generate most of the frictional heat and to keep the plasticized material under the process area. The rotational probe is responsible for contribute with additional heat and to movement the softened material around itself. In addition, the probe brings the intermixing to deeper regions, allowing the joining of thick plates

[9,11,12]. An illustration of the conventional FSW process is presented on Figure 3.6.

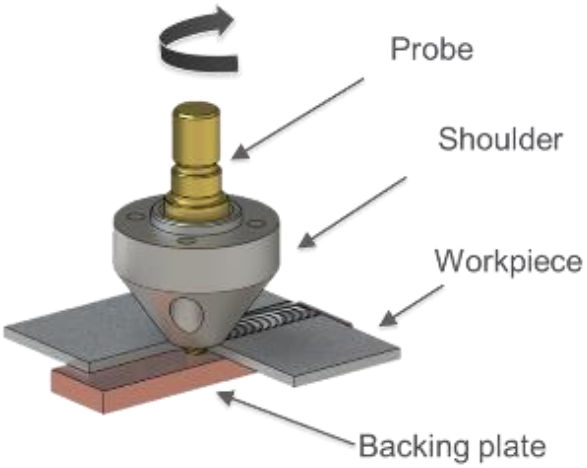

Figure 3.6 - Schematic illustration of conventional FSW. *Image courtesy of Jannik Goebel at Helmholtz-Zentrum Geesthacht.*

Material joined by FSW does not melt, but it is subjected to intense deformation and high temperature, what leads to microstructural changes. The area in direct contact with the probe, known as stir zone (SZ), experiences the highest level of deformation and energy input resulting in intense dynamic recrystallization. Therefore, this zone is characterized by fine and equiaxed grains [9].

Adjacent to the SZ, a thermomechanical-affected zone (TMAZ) is found. Highly deformed, but not recrystallized grains characterize the TMAZ. Finally, the last area affected by the process is known as heat affected zone (HAZ). As the name describes, this area is only thermally affected. Generally, grain size analysis do not show a significantly difference between HAZ and base material (BM), but mechanical tests expose the influence of the technique on this zone [9,37].

Besides the grain transformations, precipitates and intermetallic phases experience variation on the size and distribution of these particles. When a complete dissolution occurs, new precipitates might form during cooling that can even be different from the pre-welded ones. In general, SZ presents major dissolution of precipitates due to the highest temperatures driving to a natural

aging process post welding. TMAZ experiences some dissolution and overaging of these particles, and HAZ present mainly precipitate overaging [38].

3.2.1 Bobbin tool friction stir welding (BT–FSW)

To eliminate the necessity of a backing plate and to increase the flexibility of the FSW technique, a lower shoulder was added in a process variant called bobbin tool friction stir welding (BT-FSW). The BT-FSW concept was present on the original patent created by TWI in 1991. In this variant, the forging forces necessary to restrain the material act between the two shoulders and the probe carry the process loads [12,39,40]. A diagram of this variant is present in Figure 3.7. In addition, defects such as root flaws or lack of penetration occasionally reported in standard FSW are avoided by the full penetration offered by the method [31].

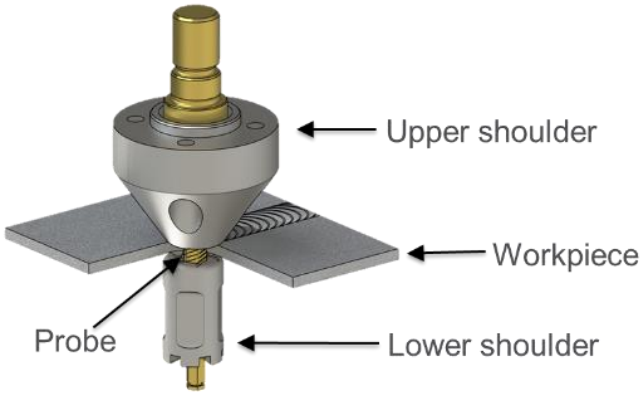

Figure 3.7 - Schematic illustration of BT-FSW. *Image courtesy of Jannik Goebel at Helmholtz-Zentrum Geesthacht.*

Initially, the BT-FSW tool was a unique piece with a fixed gap size between the shoulders. Then, a force controlled auto-adjustable probe tool was invented, allowing an adjustable gap size during the process [12]. The understanding of the process parameters, tools design and materials supported the creation of new FSW variants using the BT. These derivatives are: Self – Reacting Bobbin Tool–FSW (SRBT-FSW), Stationary Shoulder BT-FSW (SSBT-FSW) and Stationary (upper or lower) Shoulder BT-FSW (SSu/lBT-FSW), where both, none or only

one of the shoulders rotates during the process [31,41]. Figure 3.8 shows a schematic illustration of BT-FSW variants.

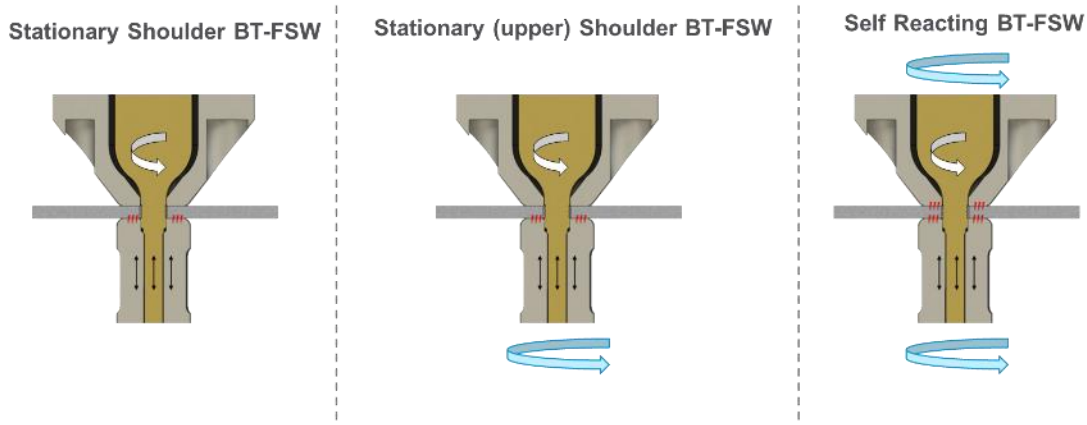

Figure 3.8 - Schematic illustration of BT-FSW variants. *Image courtesy of Jannik Goebel at Helmholtz-Zentrum Geesthacht.*

Self – reacting bobbin tool (SRBT-FSW) is a force-controlled process where the gap between the two shoulders can vary during the welding. Then, the method can withstand thickness variations of the base materials and compensate differences between the thermal expansions of probe and workpiece [41]. As the main heat produced is generate by the friction between shoulder and weldments [9], the extra heat originated by the lower shoulder influences the final microstructure of the joints. An hourglass shape stir zone represents the standard macrograph of a SRBT-FSW, as shown in Figure 3.9. Due to the described transformations during welding process, a typical W-shape hardness profile is found in 2XXX, 6XXX and 7XXX alloys joined by FSW and its variants, as showed by Figure 3.10 [34,42–44].

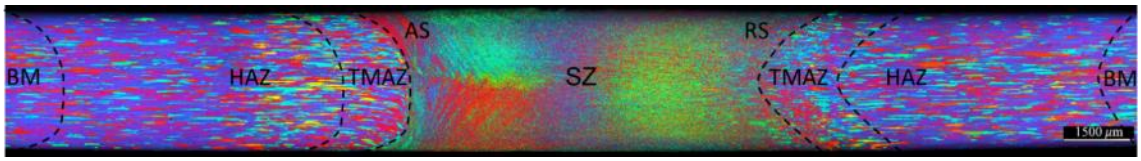

Figure 3.9 - Macrograph of SRBT-FSW in AA2060 showing the indications of the weld zones and BM.

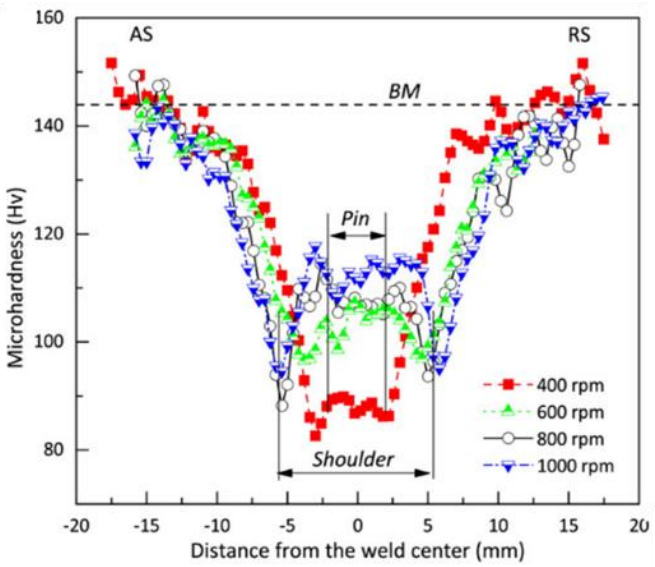

Figure 3.10 - Hardness profile of AA2198 welded by BT-FSW varying rotational speed [42].

The stationary shoulder concept was developed with the intention of reducing the frictional heat produced by the rotation of both shoulders in contact with the material surface, and only generate energy by the friction caused by the rotating probe in contact with the weld [41]. Consequently, this process would reduce the energy input on the material and also avoid through-thickness temperature gradient often observed when BT-FSW welding thick low thermal materials [44]. In addition, a stationary shoulder technique can reduces the inhomogeneity textures caused by the conventional BT-FSW and FSW process in the SZ, as the textures originate by the shoulder and probe (also known as pin) are different [45]. However, as the probe must support most of the loads and generates the energy to plasticize and movement the material, this technique faces significant challenges regarding tool material and design [31,41].

The partially stationary shoulder variation was originated as a combination of the two variants above described. Alongside the lower heat input that represents changes in the microstructure evolution, the sliding movement of the stationary shoulder produces a better surface finishing that could avoid post-processing and be interesting for some industrial applications [31]. Figure 3.11 shows a typical macrograph of a SSuBT-FSW weld. Figure 3.12 shows the typical

W-shape hardness profile found in AA2060 and AA2196 alloys joined by SSuBT-FSW [46].

Figure 3.11 - Macrograph of SSuBT-FSW in AA2060 showing the indications of the weld zones and BM.

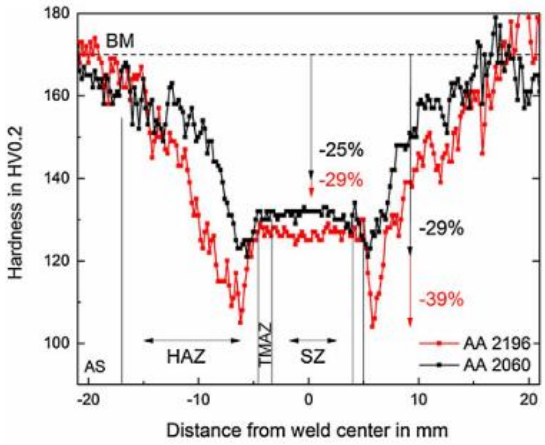

Figure 3.12 - Hardness profile of SSuBT-FSW in AA2060 and AA2196 showing the indications of the weld zones and BM [47].

3.2.2 Process parameters

As described by Mishra and Ma [9], the energy input and the plastic deformation caused by the friction welding processes cause complex material movement. This complex movement is affected by the welding parameters (rotational (ω) and traverse speed (v), pressure, angle of spindle), tool geometry and design (probe and shoulders diameter, presence of features, flutes or threads), joint design, alloy and thickness of the parent material. In BT-FSW is important to note that the pressure is between the shoulders. Cooling or pre-heating of the base material can be necessary according with the material properties (melting point and thermal conductivity) and influence the material

movement. Consequently, all these factors influence the microstructural evolution of the material.

The main welding parameters are rotational and traverse speed. Increasing the rotational speed (ω) will increase the friction heating, generating a more intense stirring and mixing of the material. On the other hand, increasing the traverse speed (v) will decrease the time the tool keeps in contact with the material, reducing the energy input. Increasing the vertical pressure (between shoulders in BT-FSW) will increase the contact between the shoulder and the substrate, leading to an increase on the weld temperature. An excessive pressure can led to depressions and excessive flash formation [9,48].

As demonstrated by Wu et al. [44], the processes parameters windows were limited by the energy input in BT-FSW and conventional FSW of high strength aluminum alloys. A high-energy input drives to overheating, initiating local material melting and defects. Otherwise, a too low input provokes probe failure due to excessive loads on it caused by high material shear strength when the material is not enough plasticized. A few works compared FSW and BT-FSW, as Lampeas and Diamantakos [49] and Esmaily et al. [10]. They concluded that differences between the processes were determined by the variances in thermal history caused by dissimilar heat accumulation and dissipation. A common equation to estimate energy input per length (Es) is defined by:

$$Es = M\,\omega/v \quad \textit{(Equation 3.3)}$$

where torque (M), rotation rate (ω) and traverse speed (v) are taken into consideration [50]. As the energy input is determined by the process parameters, mainly rotational speed, traverse speed and torque, it is not possible to compare standard and stationary shoulder processes with the same welding parameters. Thus, the best working parameters for each variant needs to be used to demonstrate and compare the principles of both processes [10,31,44]. Figure 3.13 summarizes the influence of welding parameters on the weld quality.

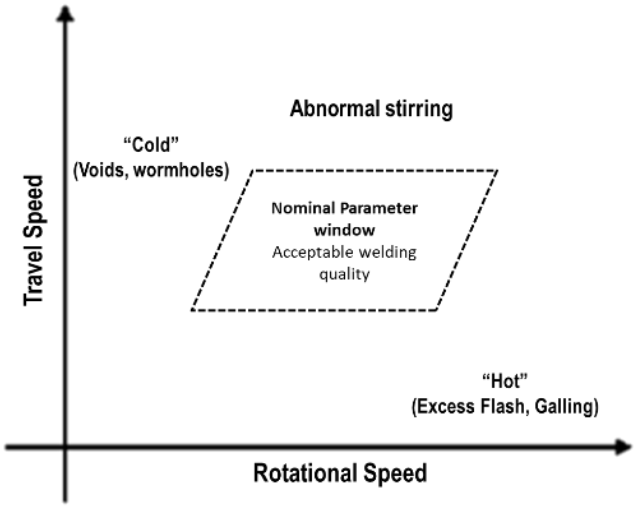

Figure 3.13 - Operational Friction Stir Welding parameters [51]. Travel speed, welding speed and traverse speed have the same meaning, i.e., the speed that the tool moves through the plate during the welding.

3.2.3 Welding Features

The onion rings marks are the most characteristic surface feature in FSW processes of aluminum alloys. These marks have been related to an extrusion process that occurs around to the retreating side (RS) of the tool when the probe moves forward [52]. In addition, Krishnan [52] concluded that the space between the marks is equal the weld pitch ratio (also known as the revolutionary pitch), this means, the tool advance per rotation (traverse speed (v) divided by the rotation rate (ω)). Moreover, it was reported, through electron back scattered diffraction studies of AA2024 welded by FSW that the density of second-phases particles differ between the bands more than any significant difference in the local grain structure or texture [14].

The main difference found when comparing SSuBT-FSW and SRBT-FSW is an ironing effect of the upper surface in SSuBT-FSW. According to Goebel et al. [31], the stationary shoulder acts as a moving anvil plate and compresses the material, which has been previously plasticized by the probe. As a result, the characteristics semicircular marks (often reported as onion ring marks) [9–

11,14,31,41,52,53] are flattened to a better surface finish. This effect can be seen in Figure 3.14.

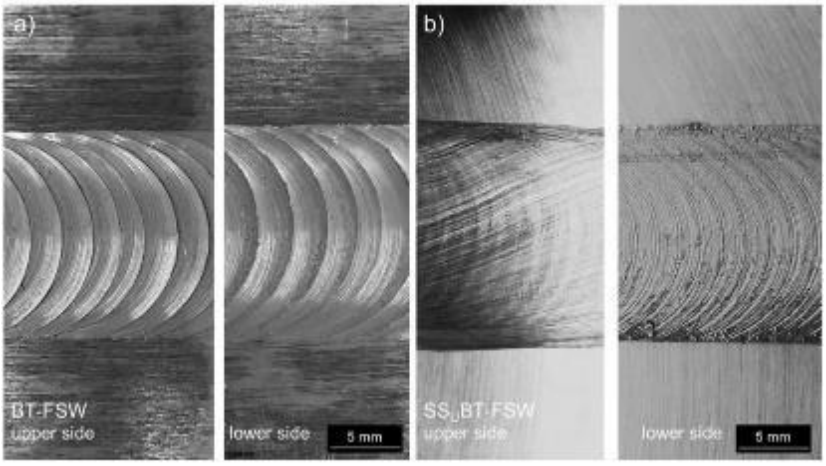

Figure 3.14 - Surface appearance of Al-Li-Cu alloy (AA2198-T851) welded by (a) standard BT-FSW and (b) SSuBT-FSW [31].

3.2.4 FSW typical discontinuities

FSW typical discontinuities are volumetric discontinuities as voids localized at the interface of TMAZ and SZ [54] caused by insufficient material flow, root defects caused by incomplete penetration of the probe, and excessive flash formation due to a deep position of the tool and/or excessive axial force [9]. Volumetric discontinuities often arise due to a combination of low rotational speed and high welding speed. They are avoided by a correction of the shoulder penetration, which will act on the forge force, in addition to the ideal parameter selection, such as rotational and weld speed that will ensure a normal flow of the material [54]. Figure 3.15 shows a macroscopic cross-section image of a void discontinuity in a 304 SS (stainless steel) caused by the lack of consolidation of the material inside the stir zone (also known as weld nugget, mainly in conventional FSW) [55].

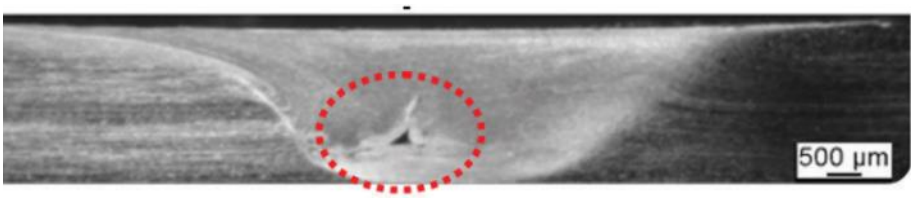

Figure 3.15 - Macroscopic cross-section image of a void discontinuity in a 304 SS caused by the lack of consolidation of the material inside the weld nugget [55].

Root flaws, as the one presented in Figure 3.16, are caused by no full consolidation at the bottom side of the root weld, due normally to inadequate probe length. Discontinuities in the root can also be caused by poor control of tool position/force, local variations in plate thickness, or by local cooling caused by the massive heat sink often provided by the tool bed [56]. Figure 3.17 present excessive flash found in some materials welded by FSW.

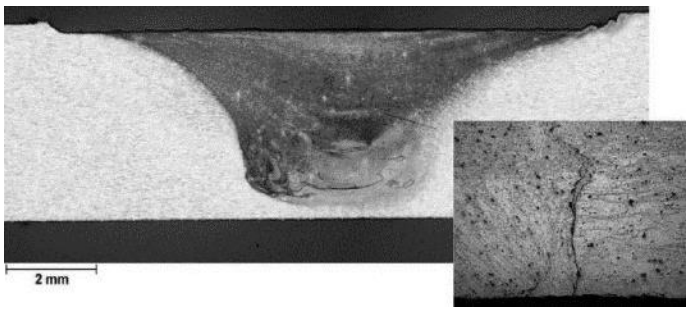

Figure 3.16 - Root defect in a 4mm thick AA2024-T351 welded by FSW due an insufficient penetration of the probe [57].

Figure 3.17 - Top view of AA2XXX welded by FSW showing excessive flash formation on the side of the weld. *Image courtesy of Helmholtz-Zentrum Geesthacht.*

As described in literature [9,31,33,39,54,58–62] for similar Al alloys welded by FSW and BT-FSW, advancing side (AS) is a critical location for discontinuities

formation. This is originated by the nature of the process, where plasticized material is removed from the AS, sheared around the front of the probe and extruded via RS to the tailing side of the tool. On the tailing side, the plasticized material is released in high velocities from the probe, refilling the empty space originated by the tool and creating a sharp transition between the SZ/TMAZ on the AS, as observed in Figure 3.18 [31,41,59,63,64].

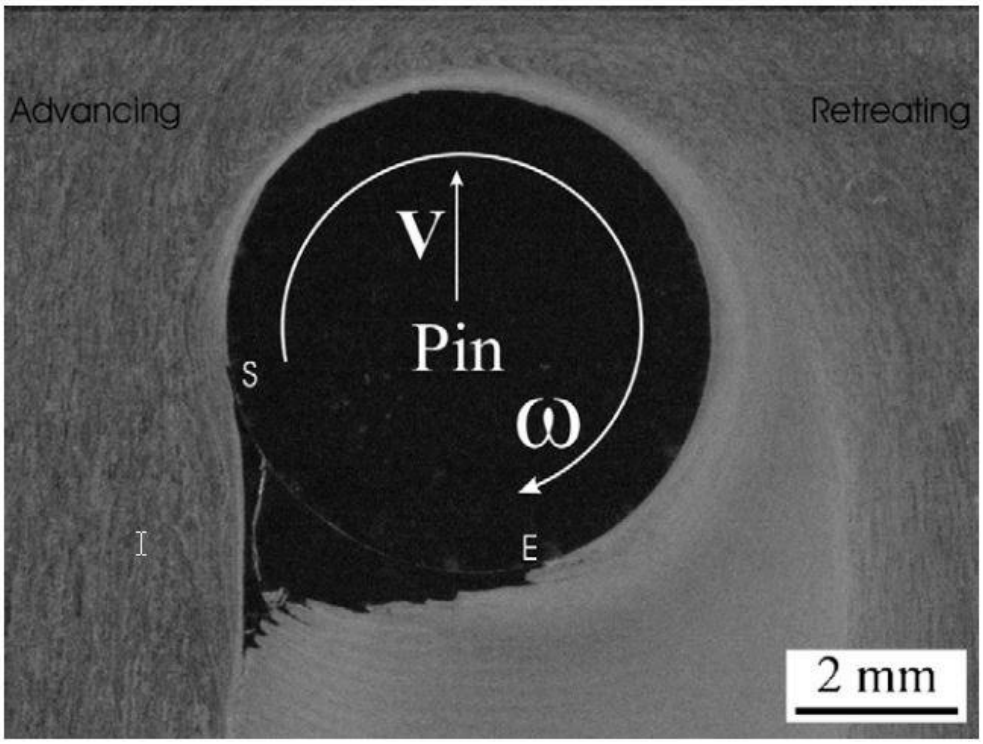

Figure 3.18 - A longitudinal cross-section of a weld plate with the broken pin embedded, taken along the mid-plane (sectioned plan parallel to the plate) [63].

Discontinuities that can occur in the welds after BT-FSW are lack of consolidation and volumetric discontinuities at the surfaces due to non-optimal parameters causing insufficient material flow [31]. In addition, some authors reported material loss due to entrapment in the tool between the shoulders and the probe. The occurrence of such is mostly problematic in the stationary shoulder BT-FSW (both shoulders stationary) [12,41]. Typical volumetric flaw observed in SSuBT-FSW are due to inadequate material flow and occurs mainly on the top surface of advancing side (AS). It is caused by the asymmetrical

character of this variant that forces a vertical material flow upwards the stationary shoulder. The flow is induced by the lower shoulder movement as well as by the threaded probe. Material flow and volumetric critical locations in SRBT-FSW and SSuBT-FSW is showed in Figure 3.19 [31].

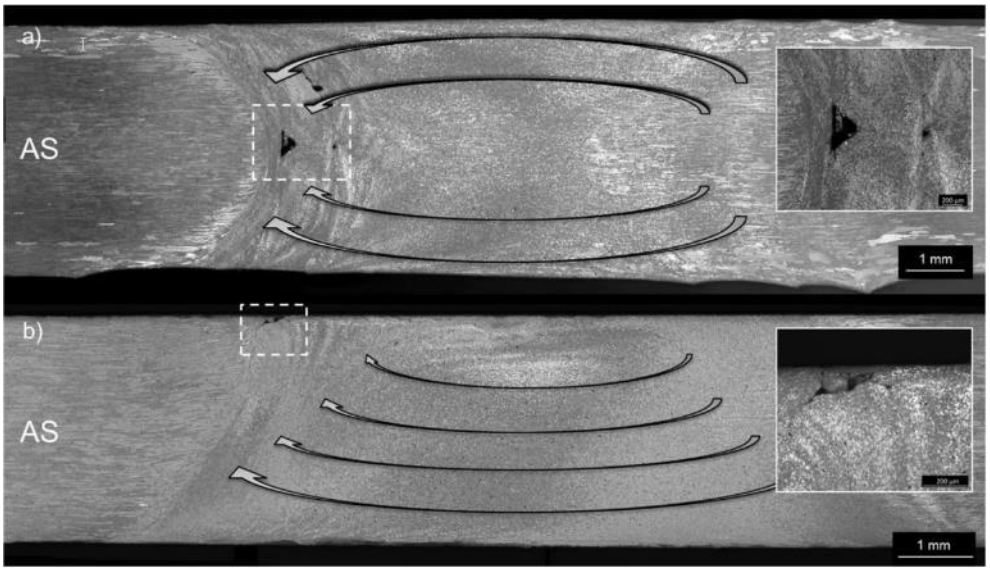

Figure 3.19 - Material flow and volumetric critical locations in (a) SRBT-FSW and (b) SSuBT-FSW welds [31].

3.2.5 Fracture behavior of 2XXX aluminum alloys under FSW variants

As reported, the mechanical behavior of Al-Li 2XXX alloys under FSW variants, including BT-FSW, is widely affected by the process [33,42,56,65,66]. A significant loss of strength takes place in the weld area of these alloys, mainly in HAZ and SZ due to overaging and dissolution of precipitates, as described before on this text. Additionally, the degradation of the material in solid state welding is less aggressive than in fusion welding processes, that involves higher heat inputs [11].

Liu at al. studied the tensile properties and fracture locations of conventional FSW weldments of 2017-T351 aluminum alloy [65]. It was found that a softened region, comprising the SZ and the HAZ, caused lower tensile properties than those of the base material. They compared the mechanical results of the different parameters considering the revolutionary pitch, also known as

weld pitch. They observed that when the revolutionary pitch was high (at their work, high was a definite value above 0.13 mm/rev) some void discontinuities existed in the joints, the tensile properties of the joints were considerably low, and the joints fractured at the weld center. Otherwise, in a defect free joint, the welds fractured near or at the interface between the SZ and the TMAZ on the advancing side (AS). At their found optimum condition, a revolutionary pitch of 0.07 mm/rev, the maximum ultimate strength achieved was equivalent to 82% that of the base material.

Wang et al. studied the effect of tool rotational speed on the microstructure and mechanical properties of SRBT-FSW of AA2198-T851 [42]. They found three fracture modes defined as mode I, mode II, and mode III. In mode I, failure occurred inside the SZ, but the crack initiation sites do not correlate to any softened regions within the SZ. However, if the respective weld macrographs were considered, the initiation sites coincided with the joint line remnant (JLR), commonly observed as remnant oxide films originated from the butt interface during welding. In mode II, failure occurred at the HAZ. That was related with a higher stir rate caused by a higher rotational speed that created a more scattered JLR region, making the lower hardness region, HAZ, more favorable for the crack initiation. In mode III, failure occurred at the border of the TMAZ/SZ. At higher welding speeds, the area of the softest region was very limited favoring minor discontinuities, such as the border of the TMAZ/SZ, as a susceptible crack initiation zone.

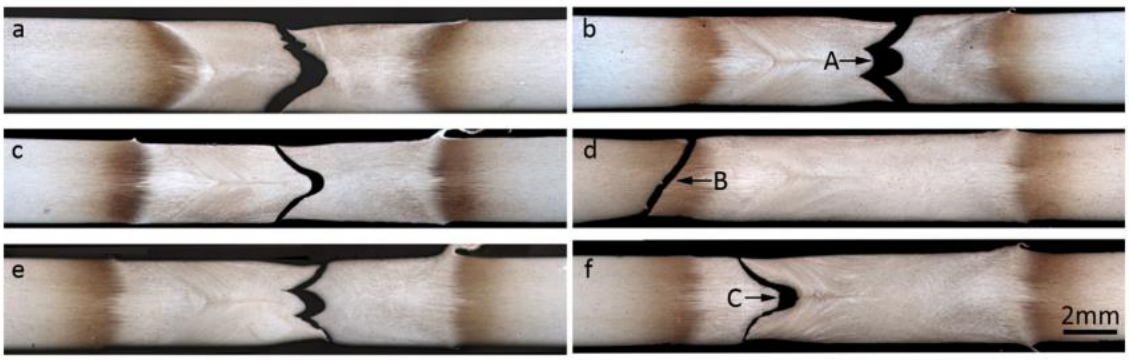

Figure 3.20 - Typical fracture locations of AA2198-T851 joints at different rotational speeds of BT-FSW: (a) 400 rpm; (b) 600 rpm; (c–d) 800

rpm; and (e–f) 1000 rpm. Mode I, II and III were showed as arrows A, B and C, respectively [42].

Goebel et al. researched SSuBT-FSW of AA2198-T851 [31]. They found two fracture modes described as mode I and mode II. Fracture mode I showed a shear mode fracture on the AS of TMAZ/SZ border. The fracture path followed the border between the SZ and the TMAZ, in an almost 45° angle. The paper indicated mode I fracture as a competing weakening mechanism located at the SZ/TMAZ border on the AS related to the high misorientation observed in the AS for FSW. Mode II fracture occurred in the HAZ, weakest point in the hardness distribution, and followed a 45° path. They related the fracturing in a shear mode from the SZ as a softening due to thermal effects. Mode I occurred in regions where temperatures of 519°C were assumed and mode II where temperatures of 350°C were measured. Mode II, occurred at 6.0 to 7.6 mm from the weld center, where the heat input caused considerable changes in the precipitation state resulting in the lowest measured hardness.

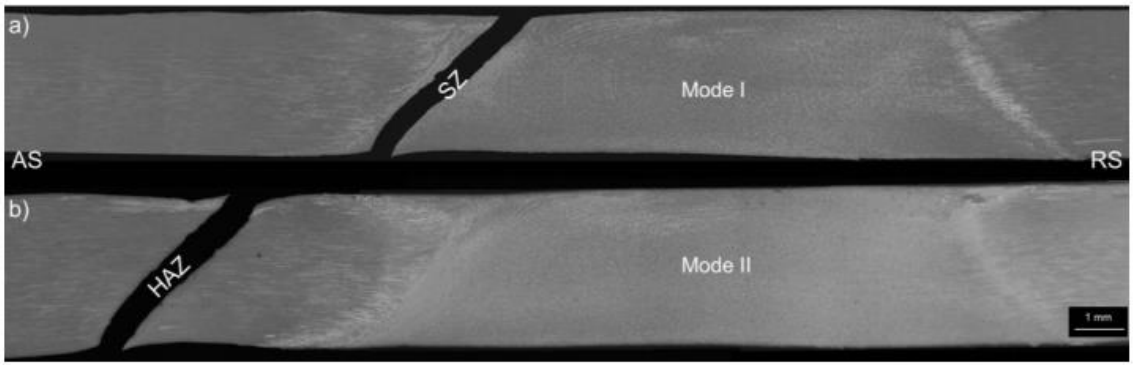

Figure 3.21 - Fracture modes for SSuBT–FSW of AA2198 - T8: (a) mode I - inside SZ, in the AS of TMAZ/SZ border ; (b) mode II - in HAZ of AS [31].

4 MATERIALS AND METHODS

4.1 Materials

Two Al-Li alloys were studied in this work, AA2060 and AA2196. The chemical composition of both alloys was determined by X-ray fluorescence spectroscopy plus additional inductively coupled plasma optical emission spectrometry for the light elements Li and Ag and it is listed on Table 4.1.The mechanical properties of the base materials at room temperature in T8 condition (solution heat treated, cold worked, and artificially aged) were measured and the average value is given on Table 4.2.

Table 4.1 - Nominal chemical composition of AA2060 and AA2196 Al-Li alloys given in wt.%.

Alloy	Cu	Li	Zn	Mg	Mn	Ag	Al
AA2060	4.2	0.9	0.36	0.85	0.32	0.36	Balance
AA2196	2.9	2.0	0.05	0.38	0.32	0.28	Balance

Table 4.2 - Mechanical properties of base materials: AA2060 - T8 and AA2196 - T8.

Material	UTS	YS	Hardness	Elongation at fracture
AA2060-T8	516 MPa	447 MPa	169 HV	12,6%
AA2196-T8	549 MPa	513 MPa	169 HV	16,4%

Butt joint welds were produce using sheets measuring 300 x 75 x 3 mm for both SSuBT-FSW and SRBT-FSW variants. The analysis of the microstructure of the base materials in the longitudinal (rolling direction), transversal short (thickness) and transversal long (width) directions showed that AA2060-T8 is consisted of large pancake grains while AA2196-T8 is composed by large elongated grains, both flatted in the rolling direction as showed by Figure 4.1.

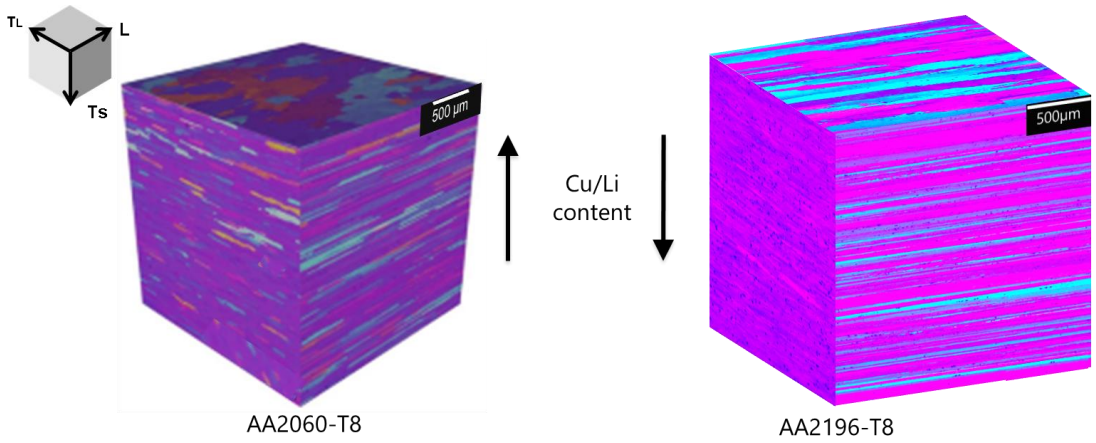

Figure 4.1 - Base material cube showing microstructure in the longitudinal (rolling direction), transversal short (thickness) and transversal long (width) directions.

4.2 Methods

4.2.1 Welding

Three millimeters thick plates of Al-Li alloys AA2060 and AA2196 were welded on a five-axis parallel kinematic robotic PKM T805 machine equipped with a custom design BT-FSW spindle. The tools consisted of a 7 mm nickel-cobalt (alloy MP159) probe with inclined features and two 15 mm diameter shoulders made of molybdenum-vanadium hot work tool steel ($X_{38}CrMoV_{5\text{-}1}$). The rotating shoulder had symmetrically scrolled features, whereas the stationary shoulder was featureless.

Figure 4.2, Figure 4.3 and Figure 4.4 show the probe, shoulders and robot used during this project, respectively.

Figure 4.2 - Image of probe used during welding. *Image courtesy of Helmholtz-Zentrum Geesthacht.*

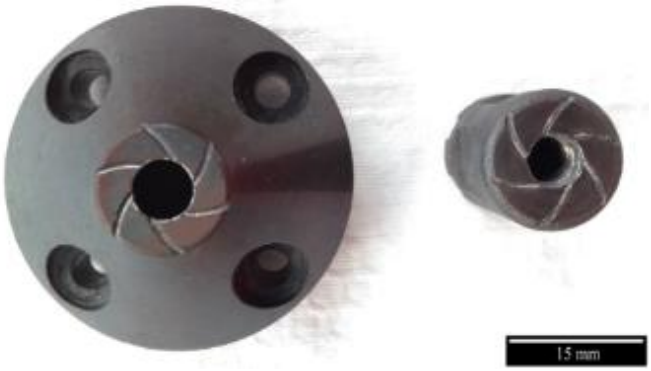

Figure 4.3 - Image of upper (left) and lower (right) shoulders used during welding. *Image courtesy of Helmholtz-Zentrum Geesthacht.*

Figure 4.4 - PKM T805 machine equipped with a custom design BT-FSW spindle. *Image courtesy of Helmholtz-Zentrum Geesthacht.*

Parameters were chosen based on previous group studies considering Design of Experiments (DoE) approach of AA2060 and then transferred to the AA2196 alloy. The process parameters chosen for analysis were rotation and traverse speed, being torque an answer of the robot. The samples were visually inspected, and a range of values was found where the welds were defects free. Parameters were hold similar for better comparison between AA2060 and AA2196 in SSuBT-FSW. For SRBT-FSW, the parameters windows were not found to overlap, then the best working parameters for each alloy were chosen.

For SSuBT-FSW, welding parameters were adjusted to 150 RPM at a traverse speed of 125 and 150 mm/min and a gap force of 5700 and 5500 N. For SRBT–FSW welds, all the welds were run at 400 RPM with the gap force and traverse speed being adapted for each material and energy level. The process parameters are shown in Table 4.3 and Table 4.4.

Table 4.3 - Welding parameters during SSuBT-FSW.

SSuBT-FSW	AA2060	AA2196
High Energy	150 RPM - 5700 N - 125 mm/min	
Low Energy	150 RPM - 5500 N - 150 mm/min	

Table 4.4 - Welding parameters during SRBT-FSW.

SRBT-FSW	AA2060	AA2196
High Energy	400 RPM-5140 N-571mm/min	400 RPM-5500 N-600 mm/min
Low Energy	400 RPM-5630 N-800mm/min	400 RPM-5500 N-800 mm/min

After the welds had been produced, samples were cut off and embedded for future microstructural analysis. Tensile, hardness and corrosion test were performed after natural aging. Furthermore, a calorimetric measurement was performed in different regions of the weld (base material, HAZ and SZ) in order to better understand the effect in microstructural evolution.

4.2.2 Thermal cycle measurements

Temperature measurements were performed embedding four k-type thermocouples at mid-thickness of the aluminum alloys sheets. Four positions were set in order to evaluate the thermal history in different zones of the welds - 3.5mm, 6mm, 9mm and 20mm from the weld center. The temperature measurements were taken after 100mm of welding when the welding conditions, result of the welding robot, process parameters and alloy, was stabilized. Since minor variations in thermocouple position led to significant effect on the recorded temperature, the exact final position after welding was determined via metallographic methods.

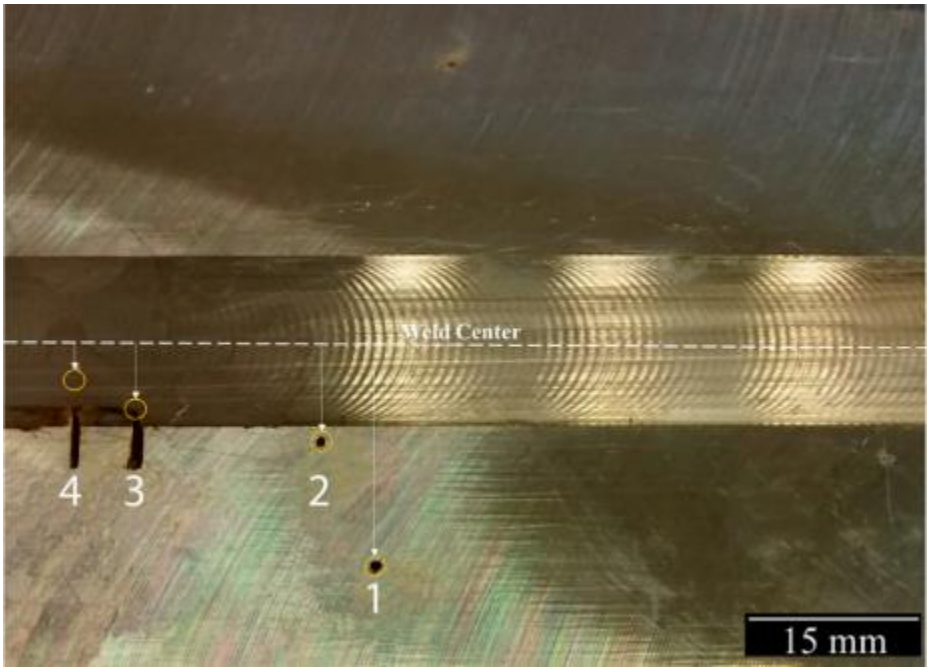

Figure 4.5 - SRBT-FSW high energy sample indicating thermocouples position where 4, 3, 2 and 1 are located at 3.5, 6, 9 and 20 mm, respectively, from the weld center.

4.2.3 Metallographic characterization

In order to analyze the microstructure of the weldments, all samples were inspected in an optical microscopy (Leica DM IRM). The samples were cut in transversal section using the Elektra Beckum machine to 25 mm width and embedded using a Demotec 30 resin. The embedded samples were grinded and polished in an automatic Struers Tegramin-30, according to metallography procedure for aluminum. The polished samples were etched using a 3 vol.% solution of HBF_4, known as BARKER solution, at 22V for 90s.

Images with a magnification of 1000x were used to measure the grain size of the materials inside the stir zone. This measurement was performed using the Intercept Count Method of ASTM E-112. The intercept count method is defined by counting the number of grains or number of grain boundaries intercepted by test lines of previously known length. As this test is recommended particularly for

all structures that depart from the uniform equiaxed form, the number of grains per unit length will determine the average grain size.

The average zone size was estimated by combining the analysis of 50x magnification images and hardness test results. It was measured on the sample middle thickness, pondering the shape of the grains (equiaxed and deformed). Image J software was used to perform the measurements.

4.2.4 Hardness profile

Hardness testing (Vickers) was performed in a Zwick/Roell ZHV machine with TestXpert software. The applied load was 200g (HV0.2) for 10s for all the samples, as in accordance with the standard ASTM E92-16. The hardness profile was measured in a line across the sectioned samples with indentations space of 0.3mm.

4.2.5 Tensile test

Tensile tests were performed at room temperature using a screw-driven Zwick-Roell Z100 testing machine with a load capacity of 100kN, MTS 634.25F-24 extensometer with a gauge length of 50 mm and TestXpert software. In accordance with ISO 6892-1-2009, the specimens were tested perpendicular to the sheet welding direction with a constant cross head speed of 1mm/min. Tensile specimen is shown on Figure 4.6.

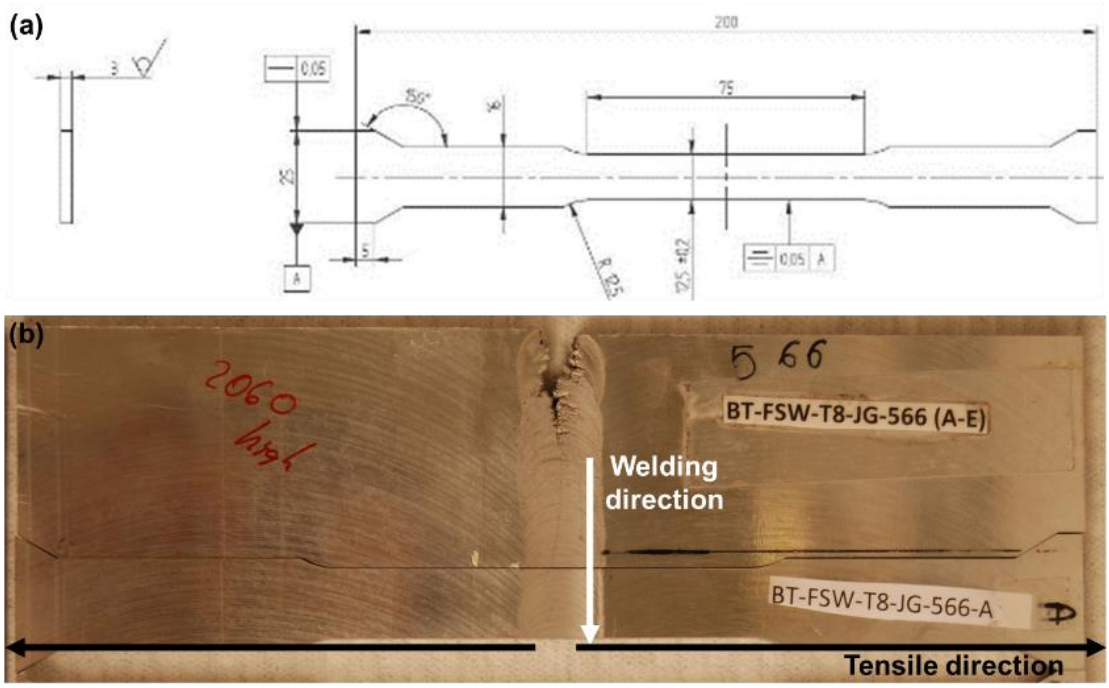

Figure 4.6 – Tensile sample (a) dimensions and (b) test and welding directions. *Image (a) is a courtesy of Jannik Goebel at Helmholtz-Zentrum Geesthacht.*

4.2.6 Fracture analysis

Fracture surface analysis were performed using a FEI Quanta 650 FEG scanning electron microscope (SEM). In addition, fractured samples were embedded using a Demotec 30 resin and polished in an automatic Struers Tegramin-30 to analyze the fracture mode (position and crack path).

4.2.7 Differential Scanning Calorimetry

Differential Scanning Calorimetry (DSC) analysis was carried out in a Netzsch DSC 200 F3 Maia. The specimens were heated from a 15 minutes isothermal step at 25°C to 590°C with a heating rate of 10°C /min. The obtained data for AA2060 and AA2196 samples were corrected via baseline subtraction and normalized to sample mass. DSC cell was placed under a nitrogen flow

atmosphere to minimize oxidation. None of the pans used were sealed to prevent rise of internal pressure.

DSC measurements were performed on 5mm diameter disks with 1.5 mm thickness. In the characterization of SZ, the disc-shaped specimens were extracted from a 3 mm thick weld by cutting and grinding to a final mass of around 70mg. All surfaces were grinded up to 1200 mesh SiC paper in order to ensure same surface finish. HAZ specimens were cut to a customized shape due its position in the weldments. A 90° tilt was necessary to ensure minimal scatter as the HAZ features a heterogeneous microstructure. The customized shape is like an ellipse with a flat lateral, as shown on Figure 4.7 (right). The dimensions are 1.5 x 3 x 5mm.

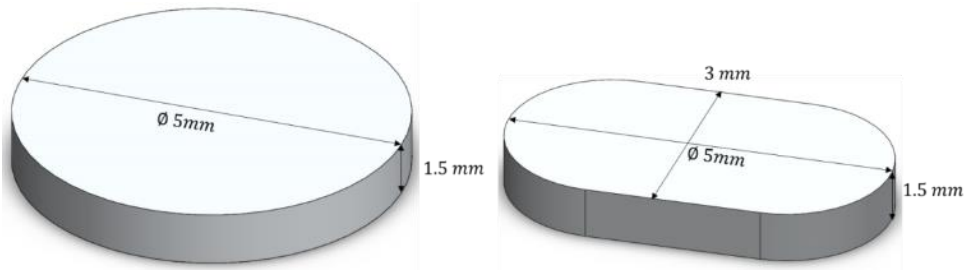

Figure 4.7 - DSC samples – disk shape (left) and customized shape.

To compare the specimens, base material samples were prepared on disk and elliptical shapes described above. All specimens from different weld zones and base material experienced the same preparation procedure. Before performing the test, the specimens were cleaned with ethanol and air-dried afterwards. As reference specimens, high purity aluminum of identical shape and weight was used.

5 RESULTS AND DISCUSSION

5.1 Selection of process parameters for SSuBT-FSW and SRBT-FSW

As described by Mishra and Ma [9], the main friction stir welding parameters are welding (v) and rotational speed (ω). The nominal operating parameters depend on the material to be welded, the welding machine and the specific criterion adopted for the evaluation of weld quality [51]. As these parameters determine the energy input, as demonstrated by Wu et al. [44], the first step in order to start this study was to establish the welding parameters operational window to obtain an acceptable microstructural and dimensional quality in the welded joint.

During the first trial, the rotation rate was too high, and due to the features on the probe, it is assumed that the probe presented a milling behavior. As result, the probe was cutting the material out of the plate instead of plasticizing it (Figure 5.1 (d)). To avoid a ‘milling’ action of the probe and to reduce energy input by 48%, ω was reduced to 2/3 and v was increased by around 30%. The result was still a non-consolidation of the weld due to an extensive heating leading to a possible local melting of the material, but the improvement was visible (Figure 5.1 (c)). Even when keeping the rotation rate constant and increasing the traverse speed by 80% (Figure 5.1 (b)) and 200% (Figure 5.1 (a)), related to the initial value (178mm/min), was still possible to observe lack of consolidation and surface defects. Further trials were performed to collect data and parameter windows of the two variants were set for both alloys.

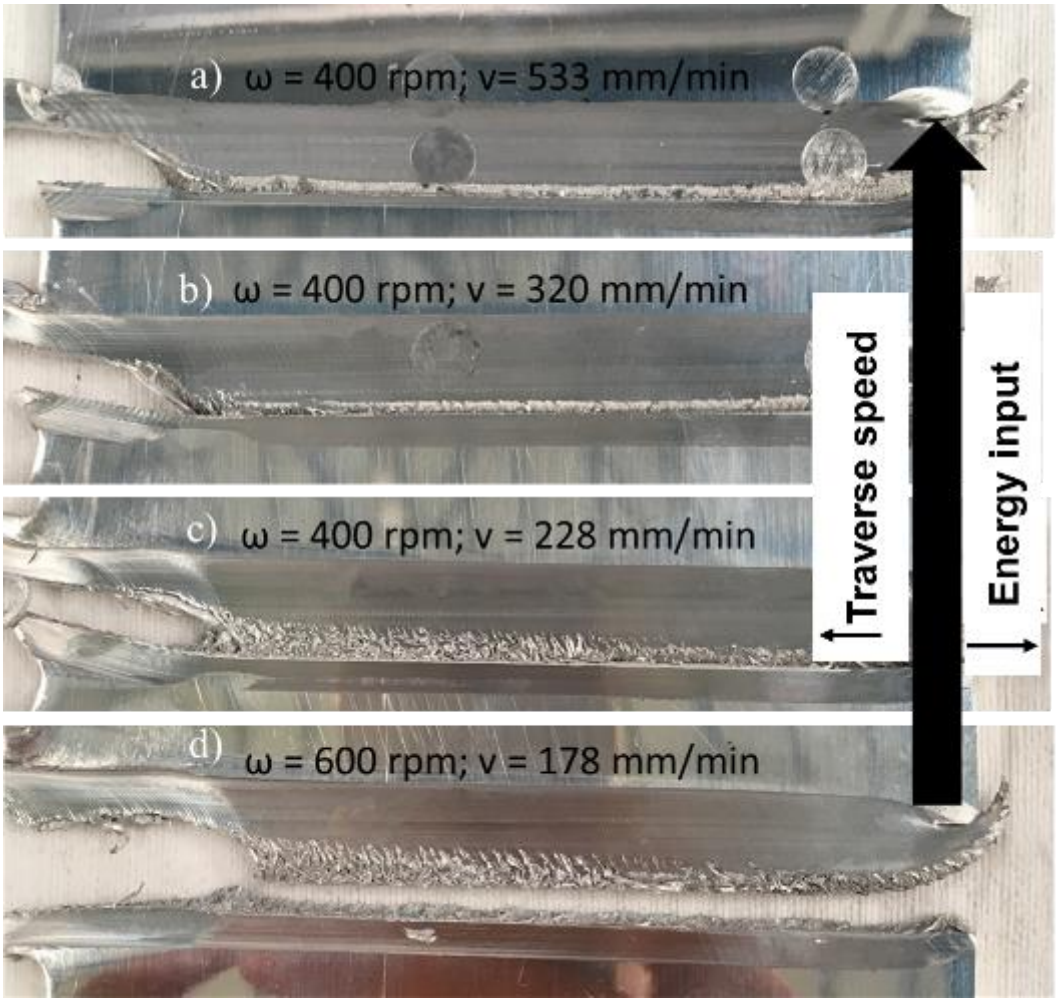

Figure 5.1 - View from the top of a SSuBT-FSW bead-on-plate (BoP) configuration varying rotation rate and traverse speed. Process parameters were (a) 400rpm – 533mm/min, (b) 400rpm – 320mm/min, (c) 400rpm – 288mm/min and (d) 600rpm – 178mm/min. Traverse speed increased from (d) to (a), in conjunction with a consequent reduction of energy input.

High and low energy input parameters were selected based on the operational parameters window, in order to maximize the difference between the two energy inputs while producing high quality welds. As presented on Table 4.3 and Table 4.4, SSuBT-FSW variant presented a more restricted processing window, considering the alloys under study and tool available. At welding speeds as high as the applied in SRBT-FSW, the energy input generated by SSuBT-FSW process was not enough to plasticize the material causing excessive loads on the

probe. Consequently, the forces imposed for rotation and translation of the tool triggered the breakage of the probe. Then, there was no possibility of replicating the welding parameters applied in SRBT-FSW variant.

After the best working parameters were established for each process variant and alloy, as presented on Table 4.3 and Table 4.4, visual inspection was performed to verify similarities and differences between the samples. The main difference found was an ironing effect on the upper surface in SSuBT-FSW welds. According to Goebel et al. [31], the stationary shoulder acts as a moving anvil plate and compresses the material, which has been previously plasticized by the probe. As a result, the characteristics semicircular marks, often reported as onion ring marks [9–11,14,31,41,52,53], are flattened to a better surface finish. This effect can be seen in Figure 5.2.

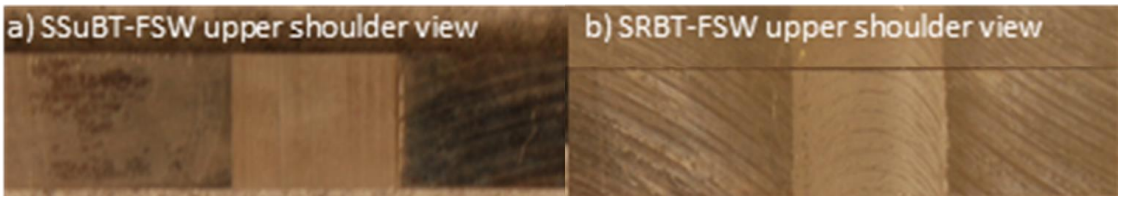

Figure 5.2 – Top view of upper shoulder side of AA2060 under (a) SSuBT-FSW and (b) SRBT-FSW.

Finally, SSuBT-FSW process showed to be more stable than SRBT-FSW in relation to the process forces after the warmup step. This may be related to the lower temperature reached on the stationary shoulder side. It led to a less plasticized material that offered a higher resistance to the tool, consequently stabilizing the probe [31].

5.2 Microstructural characterization of AA2060 and AA2196 welded by SSuBT-FSW and by SRBT-FSW

Welds produced using the different process parameter combination were subjected to hardness analysis. Hardness lines were recorded in order to reveal the local hardness distribution caused by thermal cycle. All the mechanical tests

were performed after a minimum of 5 weeks from the welding procedure. This period was determined by experimental tests made to ensure natural aging processes have become stable for both alloys.

5.2.1 Microstructural characterization of AA2060 welded by SSuBT-FSW and by SRBT-FSW

All welds were metallographically inspected for discontinuities, such as lack of consolidation, voids, and superficial discontinuities, due to non-optimal parameters causing insufficient material flow [31].

Major discontinuity found in SRBT-FSW samples during this work was a non-consolidation line located close to the SZ center on the RS. Regarding SSuBT-FSW, the main problems were caused by volumetric flaws in the surface in the advancing side, as presented in Figure 5.3. The non-consolidation line is often associated with inadequate welding parameters as explained in chapter 5.1

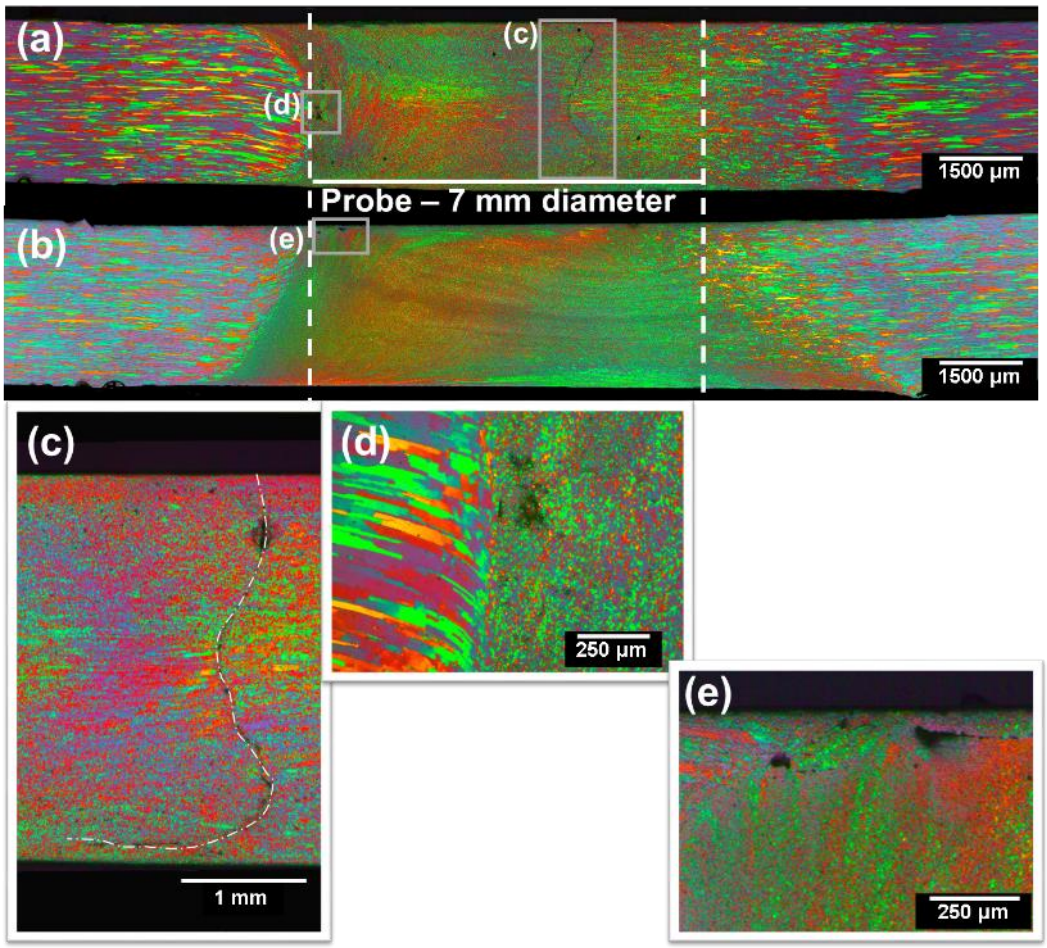

Figure 5.3 - Main discontinuities locations in AA2060 samples welded by (a) SRBT-FSW and (b) SSuBT-FSW high energy parameter. Image (c) highlights a non-consolidation oxide line that was present on all AA2060 SRBT-FSW-high parameter welds joined in butt joint configuration. Image (d) shows oxide marks inside SZ near TMAZ/SZ border on the AS close to the middle thickness of the sample, a critical location of volumetric flaws due to insufficient material flow in SRBT-FSW welds. Image (e) presents voids found on the upper surface of SZ near TMAZ/SZ border on AS of some AA2060 SSuBT-FSW welds.

In this study, SRBT-FSW flaw seems mostly related with the limitations of the clamping system. Identical welding parameters were repeated in bead-on-plate (BoP) configuration showing a flawless structure. In addition, the location of the defect line matches with the interface between the two plates joined in a butt

joint configuration, as visible in Figure 5.4. The non-consolidation line near the interface between the plates did not appeared in any of the SSuBT-FSW samples, using the same clamping system. This phenomenon occurs due to the diffusion process induced by the pressure of the stationary shoulder on the trailing side of the probe that supports the consolidation of the weld. On the surface of welded material this phenomena is known as “hot ironing” effect [41].

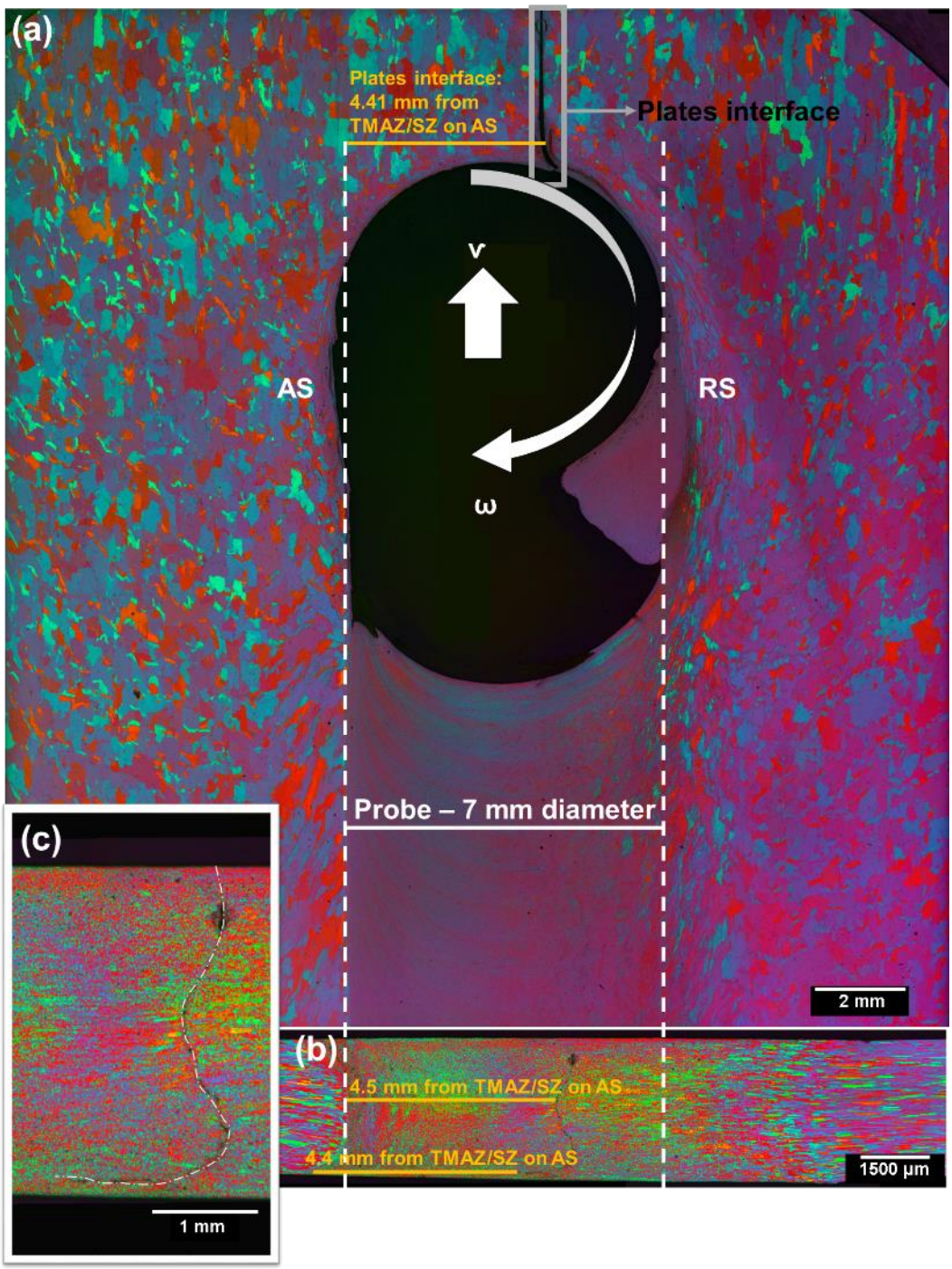

Figure 5.4 – Image (a) is a top view macrograph, perpendicular to welding direction, of a stop action with a broken probe, highlighting the interface between two AA2060-T8 plates. Figure (b) is a front view in the welding direction of the weld displaying different measurements positions that indicates the oxide line matches with the plates interface. Image (c) highlights a non-consolidation oxide

line that was present on all AA2060 SRBT-FSW – HEW welds joined in butt joint configuration.

5.2.1.1 Microstructural characterization of AA2060-T8 welded by SSuBT-FSW

Investigating the thermal cycle during BT-FSW is essential to understanding the microstructural and mechanical behavior of the welds since several metallurgical phenomena, such as recrystallization, grain growth, precipitation, coalescing and dissolution of precipitates are thermally affected.

The four measurements points, i.e. thermocouple position, were chosen based in the microstructures and hardness test found during this research. As the probe diameter of the tool of this study is 7 mm, 3.5 mm (point 4) is the nearest point of the SZ where we could place a thermocouple without it being destroyed by the tool during the welding procedure. Measurement point 3, located approximately 6 mm from the welding center, is the average distance where the minimum hardness of both alloys and welding variants was commonly found. Measurement points 2 and 1, at approximately 9 mm and 20 mm from weld center, respectively, where chosen to study the extent of the HAZ, and the development of the temperature over time in all different zones.

A typical temperature distribution is shown in Figure 5.5 (a). Previous study made by Goebel [31] showed that no difference in temperature in the AS and RS could be measured. As his previous work was performed at HZG on the same robot, tool, and similar conditions, only AS measurements were completed. The initial shape of the curve, from 20 to 46 seconds, indicates the heating rate of the metal, while the slope after the peak temperature reveals the cooling rate. As an example, measurement position 4 took approximately 15 seconds to increase the temperature from 50ºC to 450ºC but spent 107 seconds to cool down to 50 ºC. This means an average heating rate of around 26.7°C/sec and a cooling rate of 3.7°C/sec in this sample.

The measurement showed that temperature on the border of TMAZ/SZ reached around 450ºC. At 6 mm from the weld center, the temperature was up

to 400ºC, what means that the maximum temperature inside the TMAZ varied between 450-400ºC. In the HAZ, the range of maximum temperature was from 200 ºC to 400ºC. Figure 5.5 (b) presents the maximum temperature measured in each measurement point in both energy parameters. Two samples of each energy parameter (high and low energy input) were performed measuring temperature during welding. As no significant differences were observed, no further thermal analysis during welding were executed.

Additional information that can be found in this graph is the time that each point was exposed to a certain temperature. Figure 5.5 (c) presents the average time samples were exposed over 250ºC and 150ºC during welding. Exposition time at high temperature is important to understand metals answer to different environments and process. In addition, the border of SZ (measurement position 4) was approximately 20 seconds exposed to temperatures higher than 250ºC during welding.

The main influence of temperature on precipitation strengthened materials is the loss of strength caused by variations on microstructure. Gao et al. [13] studied the correlation of microstructure and mechanical properties in FSW of 2198-T8 alloy. In their work, it was found that T_1 phase (Al_2CuLi), the most important high strengthening precipitate for Al-Cu-Li alloys, fully dissolved into matrix in regions that reached up to 500°C, as the SZ. In zones that the temperature ranged from 150 to 450°C, most of T_1 dissolved and some partially coarsened. This work was consistent with other study showing that short time exposure (6 min) at 175 and 200 °C led to abundant nucleation and consequent significant coarsening of T_1 phase [13].

Table 5.1 present the energy input per unit length calculate using Equation 2.3 for AA2060 welded by SSuBT-FSW variants in both energy level parameters. Welding parameters used were presented in Table 4.3.

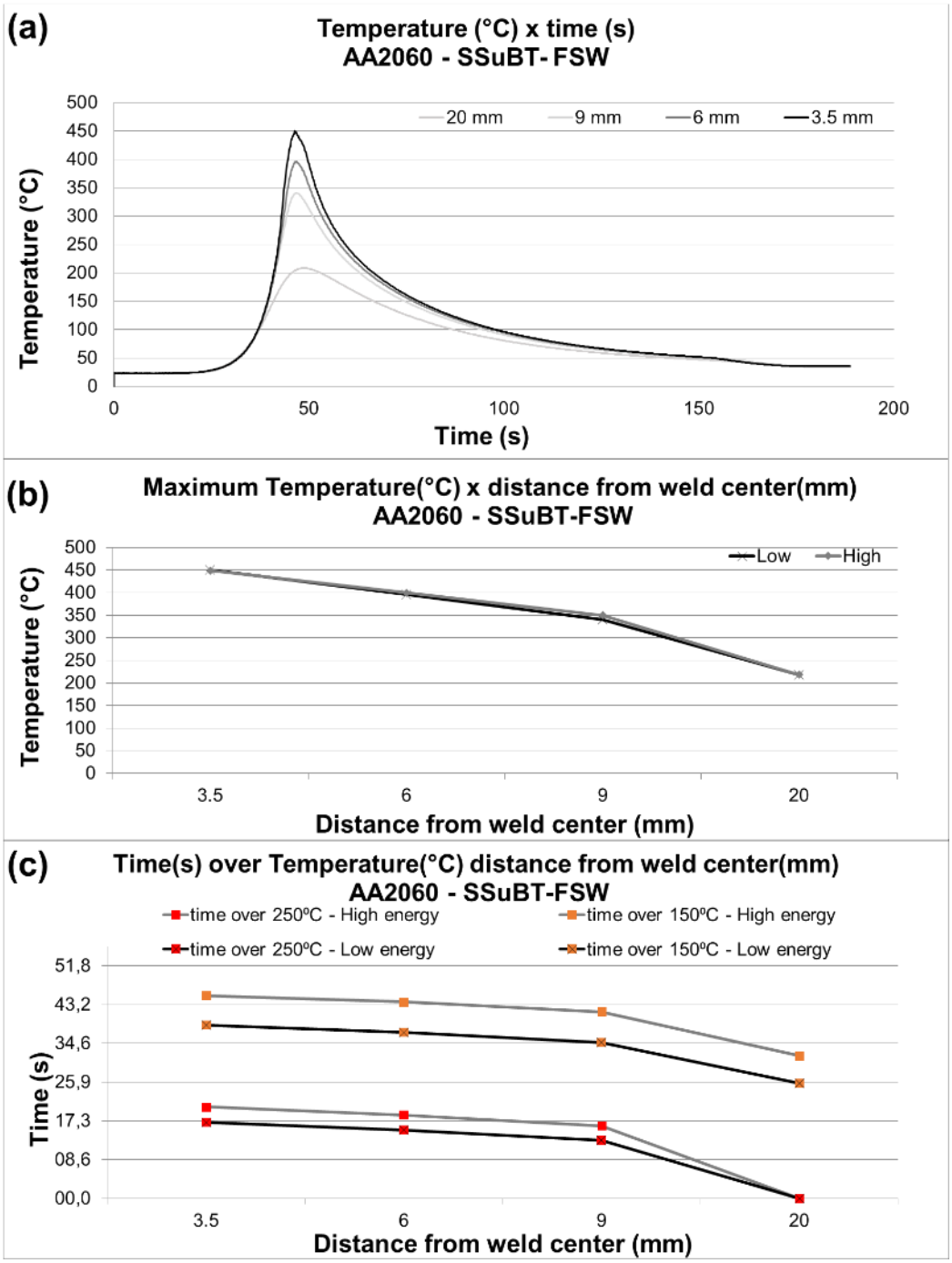

Figure 5.5 – (a) Temperature development over time (low energy sample), (b) maximum temperature measured and (c) exposition time over 250ºC and 150ºC during welding in the different measurement positions - 3.5mm (4), 6mm (3), 9mm (2) and 20mm (1) from the

weld center in the AS, during welding of AA2060-T8 plates by SSuBT-FSW.

Table 5.1 - Heat input per unit length, AA2060 per energy level parameter in SSuBT-FSW, calculated using Equation 2.3.

SSuBT-FSW	AA2060
High Energy	393 KJ/m
Low Energy	335 KJ/m

Optical microscopic analysis did not indicate general discrepancies between the samples, except the size of TMAZ that seemed to be varying, mainly in the RS. Zone size was estimated by analyzing the shape and size of the grains, combined with hardness profile results at samples middle thickness. Figure 5.6 shows the average zone size per energy input level.

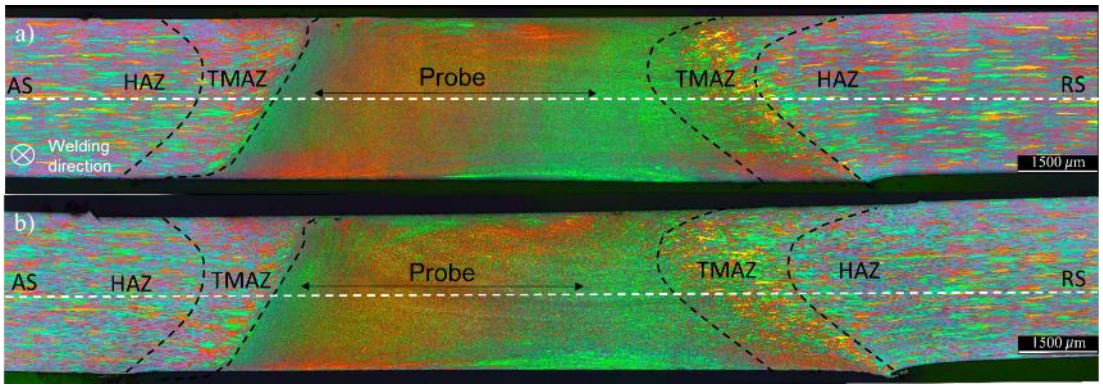

Figure 5.6 - AA2060 macrographs of SSuBT-FSW (a) high and (b) low energy input parameter, respectively.

The measurements showed that the energy level did not have a significant influence on the SZ size and shape but influenced the size of TMAZ. The size of SZ in the high energy level (HEW) was in average similar with the low energy level (LEW), while the TMAZ-AS was slightly bigger and TMAZ-RS was marginally smaller. Evaluating the welding parameters of both energy levels,

rotation rate was kept identical (150 RPM), gap force was less than 4% higher on HEW (5700 N) and the main difference was traverse speed. Then, increasing traverse speed from 125mm/min (HEW) to 150mm/min (LEW), led to minimum change on TMAZ size and no influence on SZ size.

Revisiting the process, decreasing the transverse speed, i.e. welding speed, means that material stays longer under the influence of the tool, so the softening gets bigger due to the exposition at longer time to high temperatures. As gap force and rotation rate did not significant shift, the result indicates that higher energy input was enough to extend the area of plasticized material, but not to provoke recrystallization in a higher extent.

Figure 5.7 displays the areas where grain size measurements were performed using Intercept Count Method of ASTM E-112. Images were taken with 1000x magnification. As was not possible to replicate the exact analysis position in every sample, an area was established. In the advancing side, it was easier to correct identify the begging of SZ, since the TMAZ/SZ border is sharp. However, as the same do not occurs in the RS, SZ-RS was defined slightly before the grain size shape and size turns to highly vary. Grain size measurements inside the SZ showed that HEW parameter tend to originated slightly bigger grains inside the SZ, but the measured differences were smaller than 1 μm being within the standard deviation. The average grain size was 7 μm (± 2 μm).

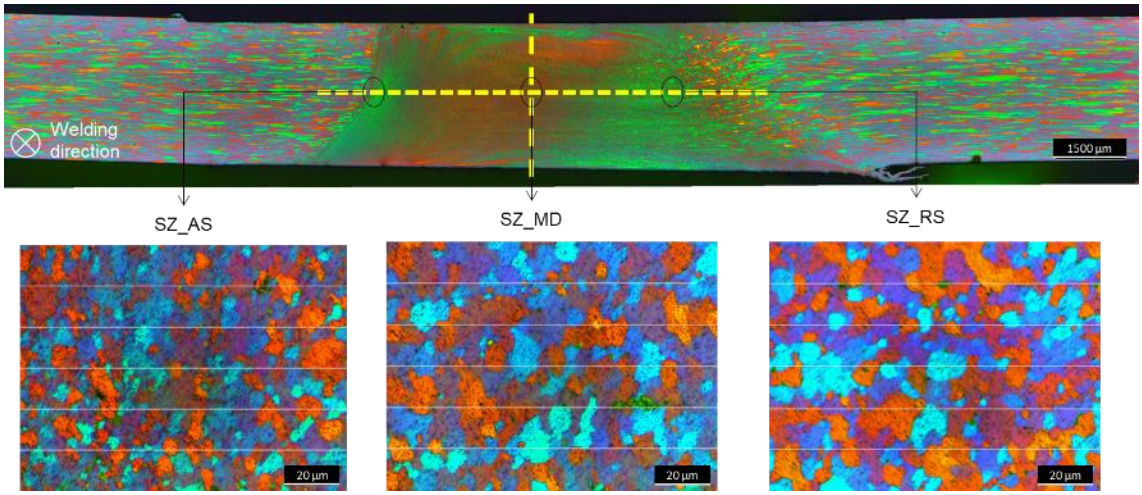

Figure 5.7 - Indication of location of grain size analysis through middle thickness line of AA2060 samples welded by SSuBT-FSW.

The energy input per length on the samples of HEW parameters were around 17% bigger than the LEW, as showed on Table 5.1. Analyzing the graph present in Figure 5.8 is possible to verify that samples that were under a process that involved a higher energy input had, in average, presented low hardness value, excluding inside the SZ. This effect was bigger on the AS of the welds.

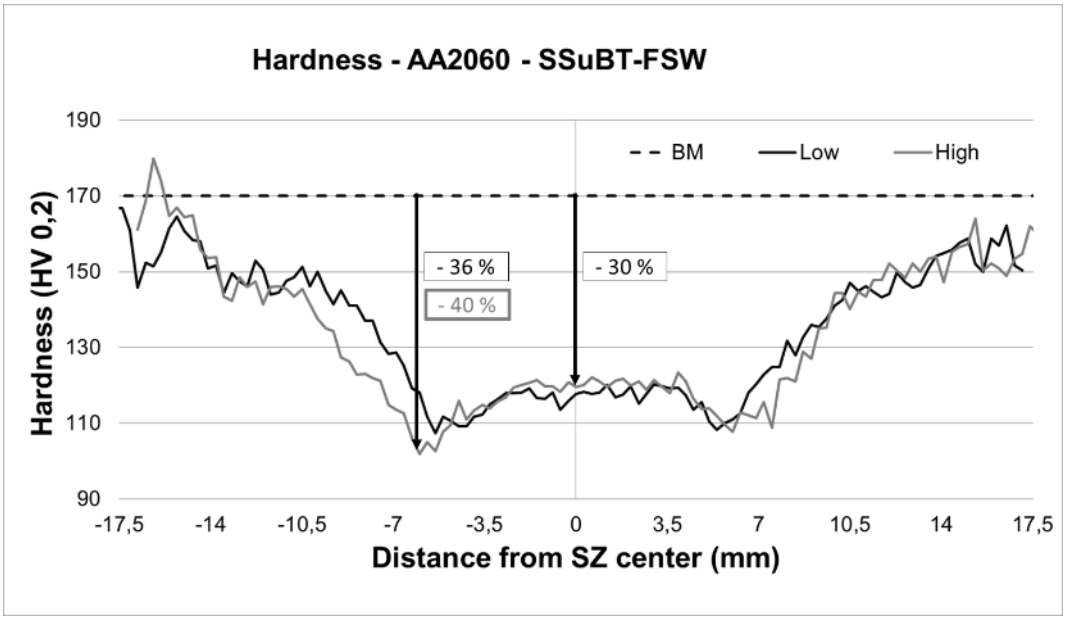

Figure 5.8 - Influence of the energy input level on the hardness test (HV 0.2) of AA2060 samples welded by SSuBT-FSW.

Evaluating Figure 5.8 a few observations can be taken into attention. First, related with the shape of both curves. The local mechanical answer of the samples seems to indicate a variation on zone sizes, mainly in TMAZ. This is in accordance with the optical analysis findings in Figure 5.6. Second, HEW samples achieved lower hardness on the HAZ, achieving the minimal performance on AS. The increase of exposition time at high temperatures may have influenced this result. Differential Scanning Calorimetry (DSC) analysis were performed to investigate the effect of temperature and time on the microstructural evolution of the welded samples.

Differential Scanning Calorimetry (DSC) is an important technique that measures temperatures and heat flux associated with material transitions as a function of temperature and time. These measurements use qualitative and quantitative information on chemical and physical changes that involve endothermic (heat absorption), exothermic (heat release) or heat capacity changes [67,68]. Both materials (AA2060 and AA2196) and both process (SRBT-FSW and SSuBT-FSW) were tested under DSC analysis. As microstructural and hardness analysis did not show significant variations between LEW and HEW

samples, only low energy input parameters welds were taken into consideration, and then no comparison between the energy level will be performed.

DSC graph of AA2060-T8 BM sample is presented in Figure 5.9. At around 110 ºC the first endothermic peak is found (A). At around 200ºC (B) and 450ºC (E) two more endothermic peaks appear. Exothermic reactions occur around 250ºC (C) and 350ºC (D). Endothermic and exothermic reactions are associated with phase dissolution and formation, respectively [67–69].

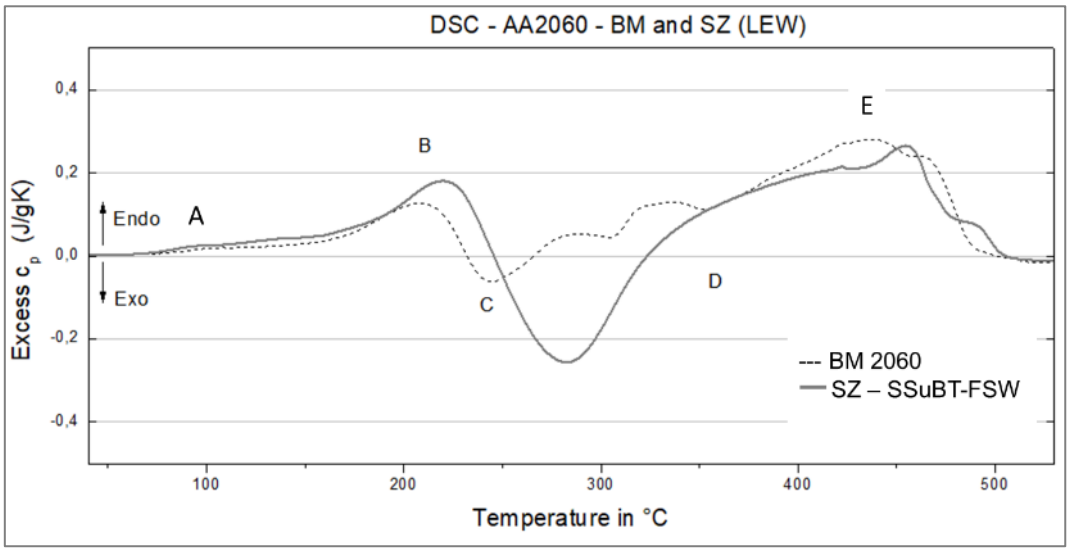

Figure 5.9 - Differential Scanning Calorimetry graph of SZ samples of AA2060 welded by SSuBT-FSW – low energy parameter.

Decreus et al [20] studied the precipitation sequence of AA2196 (low Cu/Li ratio) and AA2198 (high Cu/Li ratio) in T351 state during aging at 155°C during different periods. It was determined that peak A+B, described as a unique peak at his work, were associated with the dissolution of Cu-rich clusters for high Cu alloy (AA2198) and partial dissolution of δ' (Al_3Li) precipitates in Li-rich alloy (AA2196) in T351 state. Peak C was related with precipitation of phases such as T_1 (Al_2CuLi).

At this work, peak A (130 ◦C) was associated with the dissolution of Cu-rich GP zones and fine δ' (Al_3Li) phases. Peak B (210 ◦C) was related with δ' (Al_3Li) dissolution. Peak C, at approximately 250 ◦C, indicates the formation of T_1 (Al_2CuLi). Then, from the end of peak C, around 300°C, to the beginning of peak E, there is an area, peak D, consisting of several overlapping peaks presumed to

be related with formation of equilibrium phases, such as T_2 (Al_6Li_3Cu) and Tb ($Al_{7.5}LiCu_4$), [47,70]. Schneider associated peak D with formation of θ and θ' precipitates [35]. Finally, peak E was linked with the dissolution of prior formed T_1 precipitates, secondary phases and equilibrium phases, such as T_2, Tb, θ and θ'.

As reported in Figure 5.5, the temperature in the weld center achieved up to 450°C in the SSuBT-FSW. The DSC result presented in Figure 5.9 showed that at this temperature most of the precipitates inside the SZ were dissolved. The exposition time over high temperatures was distinct between the energy level parameters, as reported in Figure 5.5.Then the small difference between the energy input was probably enough to extent the dissolution of Cu-rich clusters and aging of δ' precipitates. Consequently, in the SZ the performance was similar probably because on the HEW samples occurred a higher range of dissolution of precipitates that later promoted a higher natural aging recovery. However, in the other zones the energy given by both processes were not able to dissolve the precipitates, then when more energy was given, bigger was the precipitate growth and higher were the mechanical properties loss. At distances higher than10.5mm from the weld center, no effect of the energy input was displayed.

5.2.1.2 Microstructural characterization of AA2060 welded by SRBT-FSW

Temperature development over time of AA2060 samples welded by SRBT-FSW showed that HEW achieved higher temperature for all measurements points, as showed by Figure 5.10 (a). However, more tests should have been performed to a more precise discussion. Moreover, Figure 5.10(b) indicates the exposition time over 150°C and 250°C for each energy parameter. The shape of the curves indicates that the heating and cooling rate are higher for HEW parameter, as displayed in Figure 5.10(c).

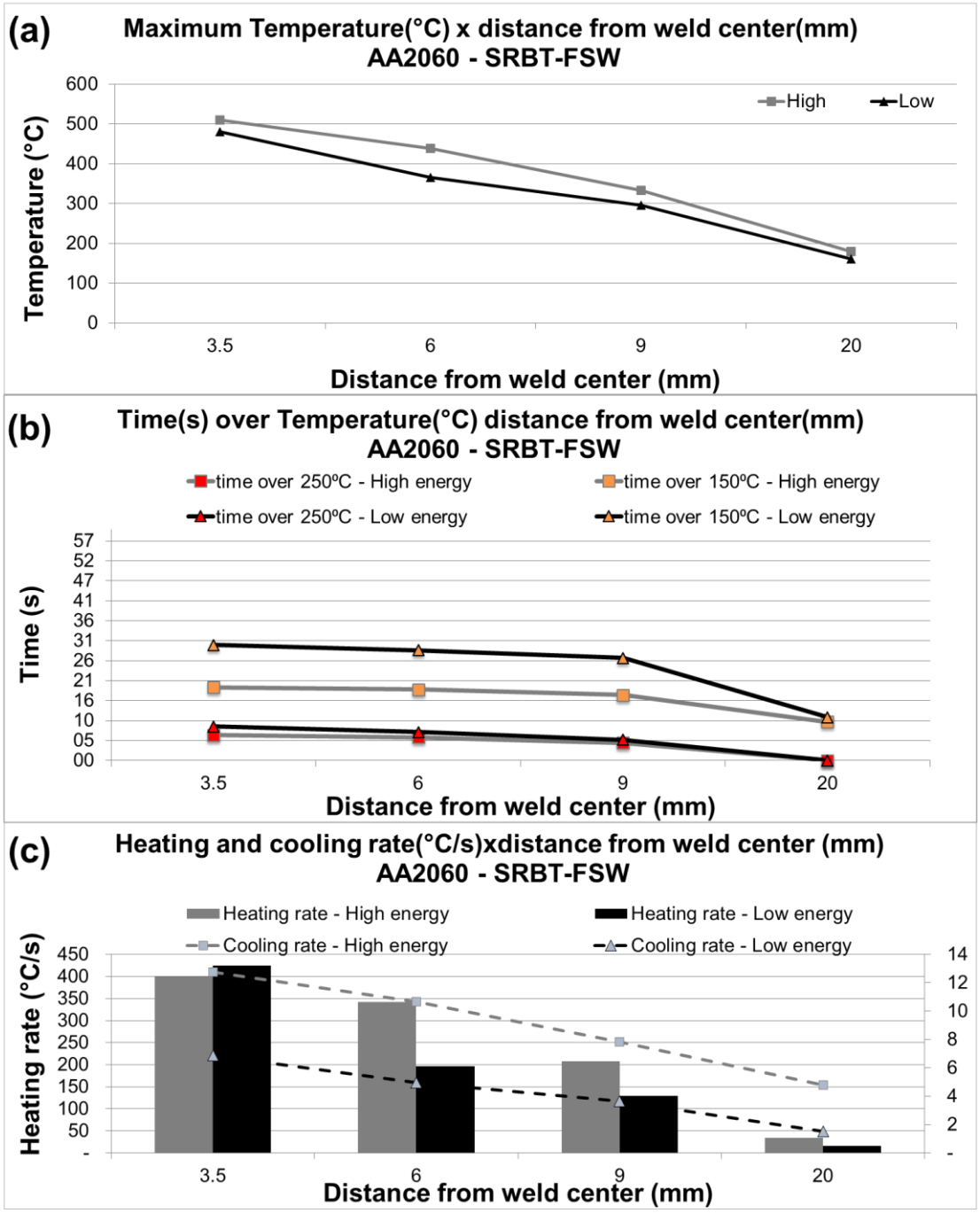

Figure 5.10 - (a) Maximum temperature measured, (b) exposition time over 250ºC and 150ºC and (c) heating and cooling rate during welding in the different measurement positions - 3.5mm (4), 6mm (3), 9mm (2) and

20mm (1) from the weld center in the AS, during welding of AA2060-T8 plates by SRBT-FSW.

Vickers hardness test performed in AA2060 samples welded by SRBT-FSW in LEW and HEW showed that in general HEW samples presented a hardness inside the SZ in average similar with LEW samples. In addition, Figure 5.10 (c) disclosed that HEW samples presented a cooling rate during SRBT-FSW welding almost twice as the cooling rate of LEW samples. This means HEW were a shorter time exposed to temperature over 250°C, but similar exposition time to temperatures around 150°C. That was enough to promote Cu-rich cluster and δ' precipitates dissolution, besides, precipitate aging in TMAZ and HAZ. Then, is believed that even with an almost 27% higher heat input per length, as showed by Table 5.2, the traverse speed was the essential parameter to influence the final microstructure of the weld since the velocity the tool move through the weld was essential to cool down and reduce the thermal effect of the process inside SZ. However, the higher energy input induced to a more degraded HAZ. Welding parameters were presented in Table 4.4 and DSC test is available in Figure 5.12.

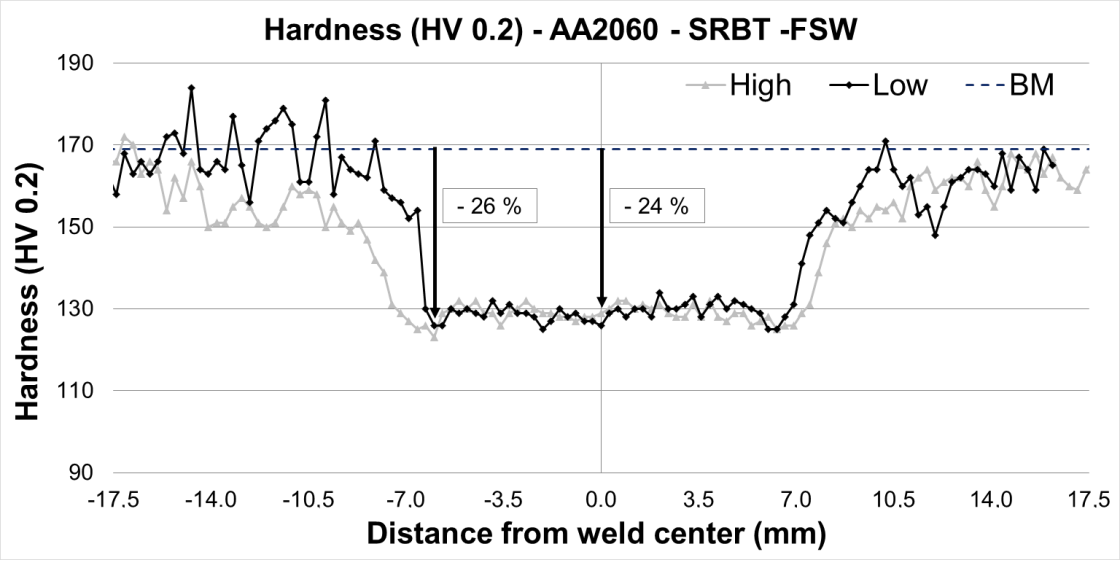

Figure 5.11 – Vickers hardness test (HV 0.2) of AA2060 welded by SRBT-FSW in high (HEW) and low (LEW) energy welding parameters.

Table 5.2 - Heat input per unit length, AA2060 per energy level parameter in SRBT-FSW, calculated using Equation 2.3.

SRBT-FSW	AA2060
High Energy	222 KJ/m
Low Energy	175 KJ/m

Finally, evaluating the microstructural evolution of AA2060-T8 under both welding procedures in Figure 5.12, it can be seen that in SZ all peaks were shift to the right in relation to the BM. It means that the transformations, associated with dissolution and formation of precipitates, were occurring at higher temperatures. Regarding the endothermic peaks, mainly peak B, this behavior can be an indication of increase of precipitate size, that increases the stability of the precipitates by lowering the Gibbs–Thomson effect [20,46].

Analyzing peak C, associated with T_1 formation, besides the shift to the right, an increased peak area is found on both BT variants SZ samples. As SZ is characterized by a recrystallized, deformation-free zone, it is likely that the original amount of T_1 present in BM dissolved during welding [20,33,35,42,46,70]. Then, a higher amount of Cu and Li were available on the alloy allowing a higher extent of T_1 precipitation during DSC heat cycle, consequently resulting in a pronounced peak on the DSC graph. Peak D was not observed on the SZ of welded samples. This can be related with formation of this equilibrium phases during welding, what could led to the absence of signal during DSC analysis, or even a overlap of peak D with the intense peak C [47].

The main difference found when comparing SRBT-FSW and SSuBT-FSW is that the first presented a much higher intense formation peak C than the SSuBT-FSW variant. When the peak temperature and the exposure time increases, the degree of supersaturation remaining increases, the post welding natural aging response is greater, and the hardness recovery in center SZ is more obvious (W-shaped profile) [42]. Then, as SRBT-FSW was exposed at

temperatures above 150ºC by shorter period than SSuBT-FSW, SRBT-FSW did not presented as much natural aging as SSuBT-FSW inside the SZ, which led to a higher content of material available in the matrix during DSC analysis that led to a more intense peak formation of T_1 precipitate.

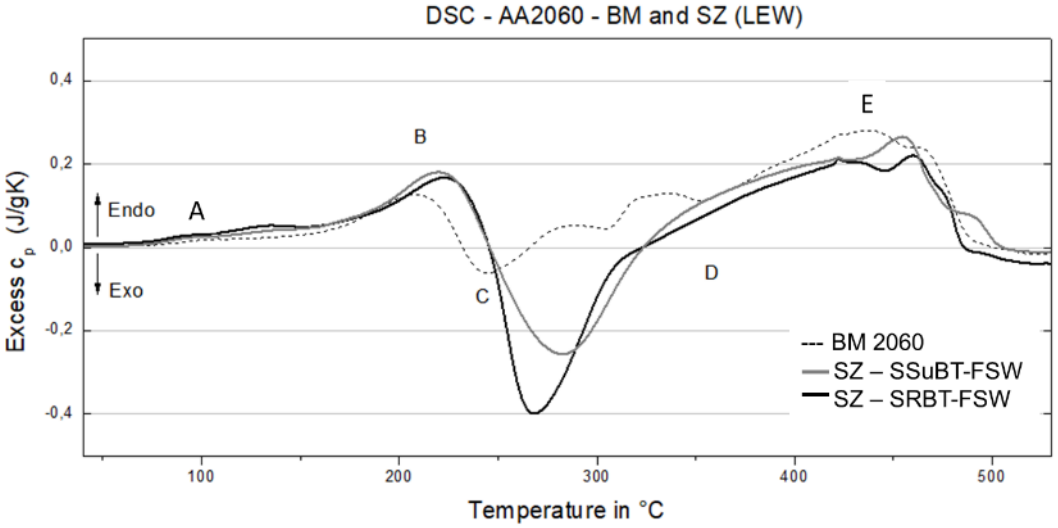

Figure 5.12 – Differential Scanning Calorimetry graph of SZ samples of AA2060 welded by SSuBT-FSW and SRBT-FSW low energy parameters.

Moreover, the final microstructure and grain size was affect by the process variants. Besides the remarkable difference of SZ shape in each variant, grain size growth inside the SZ was also affected. For SRBT-FSW variant, the grain growth occurs from the AS (5.9 ± 0.2 µm) to the RS (9.8 ± 0.8 µm), and from the edges (5.6 ± 0.3 µm) to the center of the weld (8.5 ± 0.5 µm). This measurement was performed using the Intercept Count Method of ASTM E-112. This is in correlation to the heat input. As both shoulders are rotating, is believed that a ‘heat sink’ is formed in the middle layer of the SZ resulting in grain growth [71]. As the rotating shoulder is responsible for the biggest component of providing heating [66], in SSuBT-FSW, the bottom of the weld presents higher grain growth. Figure 5.13 shows the grain growth direction inside the SZ of the welds.

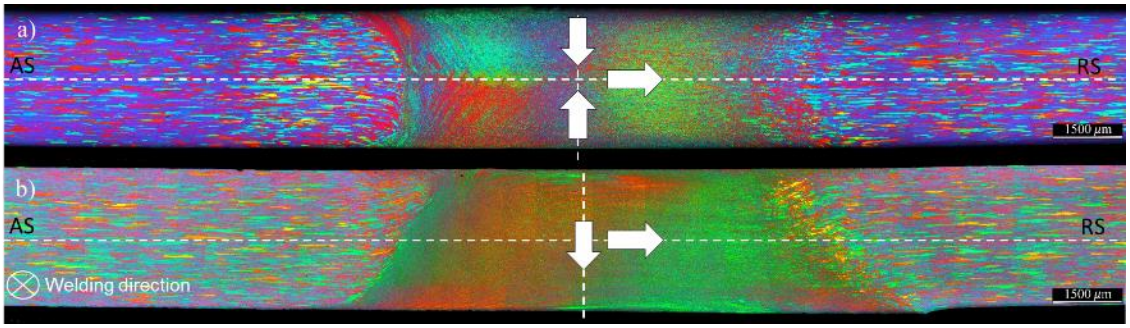

Figure 5.13- Schematic grain growth direction inside the SZ for (a) SRBT-FSW and (b) SSuBT-FSW variants.

5.2.2 Microstructural characterization of AA2196 welded by SSuBT-FSW and by SRBT-FSW

Thermal and microstructural analysis performed in AA2060 were repeated in AA2196 welded by SSuBT-FSW and SRBT-FSW to understand how this alloy was affect by the welding procedures. Figure 5.14 presents a metallographic inspection validating the measurement point 4, on the interface of TMAZ/SZ on the advancing side of an AA2196 SRBT-FSW LEW sample.

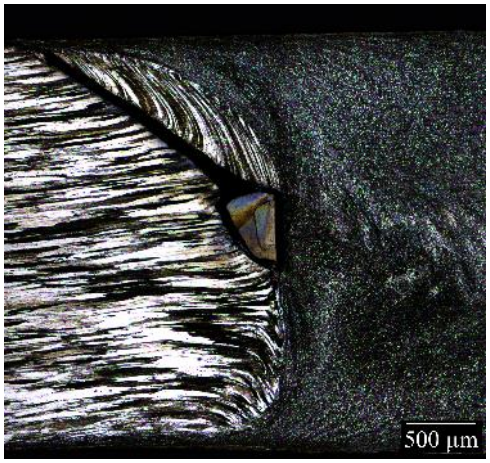

Figure 5.14 - Metallographic inspection showing the exact final position of thermocouple placed in measurement point 4 after welding of a AA2196 SRBT-FSW LEW sample.

5.2.2.1 Microstructural characterization of AA2196 welded by SSuBT-FSW

Temperature measurements performed during welding of AA2196-T8 plates by SSuBT-FSW showed that maximum temperature reached by both energy parameters were similar. HEW parameter was longer time exposed to high temperatures. Heating rate of LEW is higher than HEW, but cooling rate not significantly vary. The welding tool destroyed the thermocouple located in position 4 when passed by it on HEW sample, then just heating rate and maximum temperature were measured, but cooling rate and time of exposition was not possible to calculate. Figure 5.15 shows thermal measurements achieved during welding. Table 5.3 - Heat input per unit length, AA2196 per energy level parameter in SSuBT-FSW, calculated using Equation 2.3.Table 5.3 presents the heat input per unit length per energy level parameter of AA2196 welded by SSuBT-FSW.

Table 5.3 - Heat input per unit length, AA2196 per energy level parameter in SSuBT-FSW, calculated using Equation 2.3.

SSuBT-FSW	AA2196
High Energy	376 KJ/m
Low Energy	327 KJ/m

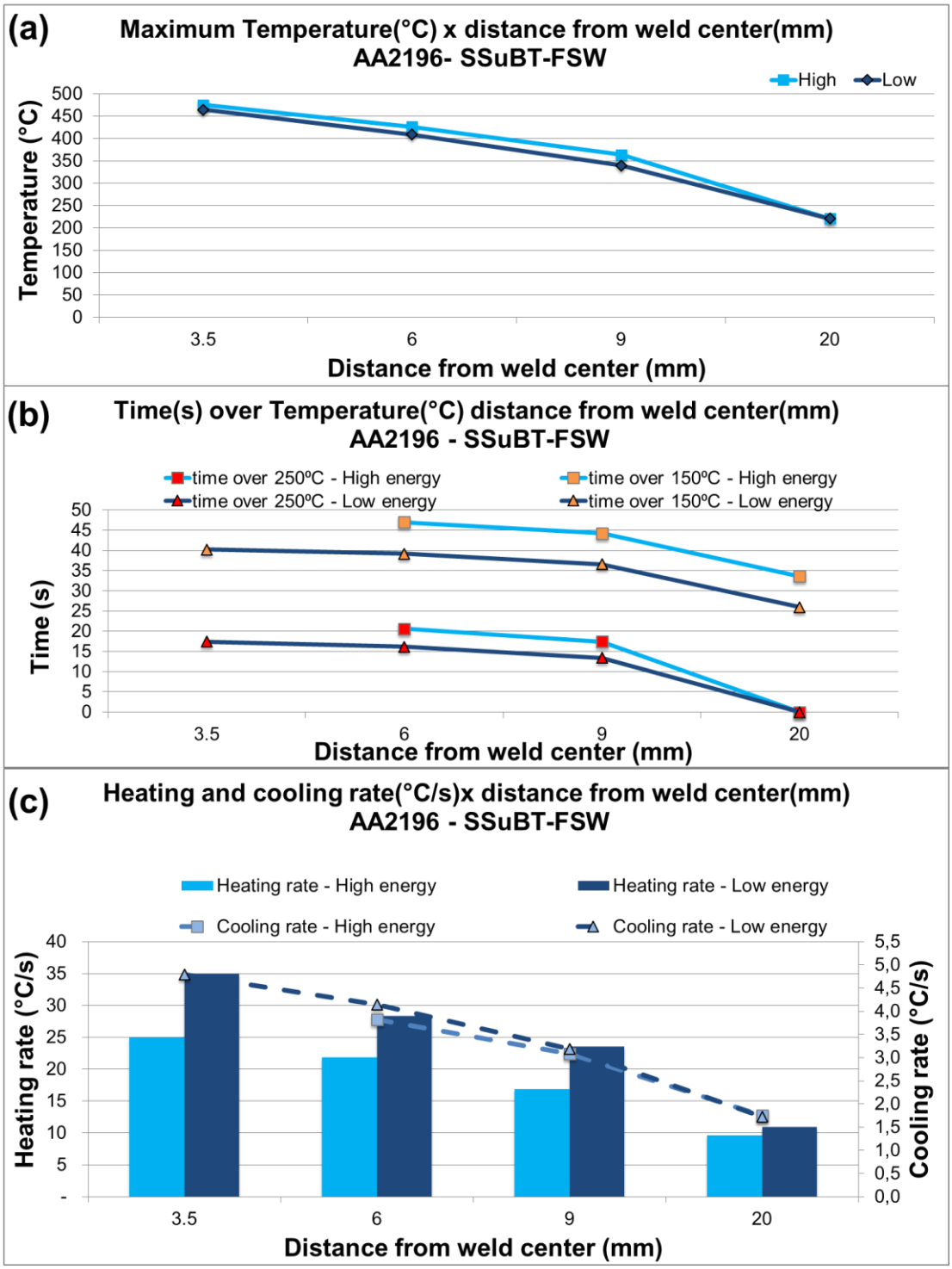

Figure 5.15 - (a) Maximum temperature measured, (b) exposition time over 250ºC and 150ºC and (c) heating and cooling rate during welding in the different measurement positions - 3.5mm (4), 6mm (3), 9mm (2) and

20mm (1) from the weld center in the AS, during welding of AA2196-T8 plates by SSuBT-FSW.

Vickers hardness test exposed that the variation in energy input parameter did not influenced in SZ and TMAZ performance, but seems to influence HAZ. HEW samples presented a lower hardness value for the points between the lowest hardness point, located between 5 to 5.5 mm from weld center (WC) on AS, to around 8mm from WC, what corresponds the area under the shoulder. As presented in Table 4.3, the difference between HEW and LEW is the traverse speed that is higher in LEW. Then, it means that HEW samples were at longer period under shoulder influence, what leads to the results presented in thermal and hardness test.

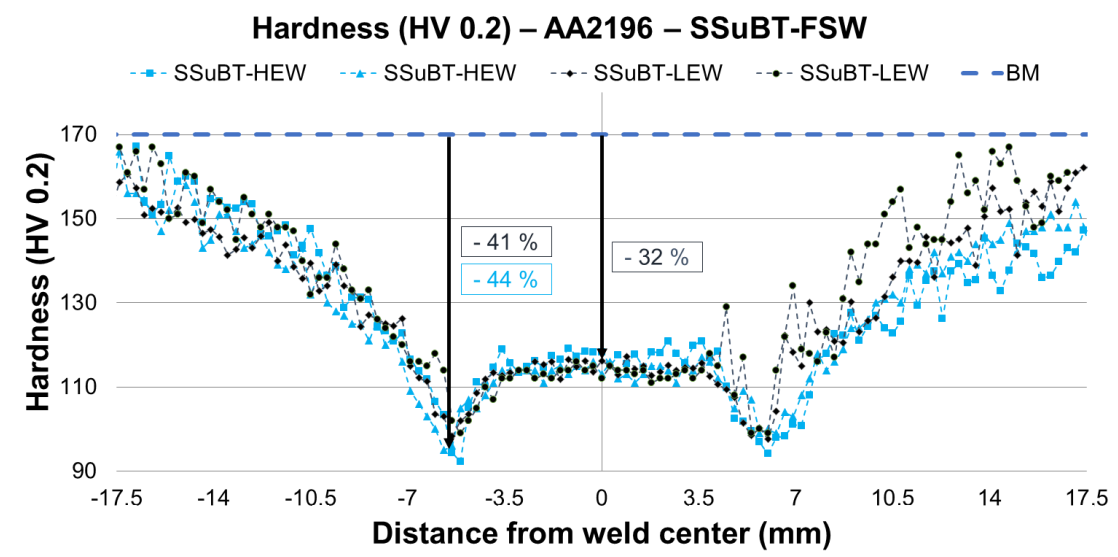

Figure 5.16 - Vickers hardness test (HV 0.2) of AA2196 welded by SSuBT-FSW in high (HEW) and low (LEW) energy welding parameters.

DSC analysis was completed to evaluate the behavior of the base material and welded samples. First, AA2196 welded by SSuBT-FSW LEW presented a more intense peak A than BM. This is linked to the bigger amount of natural aged δ' (Al_3Li) precipitates that are smaller in the welded samples than in the original AA2196-T8 plate. The same description can explain the more intense peak B in BM, as BM has artificial aged δ' (Al_3Li) precipitates. Second, peak C, related to T_1 formation, is observed at a higher temperature and intensity in welded

samples. As SZ is characterized by a recrystallized, deformation-free zone, it is likely that the original amount of T_1 present in BM dissolved during welding [20,33,35,42,46,70]. Then, a higher amount of Cu and Li were available on the alloy allowing a higher extent of T_1 precipitation during DSC heat cycle, consequently resulting in a pronounced peak on the DSC graph. Peak D was not observed on the SZ of welded samples. This can be related with formation of this equilibrium phases during welding, what could led to the absence of signal during DSC analysis, or even a overlap of peak D with the intense peak C [47]. DSC graph is displayed in Figure 5.17.

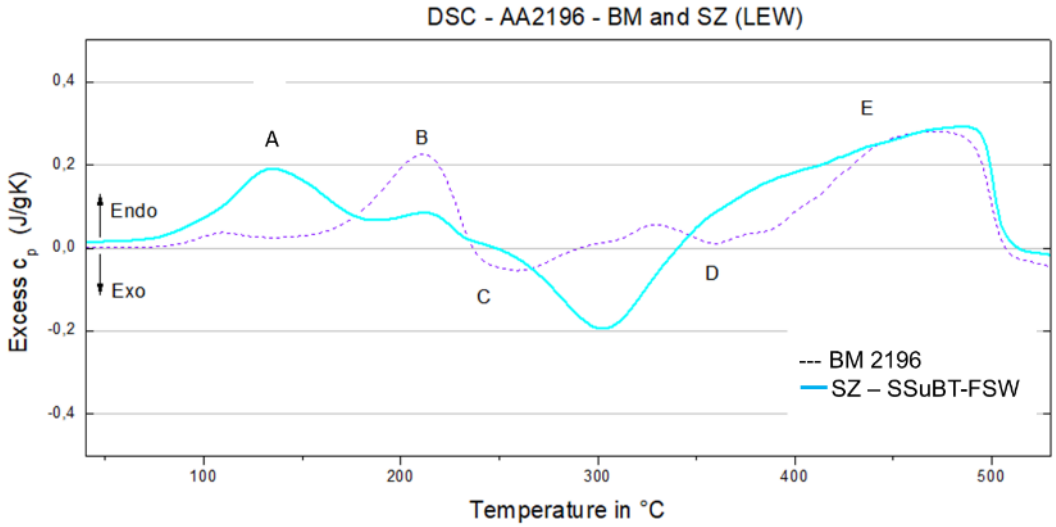

Figure 5.17 - Differential Scanning Calorimetry graph of BM and SZ samples of AA2196-T8 welded by SSuBT-FSW – low energy parameter.

5.2.2.2 Microstructural characterization of AA2196 welded by SRBT-FSW

Temperature development over time of AA2196 samples welded by SRBT-FSW showed that HEW achieved higher temperature for all measurements points, as showed by Figure 5.18 (a). However, more tests should have been performed to a more accurate discussion. Moreover, Figure 5.18 (b) indicates the exposition time over 150°C and 250°C for each energy parameter. HEW was exposed to higher temperature at longer time than LEW. In addition, while LEW samples did not achieve 150°C at 20mm from WC, HEW samples were exposed to over 150°C for around 30 seconds at the same position. Cooling rate was the same for both parameters in all measurements points, but heating

rate was expressively higher for LEW samples near WC, as displayed in Figure 5.18(c). Table 5.4 presents the heat input per unit length per energy level parameter of AA2196 welded by SRBT-FSW.

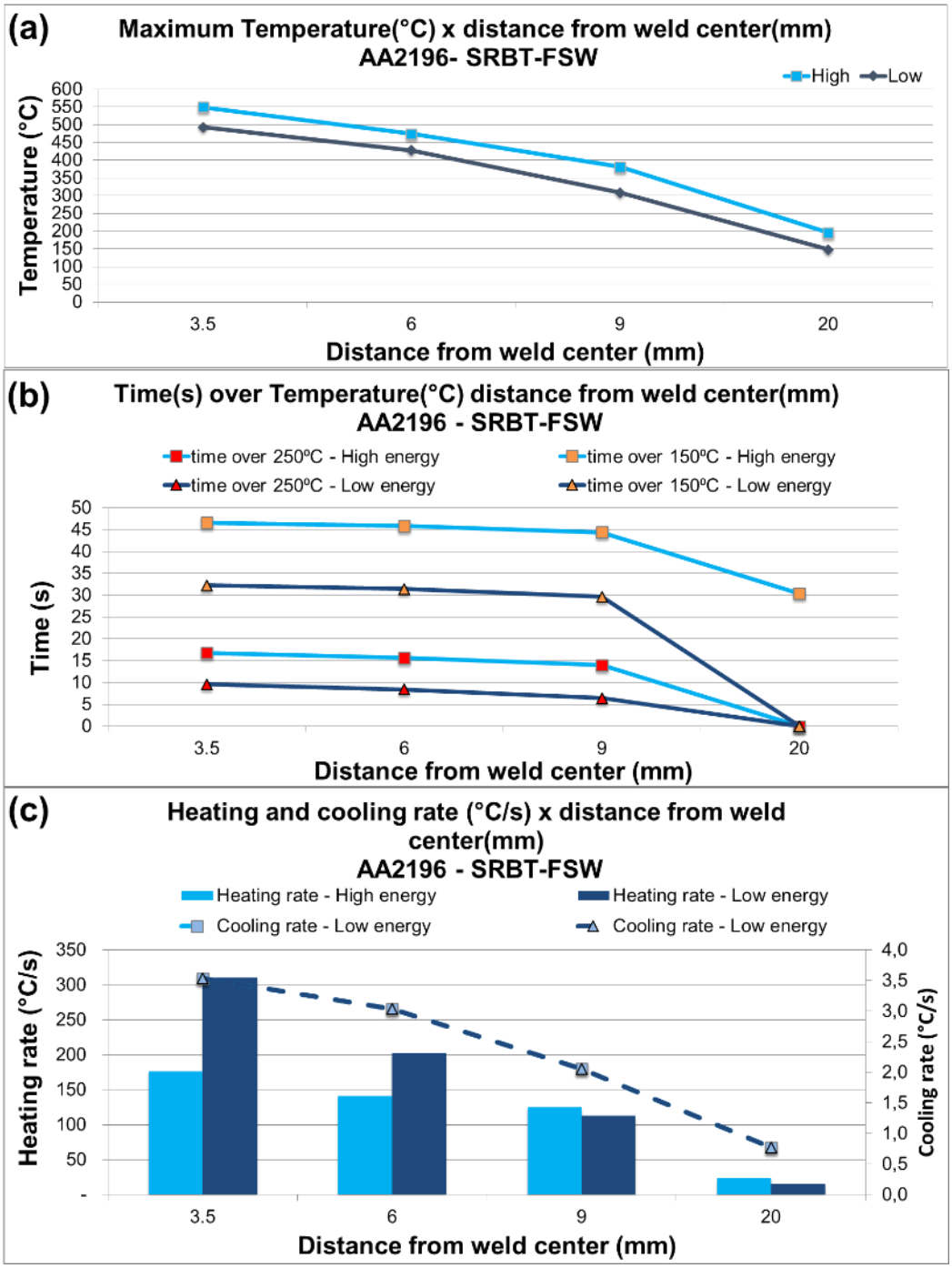

Figure 5.18 - (a) Maximum temperature measured, (b) exposition time over 250ºC and 150ºC and (c) heating and cooling rate during welding in the different measurement positions - 3.5mm (4), 6mm (3), 9mm (2) and

20mm (1) from the weld center in the AS, during welding of AA2196-T8 plates by SRBT-FSW.

Table 5.4 - Heat input per unit length, AA2196 per energy level parameter in SRBT-FSW, calculated using Equation 2.3.

SRBT-FSW	AA2196
High Energy	222 KJ/m
Low Energy	169 KJ/m

Besides thermal graphs, hardness profile implied that HEW stimulate a more degraded HAZ. This analysis is due the minimum hardness point that is more pronounced in HEW samples than in LEW. In addition, hardness values obtained in HEW returned to BM hardness baseline at longer distance from WC, which point toward a larger HAZ. Figure 5.19 displays hardness test results.

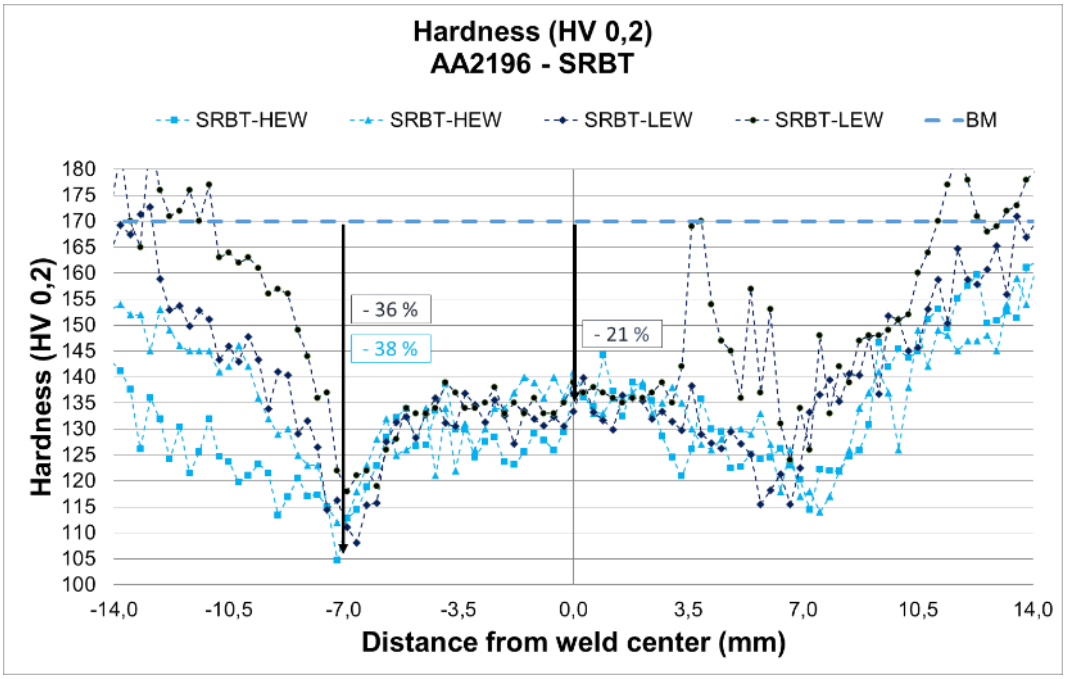

Figure 5.19 - Vickers hardness test (HV 0.2) of AA2196 welded by SRBT-FSW in high (HEW) and low (LEW) energy welding parameters.

Microstructural analysis is in agreement with hardness test, where in HEW samples TMAZ grains looked bigger than in LEW samples. In addition, in Figure 5.20 is possible to observe a higher influence of the shoulder on HEW, directed by a higher curvature of TMAZ/SZ border on AS, and leading to a higher extent of SZ and TMAZ near the shoulders.

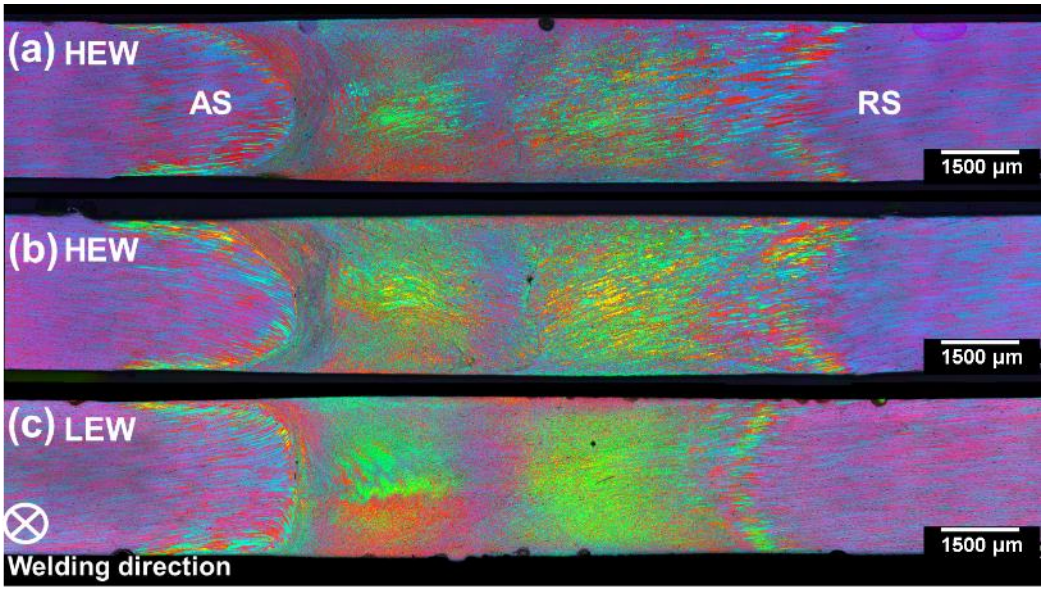

Figure 5.20 - AA2196 macrographs of SRBT-FSW (a-b) high and (c) low energy input parameter, respectively.

DSC analysis were performed only in LEW samples. Then, no evaluation comparing energy parameters could be completed. However, DSC analysis of AA2196-T8 plates welded by SSuBT-FSW and SRBT-FSW can be studied. Peak A drives to believe that SRBT-FSW led to a higher natural aging amount, since this peak is related with dissolution of fine δ' (Al_3Li) precipitates. Peak B, associated to the dissolution of δ' (Al_3Li) precipitates lost intensity in both welding procedures related with BM. However, the higher intensity of peak B of SRBT-FSW samples compared with SSuBT-FSW samples can indicate a higher content of this precipitate on the self-reacting welded sample. This is validated by peak C, since SRBT-FSW samples presented a much higher intense formation peak C than the SSuBT-FSW variant. This means SRBT-FSW welding of AA2196-T8 led to a higher content of material available in the matrix after welding, then during DSC analysis, it led to a more intense peak formation of T_1 precipitate. DSC graph of AA2196-T8 base material, SZ samples taken from plates welded by SRBT-FSW and SSuBT-FSW are presented in Figure 5.21.

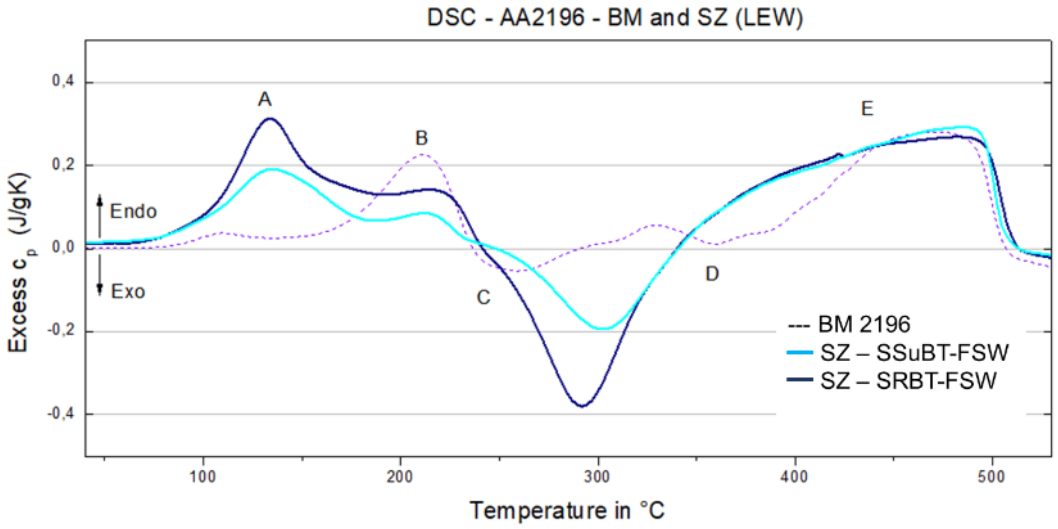

Figure 5.21 - Differential Scanning Calorimetry graph of SZ samples of AA2196 welded by SSuBT-FSW and SRBT-FSW low energy parameters.

5.2.3 Influence of Cu/Li ratio on the microstructure of AA2060 and AA2196 welded by SSuBT-FSW and by SRBT-FSW

As observed in items 5.2.1 and 5.2.2, different welding procedures (SSuBT-FSW and SRBT-FSW) caused dissimilar effect in each alloy and underwent unlike influence by each energy input parameters. To summarize the main parameters and thermal effects observed, Table 5.5 was designed. Evaluating the performance of both alloys under SSuBT-FSW LEW, it can be seen that no significant thermal differences were found. However, a general behavior happened under both procedures: at same main parameters, AA2196 achieved higher peak temperature and heating rate and smaller cooling rate. When comparing both alloys under SRBT-FSW LEW, AA2196 welded samples presented an average heating rate 62% higher and a cooling rate 39% smaller than AA2060 welds.

Heating and cooling rates can be an indication that AA2196 absorbs energy faster and dissipate energy slower than AA2060, what led to a higher peak temperature. In addition, data in Table 5.5 suggests that AA2196 samples plasticize easier than AA2060 samples. This statement is obtained analyzing power and heat input equations, as the only reason for the welding power and

heat input being smaller is a smaller torque required, as rotational and welding speed was kept identical.

Table 5.5 – Welding parameters and thermal measurements of AA2060 and AA2196 welded by SSuBT-FSW and SRBT-FSW in LEW.

	AA2060 SSuBT-FSW – LEW	AA2196 SSuBT-FSW – LEW	AA2060 SRBT-FSW – LEW	AA2196 SRBT-FSW – LEW
Rotation rate (RPM)	150	150	400	400
Welding speed (mm/min)	150	150	800	800
Power (kW)	0.84	0.82	2.33	2.24
Heat input per length (kJ/m)	335	327	175	168
Peak temperature (ºC)	450.1	464.9	480.3	492.7
Heating rate (ºC/s) – 6mm from WC	32.66	37.55	124.9	202.3
Cooling rate (ºC/s) – 6mm from WC	4.6	4.3	4.9	3.0

This behavior is probably related with the chemical composition of the material. As is no data available of the thermal properties of the alloys under study, the thermal properties of the pure metals will be taken into analysis. Table 4.1 refers to the chemical composition of both alloys. As it can be seen, AA2060 has 4.2%wt. of Cu and 0.9%wt of Li, while AA2196 has 2.9%wt. and 2.0%wt. of Cu and Li, respectively. In addition, Al content is 93% wt. and 94% wt. in AA2060 and AA2196, in that order. As copper have a thermal conductivity more than 5 times bigger and a heat specific capacity around 8 times smaller than Li, the amount of Cu in AA2060 has probably helped on the dispersion of temperature

while Li can have influenced the absorption of energy, contributing to the heat sink created near the welding center [46].

Moreover, hardness test performed over time revealed that both alloys had the microstructure stabilized after 5 weeks. The analysis was performed in an “as welded” (AW) condition, where soon after the sample temperature cool down, the samples were embbebed and set for hardness analysis. After this, the sample were weekly tested until the test shows stable results. The hardness curves obtained after 5 weeks and AW are displayed in Figure 5.22.

The main difference is the superior result presented by AA2060 in comparison with AA2196 samples in AW condition. It indicates a bigger degradation of the properties on AA2196 samples during welding. The first indication is that AA2196 plasticize easier. Heating and cooling rate presented indicates that AA2196 absorbs energy faster and dissipate energy slower than AA2060, what led to a higher time exposed at high temperature.

As the Cu/Li content influences the type of precipitates formed, in addition to others microstructural differences, this result indicates that the precipitates formed on AA2196 are more susceptible to temperature changes. This led to a bigger range of degraded material. Finally, the average loss of both welded alloys after stabilization was 30% in SZ.

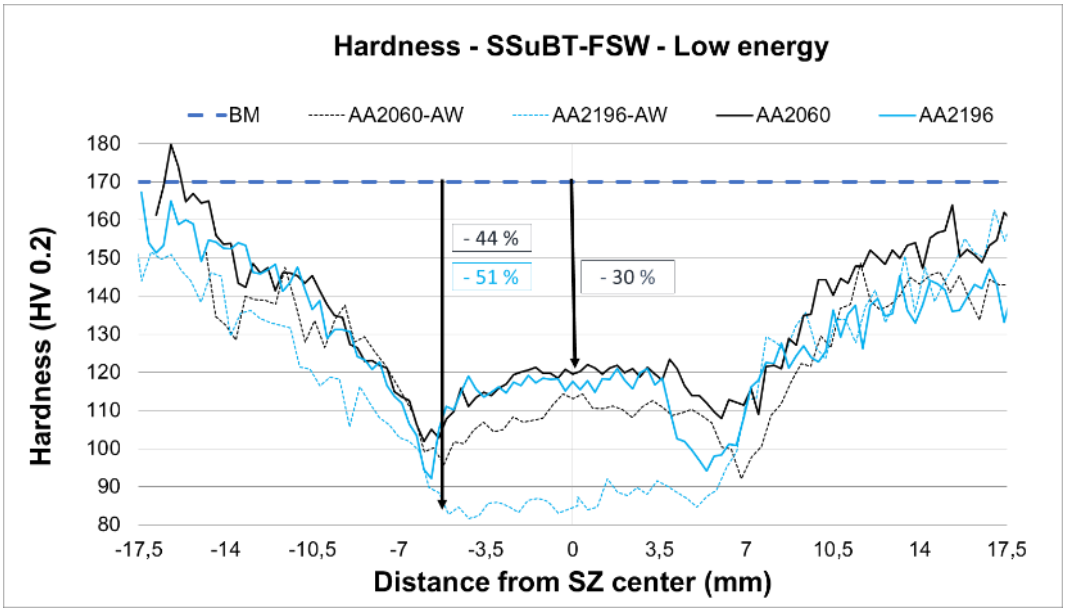

Figure 5.22 - Development of hardness profile of AA2060 and AA2196 welded by SSuBT-FSW over time (welding parameters: 200 RPM - 5500 N - 200mm/min). AW means as welded – hardness measured after around 2 hours from welding procedure.

Comparing the local mechanical behavior of both materials as welded and after stabilization, as presented in Figure 5.22, it can be observed that AA2196 has a higher recovery of the mechanical properties after some weeks. This is a strong indication of natural aging in AA2196.This behavior is verified by DSC presented in Figure 5.23.

Four main differences were observed on the behavior of the base materials (BM 2060 and BM 2196 – dashed lines). First, AA2196-T8 presented a more intense peak B than AA2060. This is linked to the bigger amount of Li on AA2196, what led to a higher amount of δ' (Al_3Li) precipitates that are not completely dissolute during T8 heat treatment. Second, peak C is observed at a higher temperature and presents a big plateau for AA2196. This consists with Decreus et al. [20] findings that shows T_1 phase precipitation occurs for longer aging times and happens more slowly in this alloy (AA2196) than in a Cu-rich alloy (AA2198).

Third, as peak D is related with formation of equilibrium phases, such as T_2 (Al_6Li_3Cu) and Tb ($Al_{7.5}LiCu_4$), [47,70], the lower amount of Cu available in

AA2196 could have led to a more stressed peak D due the formation of T_2 (Al_6Li_3Cu). Fourth, AA2196 BM peak E occurred in a higher temperature and presented a bigger area, than AA2060 BM peak E. This can be related as a consequence of the three factors before. Since peak E is related with dissolution of prior formed T_1 precipitates, secondary phases and equilibrium phases, such as T_2, Tb, θ and θ', the higher amount of precipitation occurred in peaks C and D could have led to a higher amount of precipitates to be dissolved. In addition, Decreus et al [20] found a larger saturation diameter of T_1 plates on Li-rich samples. This can be an indication of increase of precipitate size, which increases the stability of the precipitates by lowering the Gibbs–Thomson effect on AA2196.

As the aim of this research is to study the influence of Cu/Li ratio after BT-FSW, the DSC results of both alloys after welded need to be evaluated. The intensity of peak A in AA2196 SZ indicates a pronounced post-weld natural aging on this alloy. This was convergent with findings on hardness test performed on this work, as well as similar researches regarding Al-Li alloys under FSW [46,70].

At peak B, related with δ' (Al_3Li) precipitates dissolution, an increase of the intensity of AA2060 SZ compared with AA2060 BM can be observed, and an inverse effect is observed in AA2196 samples. The behavior of AA2196 can be explained by the behavior found at peak A. As the welding caused a higher post-weld natural aging on this alloy, most of δ' dissolution occurred at peak A, then the intensity of peak B reduces on the welded sample when compared with BM. That is also an indication that the post-weld precipitates were finer than AA2196-T8 (BM). Regarding AA2060, the increase on the intensity of peak B in the welded sample indicates a higher amount of δ' than in the BM. After the dissolution of precipitates on the SZ during welding, a higher amount of material was available on the matrix, but for thermodynamic reasons, the extent of post-welding aging was not as high as at AA2196. Then, during DSC heat cycle some of these available atoms reorganized in δ' precipitates, that were later dissolved in peak B [20,46,70].

Analyzing peak C, both welded alloys presented a transformation in higher temperatures and a more intense peak than the BM samples. Peak D was not visible for welded samples.

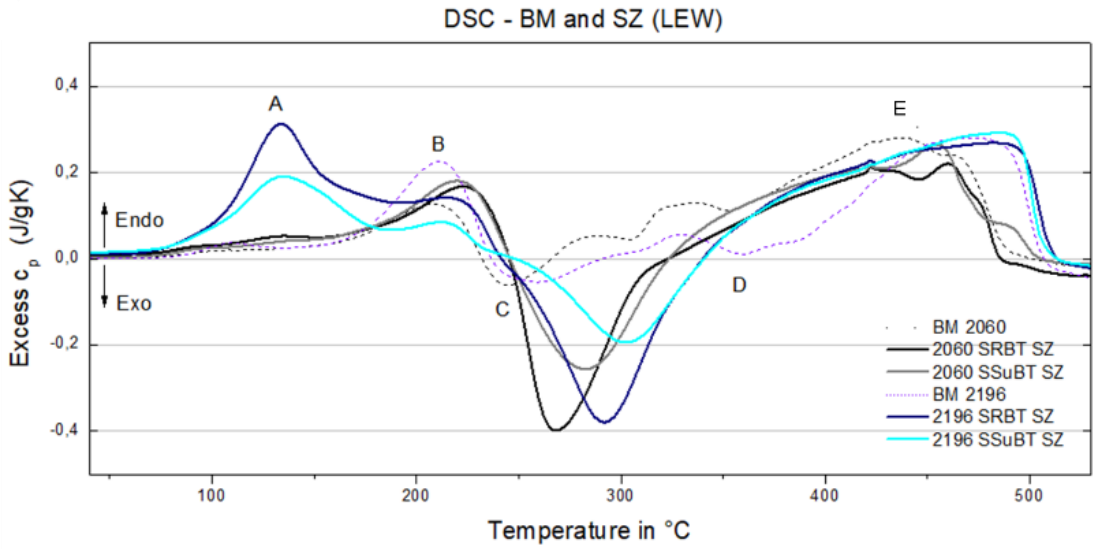

Figure 5.23 - Differential Scanning Calorimetry graph of SZ samples of AA2060 and AA2196 welded by SSuBT-FSW and SRBT-FSW low energy parameters.

5.3 Mechanical properties and fracture behavior of AA2060 and AA2196 welded by SSuBT-FSW and by SRBT-FSW

Welds produced by all different process parameter combination were subjected to tensile analysis. Tensile tests were performed in order to reveal the overall mechanical behavior caused by the thermal cycle described in section 5.2. All the mechanical tests were performed after 5 weeks from the welding procedure. This period was determined by experimental tests to analyze the time necessary for natural aging to occur and the material become stable.

5.3.1 Mechanical properties and fracture behavior of AA2060 welded by SSuBT-FSW and by SRBT-FSW

5.3.1.1 Mechanical properties and fracture behavior of AA2060 welded by SSuBT-FSW

As shown in Figure 5.8 and Figure 5.24, the overall mechanical behavior of the welds were not substantially affected by the energy input per length. Findings presented in Figure 5.24 is in accordance with hardness results, as the higher energy input promoted a slighter increase of precipitates growth and dissolution originating a more thermally affected HAZ and an increase of material aging that was responsible for the overall mechanical behavior of the samples.

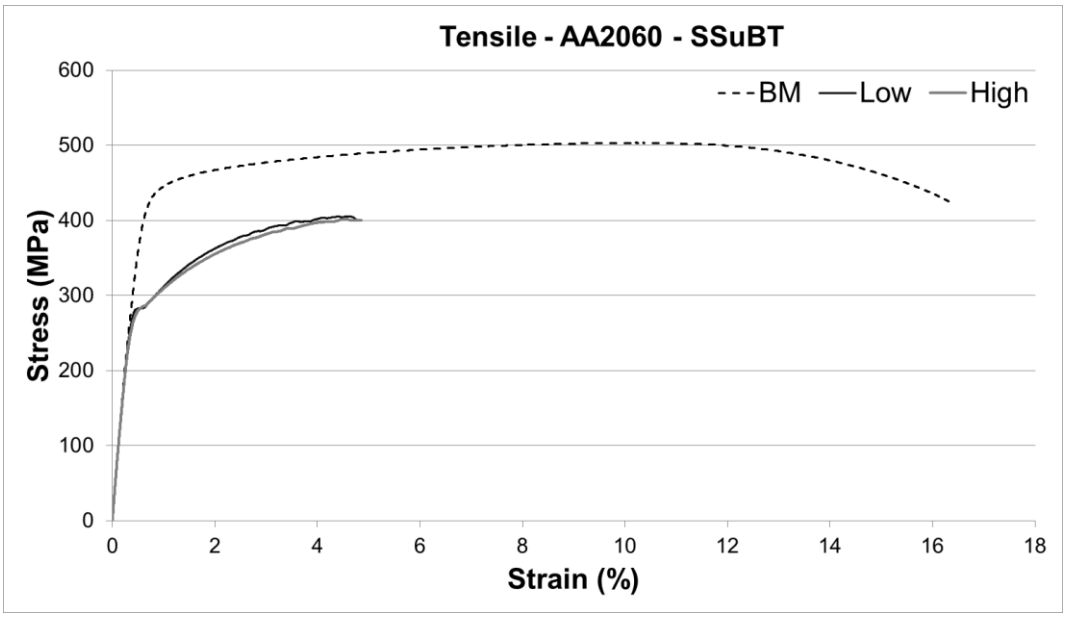

Figure 5.24 - Influence of energy input on the tensile test of AA2060 SSuBT-FSW samples.

Fracture initiates at a weak bonded area in the region of the interface between TMAZ/SZ at AS in AA2060-SSuBT-FSW samples, as showed in Figure 5.25. Evaluating post tensile testing visual images in Figure 5.26 and Figure 5.27 (a), it is possible to observe that the fracture surface seems to have two distinct areas revealed by the different texture and fracture surface brightness. Moreover, it is possible to notice in visual and microscope images that while both samples

fractured in TMAZ/SZ border, HEW samples had the crack breaking through TMAZ while LEW the crack occurred most inside SZ.

SEM analysis of fracture surface confirmed visual findings, as showed in Figure 5.27 (b). Fracture surface is clearly divided in two different microstructures. The crack follows the path of the sharp transition between the TMAZ and SZ. SZ is composed of fine-equiaxed recrystallized grains, while TMAZ is composed of high deformed recovered grains. Therefore, an interface with large grain size displacement and high misorientation led to a weak point of the material.

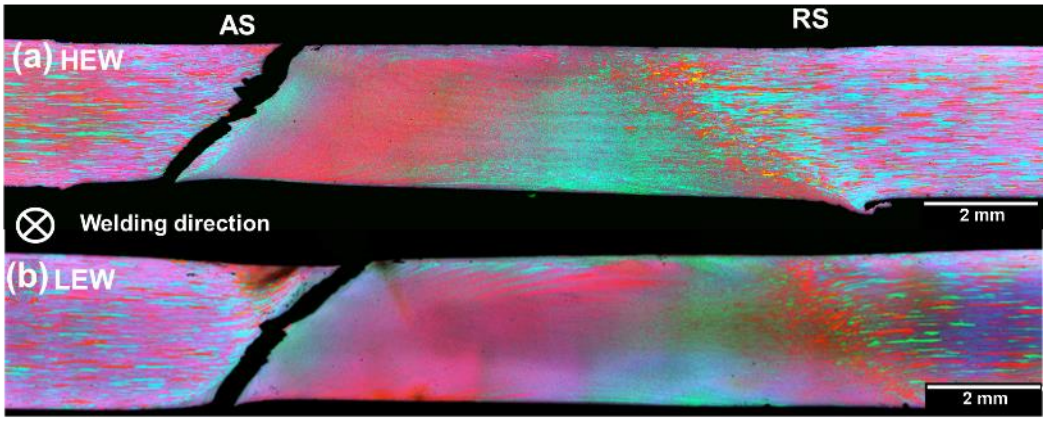

Figure 5.25 - Fracture location and shape observed by optical microscope in welding direction of AA2060 sample welded by (a) SSuBT-FSW HEW and (b) SSuBT-FSW LEW. All AA2060 samples welded by SSuBT-FSW in LEW and HEW presented fracture mode II.

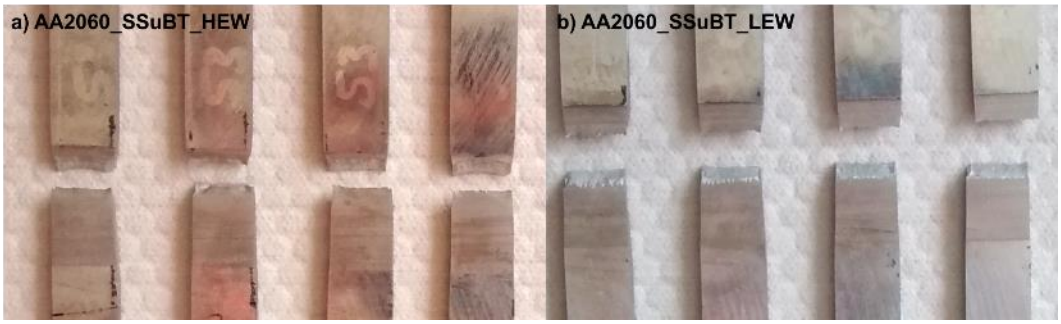

Figure 5.26 - Visual inspection of AA2060 - SSuBT (a) high energy parameter and (b) low energy parameter samples post tensile test.

Due to the border characteristic described above, a high concentration of stress and strain occurs when a tensile load is applied [65]. Consequently, voids

were created and began to merge following TMAZ/SZ border, as presented in Figure 5.27 (e) and (f). In the upper sections of the fracture surface (TMAZ), the crack follows among outward-bending angle. Fracture surface present in upper section of Figure 5.27 (b-e) shows a combination of cleavage facets and tearing edges as the crack propagates into the TMAZ. In addition, large cavities can be viewed as an indication of precipitate overaging on TMAZ. The lower section of Figure 5.27 (b) is showed in Figure 5.27 (g). The flat facets with relatively few shallow dimples on its surface suggest a brittle fracture, with some level of ductility.

Figure 5.28 presents SEM images of fracture in AA2060 – SSuBT-FSW LEW sample. As HEW samples, the fracture is characterized by cleavage facets and tearing edges with relatively few shallow dimples on its surface, as showed in high magnification presented in Figure 5.28 (e). It is important to highlight that both energy input parameters presented a crack propagation on 45^{o} angle up to sheet thickness.

The indentations in TMAZ/SZ border, near middle thickness sample, perpendicular to the tensile direction are an indication that crack initiation was situated in that location with strong signal of geometry influence. In addition, recalling Figure 3.19, it can be observed that failure path in AA2060-SSuBT-FSW samples passed through the surface of TMAZ/SZ border on AS, an area likely to occur defects due to material flow. Then, it is possible that the final crack goes through the weakest zone, but not necessarily where hardness lower value was measured.

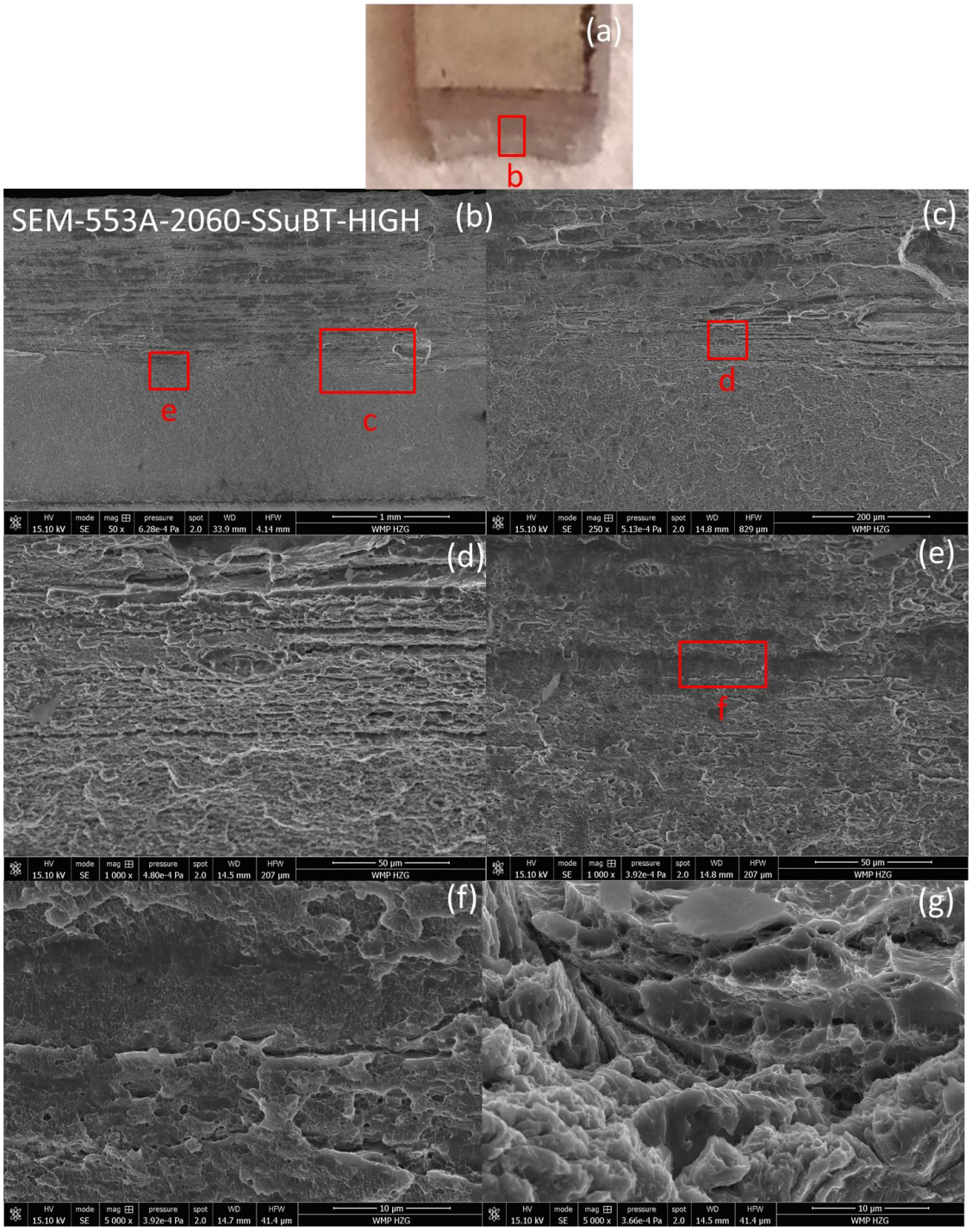

Figure 5.27 – Scanning electron micrographs of overall fracture of AA2060 – SSuBT- HEW sample. (a) presents the visual inspection and area where SEM were taken; (c) and (e) are magnified views of regions

marked in (b); (d) and (f) are magnified views of regions (c) and (e), respectively.

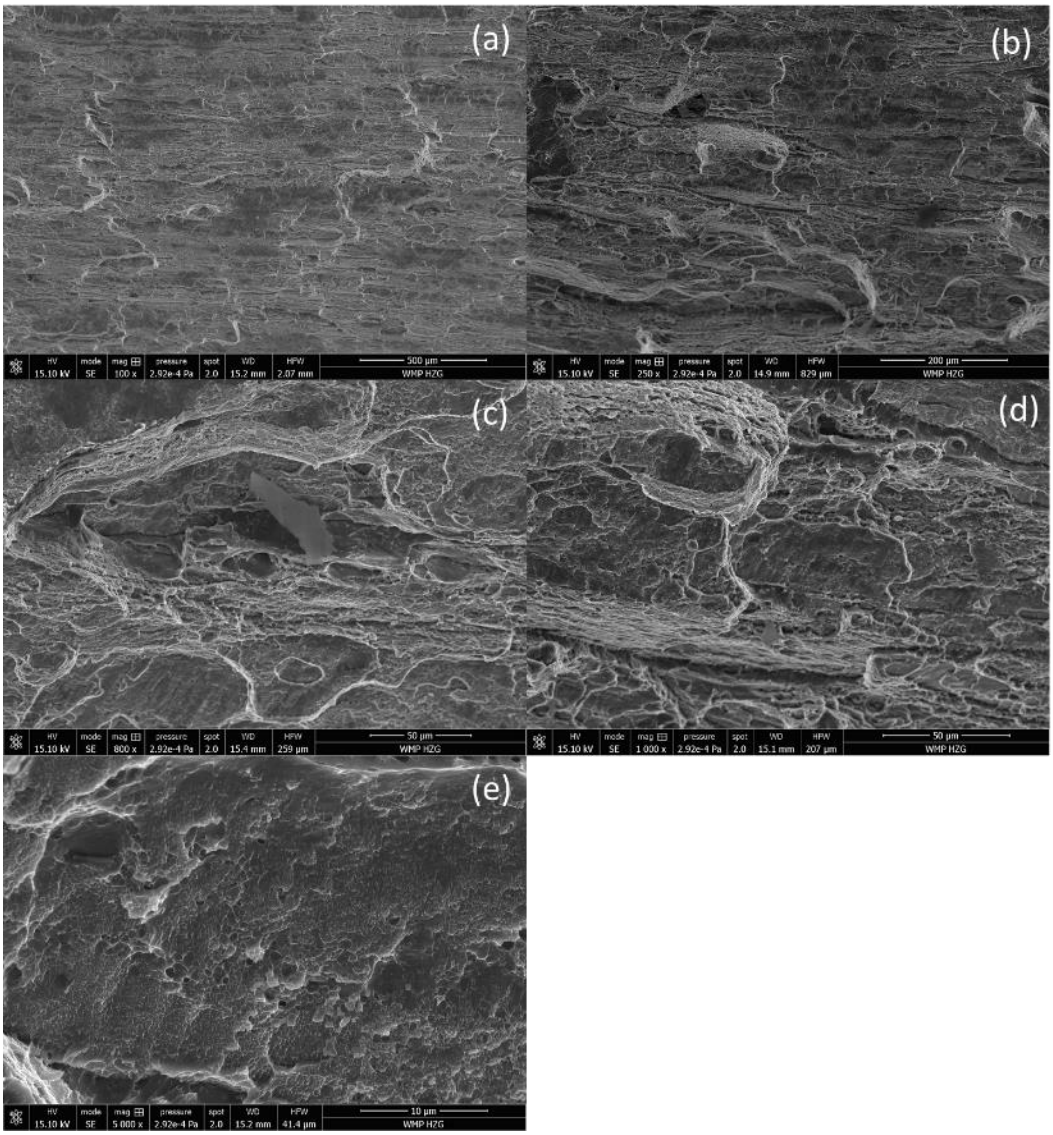

Figure 5.28 - Scanning electron micrographs of overall fracture of AA2060 – SSuBT- LEW sample. (a-e) are magnified views of regions of the fracture.

5.3.1.2 Mechanical properties and fracture behavior of AA2060 welded by SRBT-FSW

Tensile test in AA2060 samples welded by SRBT-FSW demonstrated that alterations in the welding parameters have effect in the overall mechanical performance of the welds. High energy input parameter samples presented an yield strength (YS) and an ultimate tensile strength (UTS) in average 11% and 19% smaller LEW samples. In addition, HEW samples had a maximum strain of 0.66% while LEW reached above 2% elongation. AA2060-T8 original sample elongated up to 16%.

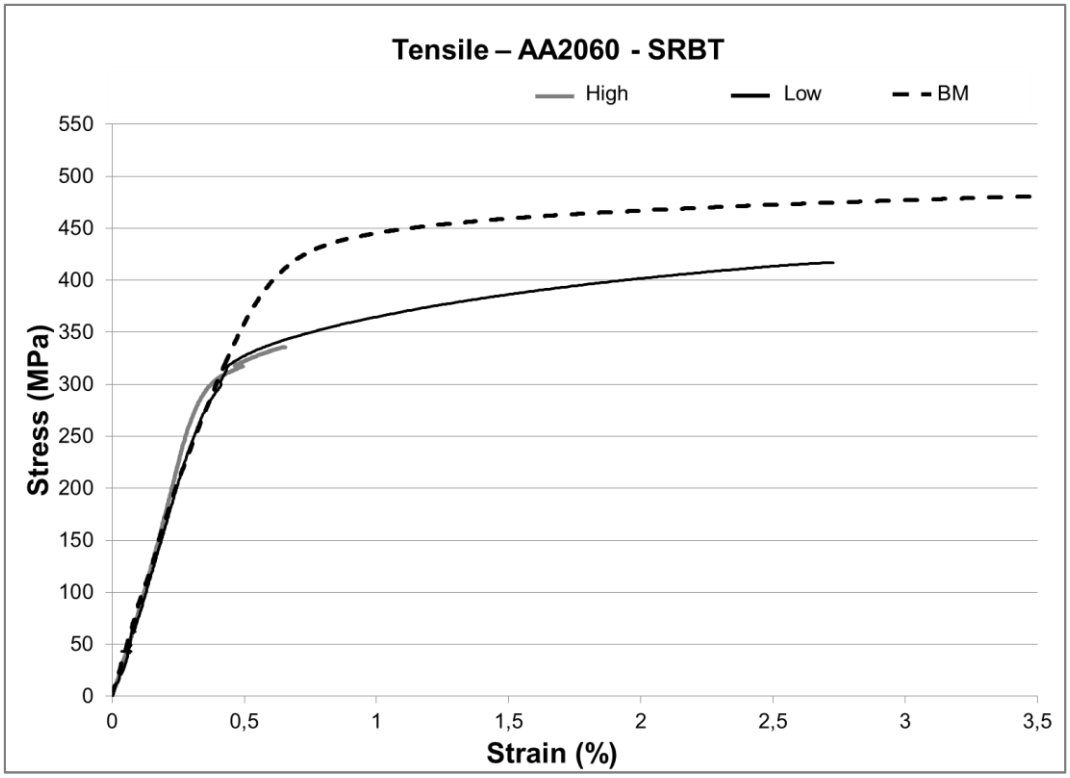

Figure 5.29 - Influence of energy input on the tensile test of AA2060 SRBT-FSW samples.

The fracture of AA2060-SRBT-FSW samples was analyzed in optical microscope. Fracture mode I occurred in all samples that presented the defect line presented in Figure 5.3 (c), this means, SRBT-FSW samples welded mainly in high energy input parameters in a butt joint configuration. As the defect was associated with the clamping system, samples were discarded. New samples

were welded using the same parameters bead on plate, I. e., the process was performed in a unique plate, only to analyze the effect of the welding variant on the metallurgical and mechanical evolution of the sample.

Most AA2060-SRBT samples failed on mode III fracture. Comparing fracture path of LEW and HEW samples presented in Figure 5.30 and Figure 5.31, respectively, it is possible to observe that the crack probably presents a geometric factor propagating perpendicular to the tensile direction in the TMAZ/SZ border at AS. The area also matches with the border of the probe, increasing the probability of geometric factor and related with material flow restrictions. Volumetric defects found near fracture surface seems similar to defects found due to non-optimal parameters caused by insufficient material flow on BT-FSW AA2198 [31]. The path of the crack in HEW samples corroborates with a brittle fracture in accordance with tensile test. Additional SEM images should be performed in future works to confirm these assumptions.

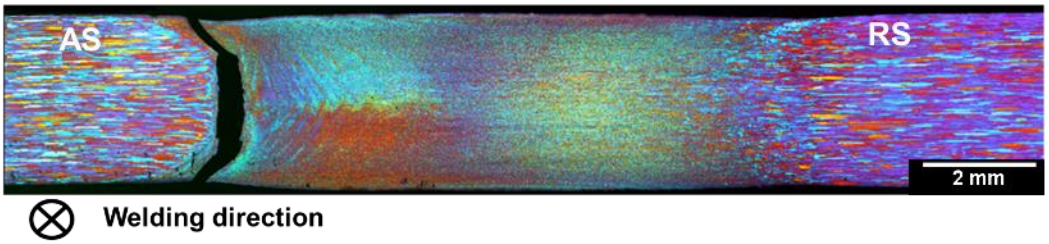

Figure 5.30 - Fracture mode III location and shape observed by optical microscope in welding direction of AA2060 sample welded by SRBT-FSW LEW.

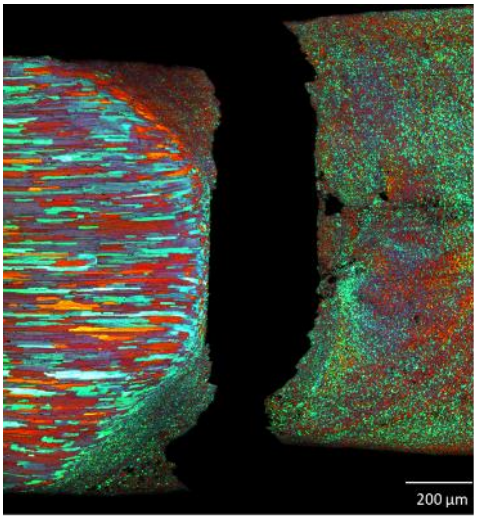

Figure 5.31 - AA2060-SRBT-FSW HEW fracture surface macrograph on optical microscope showing volumetric defects near the fracture surface mode III, at AS SZ/TMAZ border.

Comparing AA2060-SSuBT-FSW and AA2060-SRBT-FSW, Figure 5.25 and Figure 5.30, it can be observed that both samples failed in the border between TMAZ/SZ on the AS. However, AA2060-SRBT-FSW followed the border path, but failed completely inside the SZ. Recalling Figure 3.19, it can be observed that failure path in AA2060-SSuBT-FSW and AA2060-SRBT-FSW welds passed through the most likely areas to occur defects. It is possible that the final crack goes through the weakest zone, but not necessarily, where hardness lower value was measured.

5.3.2 Mechanical properties and fracture behavior of AA2196 welded by SSuBT-FSW and by SRBT-FSW

5.3.2.1 Mechanical properties and fracture behavior of AA2196 welded by SSuBT-FSW

Tensile test in AA2196 samples welded by SSuBT-FSW did not indicate a significant effect in the overall mechanical performance of the welds. For both energy parameters, samples presented a decrease of 41% and 34% in YS and UTS, respectively, compared with BM. Welded samples had an elongation of

around 3% prior fracture, while AA2196-T8 original sample elongated up to 12.5%. Figure 5.32 presents tensile curves of AA2196 samples welded by SSuBT-FSW in HEW and LEW. Figure 5.33 displays a fracture mode II observed by optical microscope in AA2196 welded by SSuBT-FSW LEW.

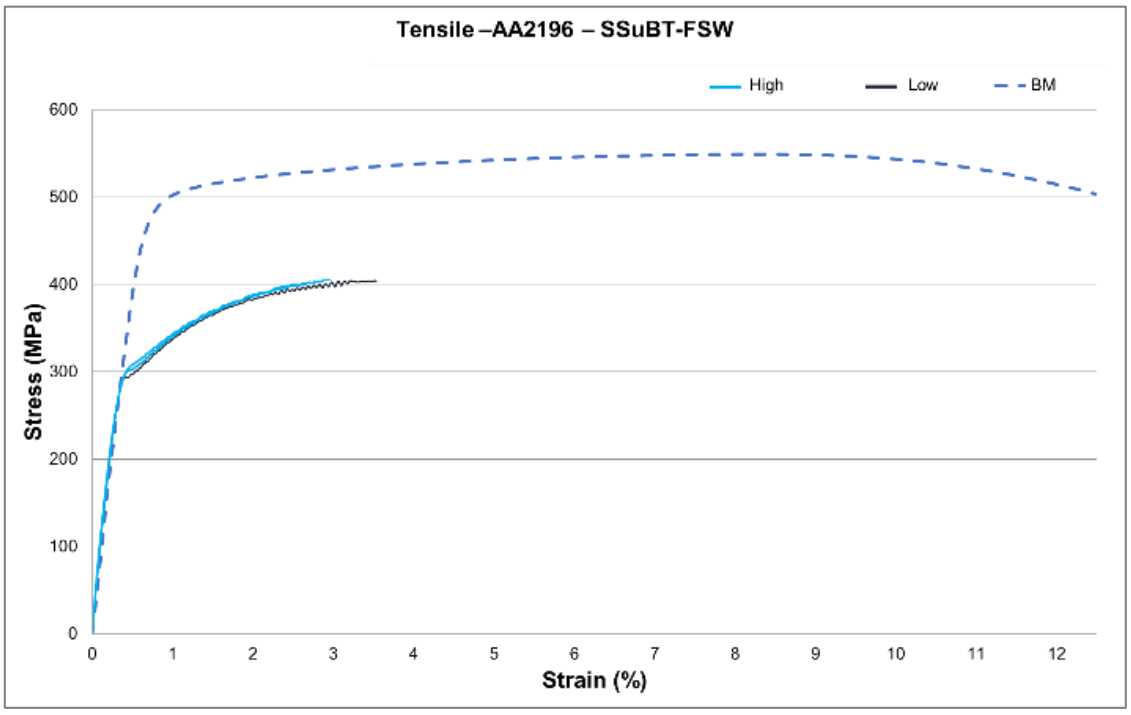

Figure 5.32 - Influence of energy input on the tensile test of AA2196 SSuBT-FSW samples.

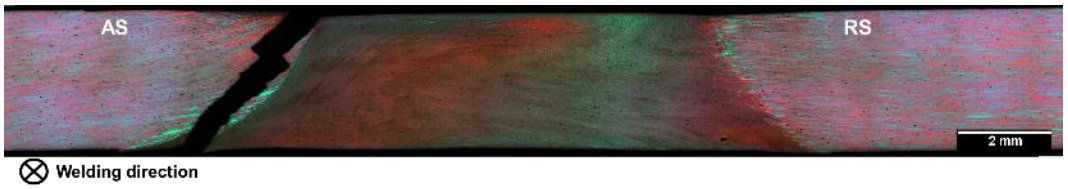

Figure 5.33 - Fracture location and shape observed by optical microscope in welding direction of AA2196 sample welded by SSuBT-FSW LEW. All AA2196 samples welded by SSuBT-FSW in LEW and HEW presented fracture mode II.

Scanning electron macrographs of the overall fracture of AA2196 SSuBT-FSW samples is presented in Figure 5.34. As AA2060-SSuBT-FSW samples, AA2196 SSuBT-FSW failed on the interface of TMAZ/SZ at advancing side in a

45° path, as showed in Figure 5.34 (a). Images obtained by SEM with 250x magnification of perpendicular to fracture in stationary shoulder surface, presented in Figure 5.34 (b), show interesting features in the upper surface similar to the ironing effect on the onion rings indicated in Figure 3.14. In the upper sections of the fracture surface (TMAZ), the crack follows among outward-bending angle. Fracture surface present in Figure 5.34 (b-f) shows a combination of cleavage facets and tearing edges as the crack propagates into the TMAZ. In addition, steps were observed on the fractured surfaces, as highlighted by red lines in Figure 5.34 (b), (e) and (f). These steps were linked in literature to the different plastic flow caused by probe and shoulder rotation, in addition to the direction of the welding as illustrated in Figure 3.18. The bonding strength of the plastic flow layers contributes to the strength of the SZ in welding direction [86].

From the high magnification factographs in Figure 5.34 (e-g), presence of shallow dimples indicates a level of ductility on the SZ. Coalescence microvoids can be seen on Figure 5.34 (g), as before reported in literature [19].

Figure 5.35 shows SEM images of the fracture surfaces of AA2196 SSuBT-FSW LEW samples. Fracture present a combination of cleavage facets and tearing edges with some shallow dimples on the surface of Figure 5.35 (e-g).

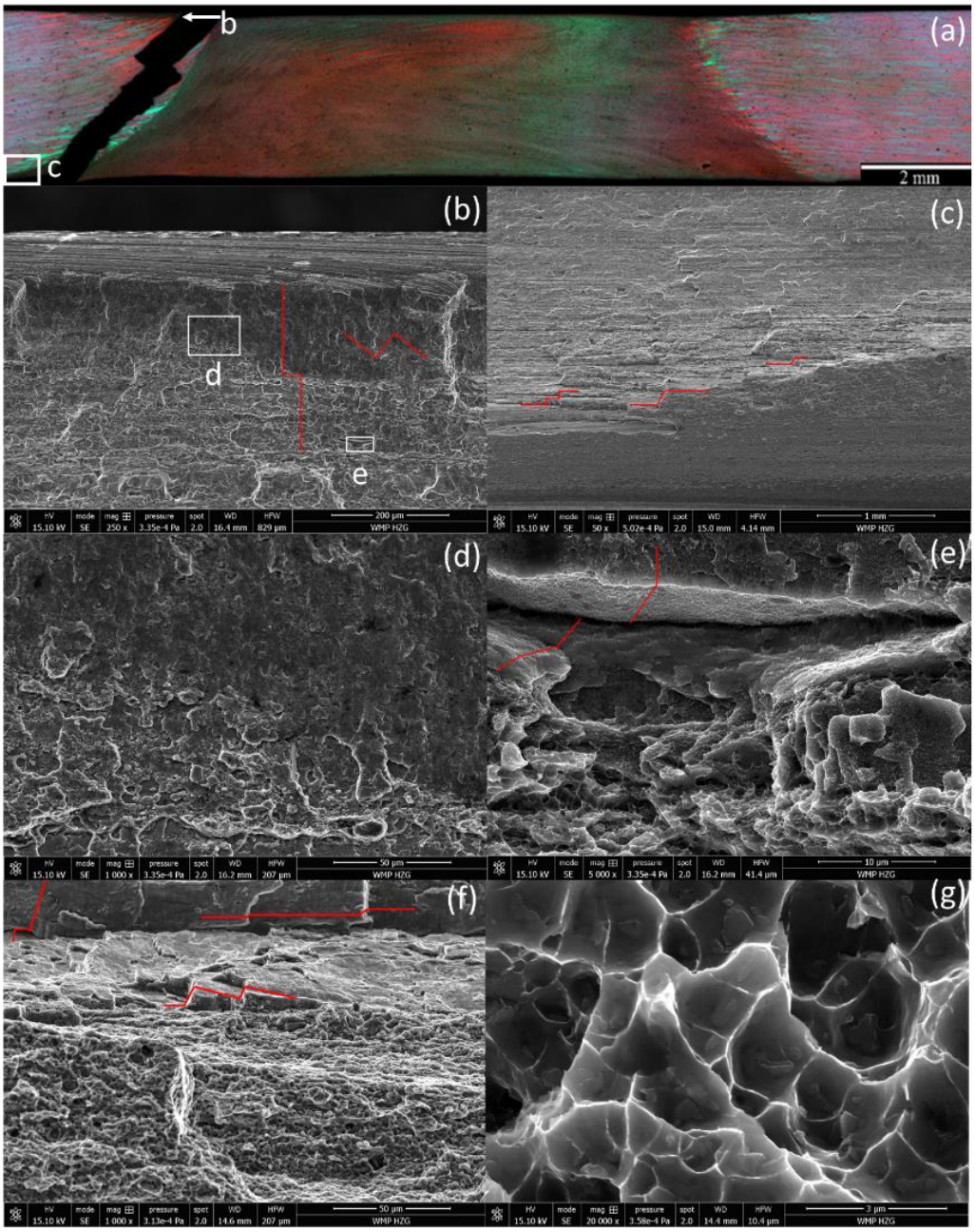

Figure 5.34 - Microscopic fracture surfaces of AA2196 SSuBT-FSW HEW tensile sample: (a) optical microscope macrograph illustrating SEM direction of (b) and (c); (b) SEM perpendicular to fracture in stationary shoulder surface; (c) SEM view of TMAZ/SZ interface near rotating shoulder surface; (d) and (e) are magnified views marked on (b); (f) is the magnified view of TMAZ/SZ interface presented in (c); (g) is the magnified view of SZ presented in (f).

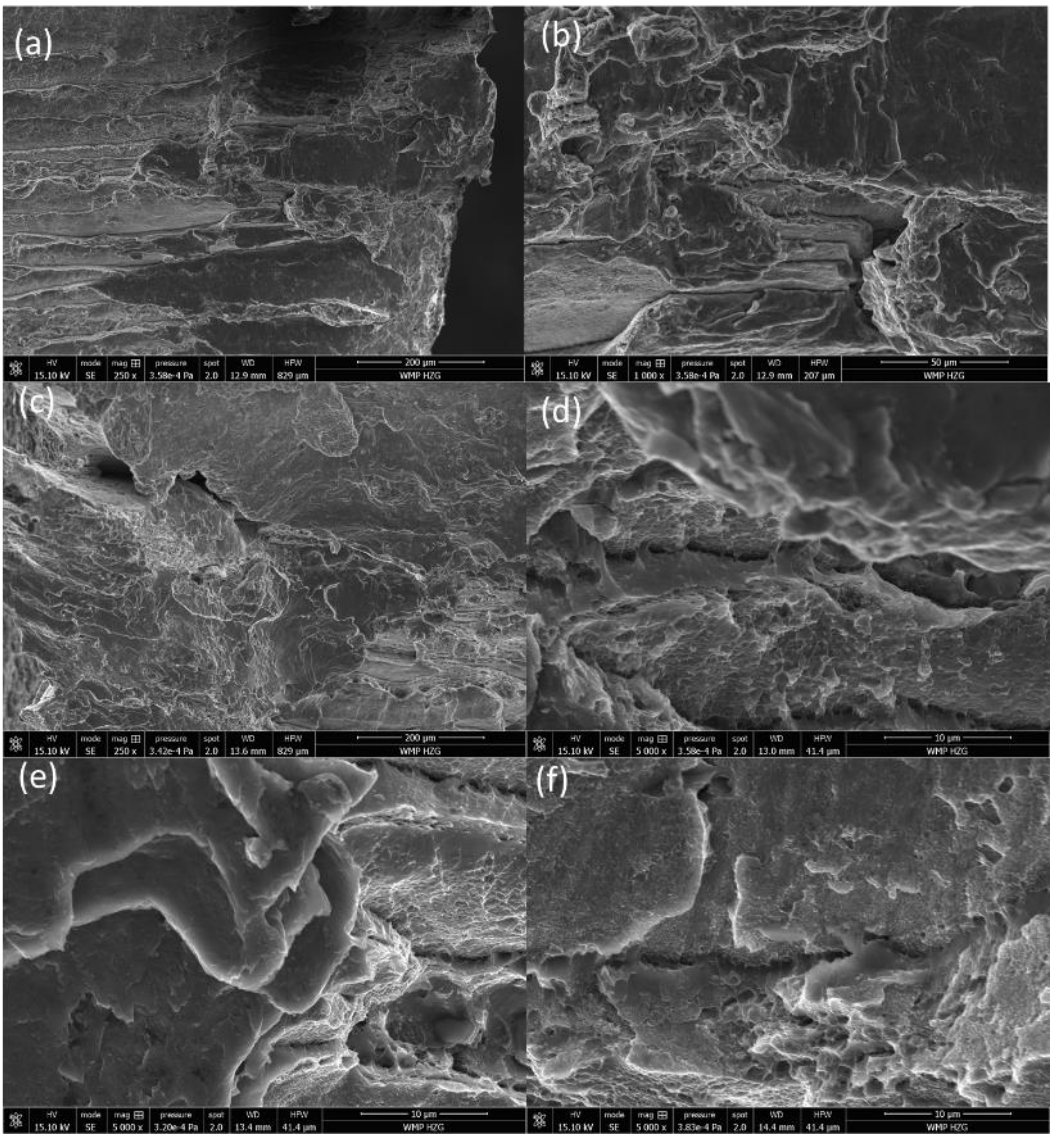

Figure 5.35 - Microscopic fracture surfaces of AA2196 SSuBT-FSW LEW tensile sample: (a) to (f) SEM magnified views perpendicular to fracture.

5.3.2.2 Mechanical properties and fracture behavior of AA2196 welded by SRBT-FSW

Tensile test in AA2196 samples welded by SRBT-FSW did not indicate a significant effect in the YS of the welded samples, but LEW showed higher elongation prior fracture and UTS than HEW samples. HEW and LEW samples presented a decrease of 31% and 22% in UTS, respectively, compared with BM. HEW samples had an elongation up to 1% and LEW of around 2.7% prior

fracture, while AA2196-T8 original sample elongated up to 12.5%. Figure 5.36 presents tensile curves of AA2196 samples welded by SRBT-FSW in HEW and LEW. Figure 5.37 displays a fracture mode IV observed by optical microscope in AA2196 welded by SRBT-FSW LEW.

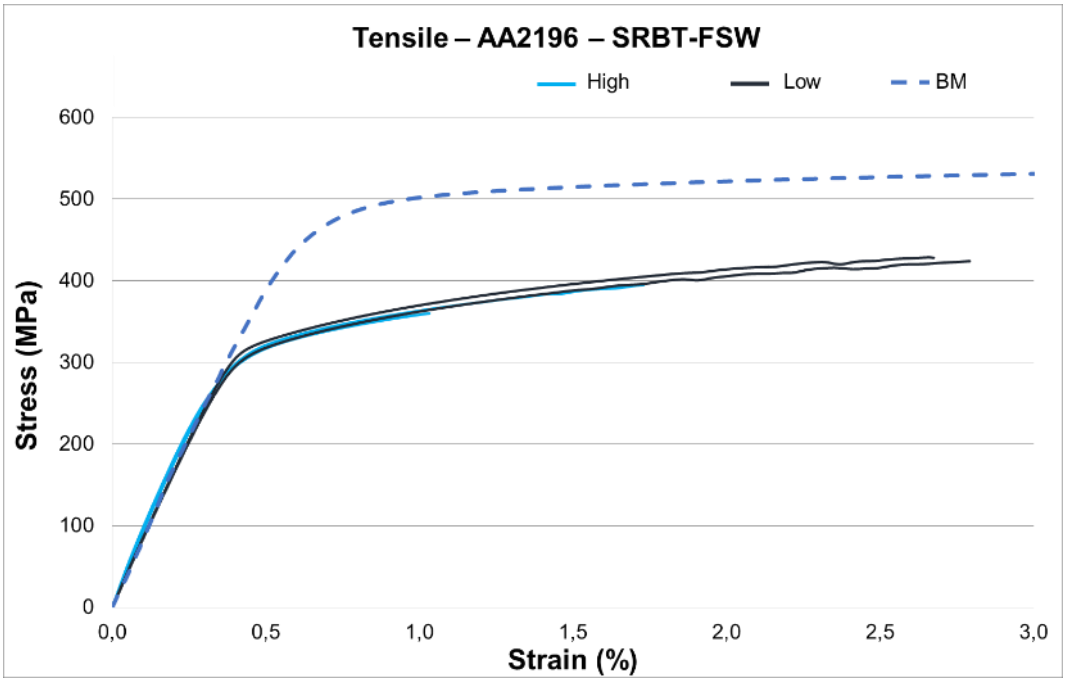

Figure 5.36 - Influence of energy input on the tensile test of AA2196 SRBT-FSW samples.

No fracture inspection of AA2196 welded by SRBT-FSW were performed in SEM. However, visual and optical microscope inspection showed in Figure 5.37 (a) indicates: (i) a noticeable necking on LEW samples that were not observed on samples ruptured on different fracture modes; (ii) a tear/void close to the center of the weld that coincides with the fracture location on HEW samples, as displayed in Figure 5.37 (c).

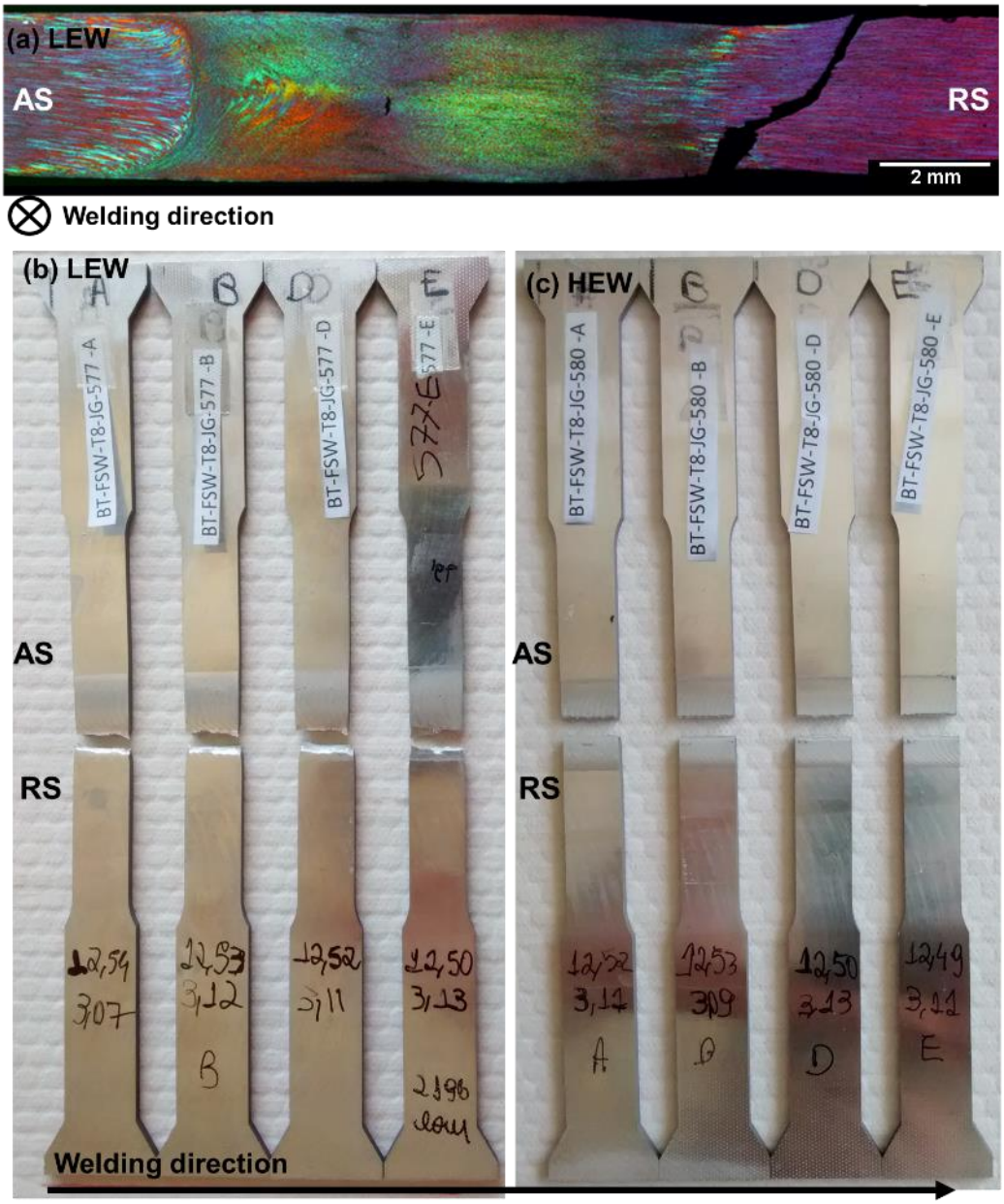

Figure 5.37 – (a) AA2196-SRBT-FSW LEW fracture surface macrograph on optical microscope showing volumetric defects near the welding center and a fracture surface mode IV, at RS trough TMAZ. (b) Post tensile picture of (a). (c) Post tensile picture of AA2196-SRBT-FSW HEW sample that fractured in mode I.

5.3.3 Main remarks

In general, mechanical properties and fracture behavior indicated that:

- Samples welded by SSuBT-FSW exhibited that increasing the traverse speed from 125mm/min (HEW) to 150mm/min (LEW) does not drove to difference in mechanical properties for both alloys. This is in accordance with microstructural analysis. In addition, all samples welded by SSuBT-FSW displayed a fracture mode II;
- Samples welded by SRBT-FSW showed that shifting traverse speed from around 600mm/min (HEW) to 800mm/min (LEW) led to significant difference in mechanical behavior of the welds, mainly related with the impact of the processes in TMAZ and HAZ. This can be stated due to hardness results that did not showed differences inside the SZ between the energy parameters, but showed significant variances on UTS and elongation at fracture;
- Fracture mode I, III and mode IV were found in samples welded by SRBT-FSW .The first mode occurred when the non-consolidation oxide line was existent (butt joint configuration) and mode III when the oxide line was not available (bead on plate). Only AA2196 welded by SRBT-FSW failed in mode IV;
- For both alloys, the better mechanical performance was achieved when welding using SRBT-FSW LEW parameters.

Table 5.6 shows average mechanical performance of the welds. After tensile testing, a microscopic inspection was performed to verify the location and the mode of the fracture on each parameter and alloy under study. Table 5.7 presented below shows fracture modes established and its descriptions.

Table 5.6 – Average mechanical properties of BM and welds per alloy, BT-FSW variant and energy input level.

Alloy – BT-FSW variant – Energy input level	BM YS/UTS [MPa]	YS [MPa]	UTS [MPa]	BM hardness [Hv]	SZ hardness [Hv]	Lowest hardness [Hv]	Elonga-tion at fracture
AA2060 – T8 SSuBT - HEW	417/503	278 ± 8	383 ± 28	169	119 ± 2	102	3.5 ± 1.1
AA2060 – T8 SSuBT - LEW	417/503	284 ± 8	398 ± 14	169	118 ± 2	107	3.6 ± 0.9
AA2060 – T8 SRBT - HEW	417/503	298± 20	320 ± 13	169	128 ± 2	122	0.3 ± 0.3
AA2060 – T8 SRBT - LEW	417/503	338 ± 17	394 ± 21	169	130 ± 3	124	1.5 ± 0.7
AA2196 – T8 SSuBT - HEW	485/549	283 ± 34	354 ± 76	169	117 ± 2	92	1.9 ± 1.2
AA2196– T8 SSuBT - LEW	485/549	285 ± 13	364 ± 46	169	114 ± 1	98	2.1 ± 1.1
AA2196– T8 SRBT - HEW	485/549	334 ± 3	380 ± 24	169	130 ± 6	105	0.5 ± 0.5
AA2196– T8 SRBT - LEW	485/549	335 ± 4	429 ± 4	169	133± 3	116	2.5 ± 0.4

Table 5.7- Fracture mode and description.

Fracture mode	Description
I	Brittle fracture at defect line
II	Fracture on SZ at the border of TMAZ, 45° inclined to the loading direction
III	Fracture on SZ at the border of TMAZ, following TMAZ border
IV	Fracture on HAZ, 45° inclined to the loading direction

6 CONCLUSIONS

The results obtained in this work indicated that both variants of Bobbin Tool Friction Stir Welding, Self-Reacting BT-FSW (SRBT-FSW) and Stationary (upper) Shoulder BT-FSW (SSuBT-FSW), have been shown to be suitable for welding Al-Li AA2060 and AA2196 alloys. In addition, some conclusions could be obtained in this work:

- SSuBT-FSW variant presented a more restricted processing window, considering the alloys under study and tool available. At welding speeds as high as the applied in SRBT-FSW, the energy input generated by SSuBT-FSW process was not enough to plasticize the material causing excessive loads on the probe. Consequently, the forces imposed for rotation and translation of the tool triggered the breakage of the probe. Then, there was no possibility of replicating the welding parameters applied in SRBT-FSW variant. Thus, without the development / application of new material and / or tool design, the SSuBT-FSW variant does not fulfill the objective of reducing the energy input during welding;
- In general, SRBT-FSW process led to better mechanical properties on both welded alloys. That was related with the longer exposure time at higher temperatures in SSuBT-FSW variant what guided to a more pronounced degradation of the material original properties;
- Overall, AA2060 revealed a better mechanical answer than AA2196 to SSuBT-FSW process. AA2060 welded by SSuBT-FSW reached up to 68% of BM yield strength and 79% of BM UTS. Meanwhile, AA2196 achieved 59% and 66% of YS and UTS of AA2196-T8 condition;
- Regarding SRBT-FSW, AA2060 welded samples presented a higher YS and hardness and a lower UTS and elongation performance compared to BM than AA2196 welds;
- AA2196 presented a higher degree of post welding natural aging than AA2060. This was verified during Differential Scanning Calorimetry (DSC) and hardness test. In DSC, it was confirmed by a more stressed peak A related with the dissolution of δ’ (Al_3Li) with the natural aging process

driven by the high amount of Li on this alloy. In addition, that was demonstrated in hardness over time graph that showed a higher recover of SZ hardness in AA2196 when comparing with AA2060. Natural aging was promoted in a higher extend in SRBT-FSW samples;

- Samples welded by SRBT-FSW showed that increasing traverse speed from around 600mm/min (HEW) to 800mm/min (LEW) led to significant difference in mechanical behavior of the welds, mainly related with the impact of the processes in TMAZ and HAZ. The rise of 229 mm / min meant that the mechanical strength (UTS) of alloy AA2060 were increased from 320MPa to 394MPa and elongation at fracture were shifted from 0.3% to 1.4%. AA2196 samples had UTS and strain increased from 380MPa and 0.5% to 429MPa and 2.5%, respectively, increasing 200 mm/min on traverse speed.

7 SUGGESTIONS FOR FUTURE WORKS

Although a satisfactory evaluation of BT-FSW variants of AA2060-T8 and AA2196-T8 for aerospace applications was successfully achieved, additional analysis is proposed to have a more comprehensive investigation.

- Identify by integrated EBSD and energy dispersive spectroscopy technique the chemical composition of particles found during SEM of the fracture;
- Investigating reprecipitation and overaging process in different weld regions using Transmission Electron Microscope (TEM) and tomography techniques as 3DAP;
- Analyze the DSC results of both alloys to identify the effect of SRBT-FSW and SSuBT-FSW and Cu/Li ratio on HAZ;
- Study the effect of energy input on the distance of fracture from the welding center in SSuBT-FSW samples after tensile test;
- Perform corrosion and stress corrosion tests to verify the effect of BT-FSW variants on the corrosion behavior of the alloys;
- Evaluate the application of different material and/or design on tool/probe in order to perform SSuBT-FSW in higher welding speed.

8 REFERENCES

1. CALKINS, M. The future of metals. **Materials for sustainable sites A complete guide to the Evaluation, selection, and Use of sustainable construction materials**, V. 328, 2010, 369.
2. RIOJA, R. J. & LIU, J. The evolution of Al-Li base products for aerospace and space applications. **Metallurgical and Materials Transactions A: Physical Metallurgy and Materials Science**, V. 43, 2012, 3325–3337.
3. POLMEAR, I. Aluminium Alloys--A Century of Age Hardening. **Materials forum**, V. 28, 2004, 1–14.
4. GIUMMARRA, C.;THOMAS, B. & RIOJA, R. New Aluminum alloys for aerospace applications. **Proceedings of the Light Metals Technology Conference 2007**, 2007, doi:4B13A37E48BB17CE0CC5FD14DA676F42
5. DURSUN, TOLGA; SOUTIS, C. Recent developments in advanced aircraft aluminium alloys. **Materials and Design**, V. 56, 2014, 862–871.
6. STEMART, C. Fuel and Flight Efficiency Services by Airbus. in **AACO 7th Aviation Fuel Forum** (2015). 1–29.
7. THÉVENIN, R. Composites in Airbus: A Long Story of Innovations and Experiences. **Global Investor Forum** 2008, 1–26.
8. WANHILL, R. J. H. Aerospace Applications of Aluminum-Lithium Alloys. in **Aluminum-Lithium Alloys: Processing, Properties, and Applications** (2013). doi:10.1016/B978-0-12-401698-9.00015-X
9. MISHRA, R. S. & MA, Z. Y. Friction stir welding and processing. **Materials Science and Engineering R: Reports** 2005, doi:10.1016/j.mser.2005.07.001
10. ESMAILY, M.;MORTAZAVI, N.;OSIKOWICZ, W.;HINDSEFELT, H.;SVENSSON, J. E.;HALVARSSON, M.;MARTIN, J. & JOHANSSON, L. G. Bobbin and conventional friction stir welding of thick extruded AA6005-T6 profiles. **Materials {&} Design**, 2016, doi:10.1016/j.matdes.2016.06.089
11. ÇAM, G. & MISTIKOGLU, S. Recent developments in friction stir welding of al-Alloys. **Journal of Materials Engineering and Performance**, V. 23,

2014, 1936–1953.

12. HILGERT, J. Knowledge Based Process Development of Bobbin Tool Friction Stir Welding. (2012).
13. GAO, C.;ZHU, Z.;HAN, J. & LI, H. Correlation of microstructure and mechanical properties in friction stir welded 2198-T8 Al-Li alloy. **Materials Science and Engineering A**, V. 639, 2015, 489–499.
14. NANDAN, R.;DEBROY, T. & BHADESHIA, H. K. D. H. Recent advances in friction-stir welding – Process, weldment structure and properties. **Progress in Materials Science**, V. 53, 2008, 980–1023.
15. NUNES, A. C. jr.;RUSSELL, C. K.;BROOKE, S. A.;PARRY, Q. & LOWREY, N. M. Laser Ablation Cleaning of Self-Reacting Friction Stir Weld Seam Surfaces: A Preliminary Evaluation. **Nasa**, 2014,
16. POLMEAR, I. J. PHYSICAL METALLURGY OF ALUMINIUM ALLOYS. in **Light Alloys: From traditional Alloys to Nanocrystals** (2005). 29–96.
17. AMERICAN SOCIETY FOR METALS. *Aluminum Properties and Physical Metallurgy*. **ASM International** (1984). doi:10.1361/appm1984p001
18. KAUFMAN, J. G. Understanding Wrought and Cast Aluminum Alloys Designations. **Introduction to Aluminum Alloys and Tempers**, 2000, doi:10.1361/iaat2000p02323–37.
19. ZHANG, S. fei;ZENG, W. dong;YANG, W. hua;SHI, C. ling & WANG, H. jun. Ageing response of a Al-Cu-Li 2198 alloy. **Materials and Design**, V. 63, 2014, 368–374.
20. DECREUS, B.;DESCHAMPS, A.;DE GEUSER, F.;DONNADIEU, P.;SIGLI, C. & WEYLAND, M. The influence of Cu/Li ratio on precipitation in Al-Cu-Li-x alloys. **Acta Materialia**, V. 61, 2013, 2207–2218.
21. CALLISTER JR., W. D.; RETHWISCH, D. G. *Materials Science and Engineering: An Introduction*. (Wiley, 2017).
22. MOURITZ, A. P. *Introduction to aerospace materials Related titles :* (Woodhead Publishing Limited, 2012).
23. STARINK, M. J.;WANG, P.;SINCLAIR, I. & GREGSON, P. J. Microstrucure and strengthening of Al–Li–Cu–Mg alloys and MMCs: II. Modelling of yield strength. **Acta Materialia**, V. 47, 1999, 3855–3868.

24. SEIDMAN, D. N.;MARQUIS, E. A. & DUNAND, D. C. Precipitation strengthening at ambient and elevated temperatures of heat-treatable Al(Sc) alloys. **Acta Materialia**, V. 50, 2002, 4021–4035.
25. ASHJARI, M. & JODEIRI FEIZI, A. 7Xxx Aluminum Alloys; Strengthening Mechanisms and Heat Treatment: a Review. **Material Science & Engineering International Journal**, V. 2, 2018, 52–56.
26. AZARNIYA, A.;TAHERI, A. K. & TAHERI, K. K. Recent advances in ageing of 7xxx series aluminum alloys: A physical metallurgy perspective. **Journal of Alloys and Compounds**, V. 781, 2019, 945–983.
27. TOTTEN, G. E. *Handbook of Aluminum*. **Corrosion** V. 2, (Marcel Dekker, Inc, 2003).
28. HALL E. O. The deformation and ageing of mild steel: II Characteristics of the Lüders deformation. **Proceedings of the Physical Society. Section B**, V. 64, 1951, 742–747.
29. PETCH, N. J. The Cleavage Strength of Polycrystals. **The Journal of the Iron and Steel Institute**, V. 173, 1953, 25–28.
30. DESCHAMPS, A.;MARTIN, G.;DENDIEVEL, R. & VAN LANDEGHEM, H. P. Allègement des structures dans les transports : le rôle de l'innovation en métallurgie. **Comptes Rendus Physique**, V. 18, 2017, 445–452.
31. GOEBEL, J.;REIMANN, M.;NORMAN, A. & DOS SANTOS, J. F. Semi-stationary shoulder bobbin tool friction stir welding of AA2198-T851. **Journal of Materials Processing Technology**, V. 245, 2017, 37–45.
32. BELOV, N.A.; ESKIN, D. G.; AKSENOV, A. A. *Multicomponent Phase Diagrams: Applications for Commercial Aluminum Alloys*. (Elsevier, 2005).
33. LIU, H.;HU, Y.;DOU, C. & SEKULIC, D. P. An effect of the rotation speed on microstructure and mechanical properties of the friction stir welded 2060-T8 Al-Li alloy. **Materials Characterization**, V. 123, 2017, 9–19.
34. CAI, B.;ZHENG, Z. Q.;HE, D. Q.;LI, S. C. & LI, H. P. Friction stir weld of 2060 Al-Cu-Li alloy: Microstructure and mechanical properties. **Journal of Alloys and Compounds**, V. 649, 2015, 19–27.
35. SCHNEIDER, J. A.;NUNES, A. C.;CHEN, P. S. & STEELE, G. TEM study of the FSW nugget in AA2195-T81. **Journal of Materials Science**, V. 40,

2005, 4341–4345.

36. FARD, M. H. & FARD, M. H. IMPACTS OF WELDING ON ENVIRONMENTAL PROBLEMS AND. 2016, 4–7.
37. SU, J. Q.;NELSON, T. W.;MISHRA, R. & MAHONEY, M. Microstructural investigation of friction stir welded 7050-T651 aluminium. **Acta Materialia**, V. 51, 2003, 713–729.
38. HORTON, K. R. Microhardness, Strength and Strain Field Characterization of Self-Reacting Friction Stir and Plug Welds of Dissimilar Aluminum Alloys. (The University of Alabama, 2011).
39. LI, W. Y.;FU, T.;HÜTSCH, L.;HILGERT, J.;WANG, F. F.;DOS SANTOS, J. F. & HUBER, N. Effects of tool rotational and welding speed on microstructure and mechanical properties of bobbin-tool friction-stir welded Mg AZ31. **Materials {&} Design**, V. 64, 2014, 714–720.
40. HOU, J. C.;LIU, H. J. & ZHAO, Y. Q. Influences of rotation speed on microstructures and mechanical properties of 6061-T6 aluminum alloy joints fabricated by self-reacting friction stir welding tool. **The International Journal of Advanced Manufacturing Technology**, V. 73, 2014, 1073–1079.
41. SCUPIN, P. Semi-Stationary Shoulder Bobbin Tool (S 3 BT): A New Approach in High Speed Friction Stir Welding. (2015).
42. WANG, F. F.;LI, W. Y.;SHEN, J.;HU, S. Y. & DOS SANTOS, J. F. Effect of tool rotational speed on the microstructure and mechanical properties of bobbin tool friction stir welding of Al–Li alloy. **Materials {&} Design**, V. 86, 2015, 933–940.
43. HUANG, Y. X.;HAN, B.;LV, S. X.;FENG, J. C.;LIU, H. J.;LENG, J. S. & LI, Y. Interface behaviours and mechanical properties of filling friction stir weld joining AA 2219. **Science and Technology of Welding and Joining**, V. 17, 2012, 225–230.
44. WU, H.;CHEN, Y. C.;STRONG, D. & PRANGNELL, P. Stationary shoulder FSW for joining high strength aluminum alloys. **Journal of Materials Processing Technology**, V. 221, 2015, 187–196.
45. SHEN, J.;WANG, F.;SUHUDDIN, U. F. H.;HU, S.;LI, W. & DOS SANTOS,

J. F. Crystallographic Texture in Bobbin Tool Friction-Stir-Welded Aluminum. **Metallurgical and Materials Transactions A: Physical Metallurgy and Materials Science**, V. 46, 2015, 2809–2813.

46. ENTRINGER, J.;REIMANN, M.;NORMAN, A. & DOS SANTOS, J. F. Influence of Cu/Li ratio on the microstructureevolution of bobbin-tool friction stir weldedAl-Cu-Li alloys. **Journal of Materials Research and Technology**, V. 8, 2019, 1–19.
47. ENTRINGER, J.;REIMANN, M.;NORMAN, A. & DOS SANTOS, J. F. Influence of Cu/Li ratio on the microstructure evolution of bobbin-tool friction stir welded Al-Cu-Li alloys. **Journal of Materials Research and Technology**, V. 8, 2019, 2031–2040.
48. FRIGAARD, Ø.;GRONG, Ø. & MIDLING, O. T. A process model for friction stir welding of age hardening aluminum alloys. **Metallurgical and Materials Transactions A**, V. 32, 2001, 1189–1200.
49. LAMPEAS, G. N. & DIAMANTAKOS, I. D. Effects of Nonconventional Tools on the Thermo-Mechanical Response of Friction Stir Welded Materials. **Journal of Manufacturing Science and Engineering**, V. 137, 2015, 051020.
50. ESMAILY, M.;MORTAZAVI, N.;OSIKOWICZ, W.;HINDSEFELT, H.;SVENSSON, J. E.;HALVARSSON, M.;THOMPSON, G. E. & JOHANSSON, L. G. Corrosion behaviour of friction stir-welded AA6005-T6 using a bobbin tool. **Corrosion Science**, 2016, doi:10.1016/j.corsci.2016.04.046
51. DOUDE, H.;SCHNEIDER, J.;PATTON, B.;STAFFORD, S.;WATERS, T. & VARNER, C. Optimizing weld quality of a friction stir welded aluminum alloy. **Journal of Materials Processing Technology**, V. 222, 2015, 188–196.
52. KRISHNAN, K. N. On the formation of onion rings in friction stir welds. **Materials Science and Engineering A**, V. 327, 2002, 246–251.
53. PRANGNELL, P. B. & HEASON, C. P. Grain structure formation during friction stir welding observed by the ‘stop action technique’. **Acta Materialia**, V. 53, 2005, 3179–3192.

54. KIM, Y. G.;FUJII, H.;TSUMURA, T.;KOMAZAKI, T. & NAKATA, K. Three defect types in friction stir welding of aluminum die casting alloy. **Materials Science and Engineering A**, V. 415, 2006, 250–254.

55. PLAINE, A. H. & ALCÂNTARA, N. G. de. Prediction of Friction Stir Welding defect-free joints of AISI 304 austenitic stainless steel through axial force profile understanding. **Materials Research**, V. 17, 2014, 1324–1327.

56. THREADGILL, P. L.;LEONARD, A. J.;SHERCLIFF, H. R. & WITHERS, P. J. Friction Stir Welding of Aluminium Alloys. **International Materials Reviews**, V. 54, 2009, 49–93.

57. ZETTLER, R.; LOMOLINO, S. *Study on root flaws in 4mm thick AA2024-T351 FSW Joints*. (2004).

58. WAN, L.;HUANG, Y.;GUO, W.;LV, S. & FENG, J. Mechanical Properties and Microstructure of 6082-T6 Aluminum Alloy Joints by Self-support Friction Stir Welding. **Journal of Materials Science {&} Technology**, V. 30, 2014, 1243–1250.

59. SHUJIN CHEN;ALI LU;DAILI YANG;SHENG LU;JIHONG DONG & CHUNLIN DONG. *Analysis on flow pattern of bobbin tool friction stir welding for 6082 aluminum*. (2013).

60. OKAMOTO, K.;SATO, a.;PARK, S. H. C. & HIRANO, S. Microstructure and Mechanical Properties of FSWed Aluminum Extrusion with Bobbin Tools. **Materials Science Forum**, V. 706–709, 2012, 990–995.

61. JARIYABOON, M.;DAVENPORT, A. J.;AMBAT, R.;CONNOLLY, B. J.;WILLIAMS, S. W. & PRICE, D. A. The effect of welding parameters on the corrosion behaviour of friction stir welded AA2024-T351. **Corrosion Science**, V. 49, 2007, 877–909.

62. SCHNEIDER, J. A.;NUNES, A.C., J. & BRENDEL, M. S. The Influence of Friction Stir Weld Tool Form and Welding Parameters on Weld Structure and Properties : Nugget Bulge in Self- Reacting Friction Stir Welds The Influence of Friction Stir Weld Tool Form and Welding Parameters on Weld Structure and Propertie. **International Symposium on Friction Stir Welding**, 1991,

63. CHEN, Z. W.;PASANG, T. & QI, Y. Shear flow and formation of Nugget

zone during friction stir welding of aluminium alloy 5083-O. **Materials Science and Engineering A**, V. 474, 2008, 312–316.

64. HILGERT, J.;SCHMIDT, H. N. B.;DOS SANTOS, J. F. & HUBER, N. Thermal models for bobbin tool friction stir welding. **Journal of Materials Processing Technology**, V. 211, 2011, 197–204.
65. LIU, H. J.;FUJII, H.;MAEDA, M. & NOGI, K. Tensile properties and fracture locations of friction-stir-welded joints of 2017-T351 aluminum alloy. **Journal of Materials Processing Technology**, V. 142, 2003, 692–696.
66. MISHRA, R. S. & MA, Z. Y. Friction stir welding and processing. **Materials Science and Engineering R: Reports**, V. 50, 2005, 1–78.
67. DORIN, T.;DESCHAMPS, A.;DE GEUSER, F.;LEFEBVRE, W. & SIGLI, C. Quantitative description of the T 1 formation kinetics in an Al-Cu-Li alloy using differential scanning calorimetry, small-angle X-ray scattering and transmission electron microscopy. **Philosophical Magazine**, V. 94, 2014, 1012–1030.
68. AHMADI, S.;ARABI, H. & SHOKUHFAR, A. Formation mechanisms of precipitates in an Al-Cu-Li-Zr alloy and their effects on strength and electrical resistance of the alloy. **Journal of Alloys and Compounds**, V. 484, 2009, 90–94.
69. SIDHAR, H. & MISHRA, R. S. Aging kinetics of friction stir welded Al-Cu-Li-Mg-Ag and Al-Cu-Li-Mg alloys. **Materials and Design**, V. 110, 2016, 60–71.
70. STEUWER, A.;DUMONT, M.;ALTENKIRCH, J.;BIROSCA, S.;DESCHAMPS, A.;PRANGNELL, P. B. & WITHERS, P. J. A combined approach to microstructure mapping of an Al-Li AA2199 friction stir weld. **Acta Materialia**, V. 59, 2011, 3002–3011.
71. ZHANG, H.;WANG, M.;ZHANG, X. & YANG, G. Microstructural characteristics and mechanical properties of bobbin tool friction stir welded 2A14-T6 aluminum alloy. **Materials & Design (1980-2015)**, V. 65, 2015, 559–566.